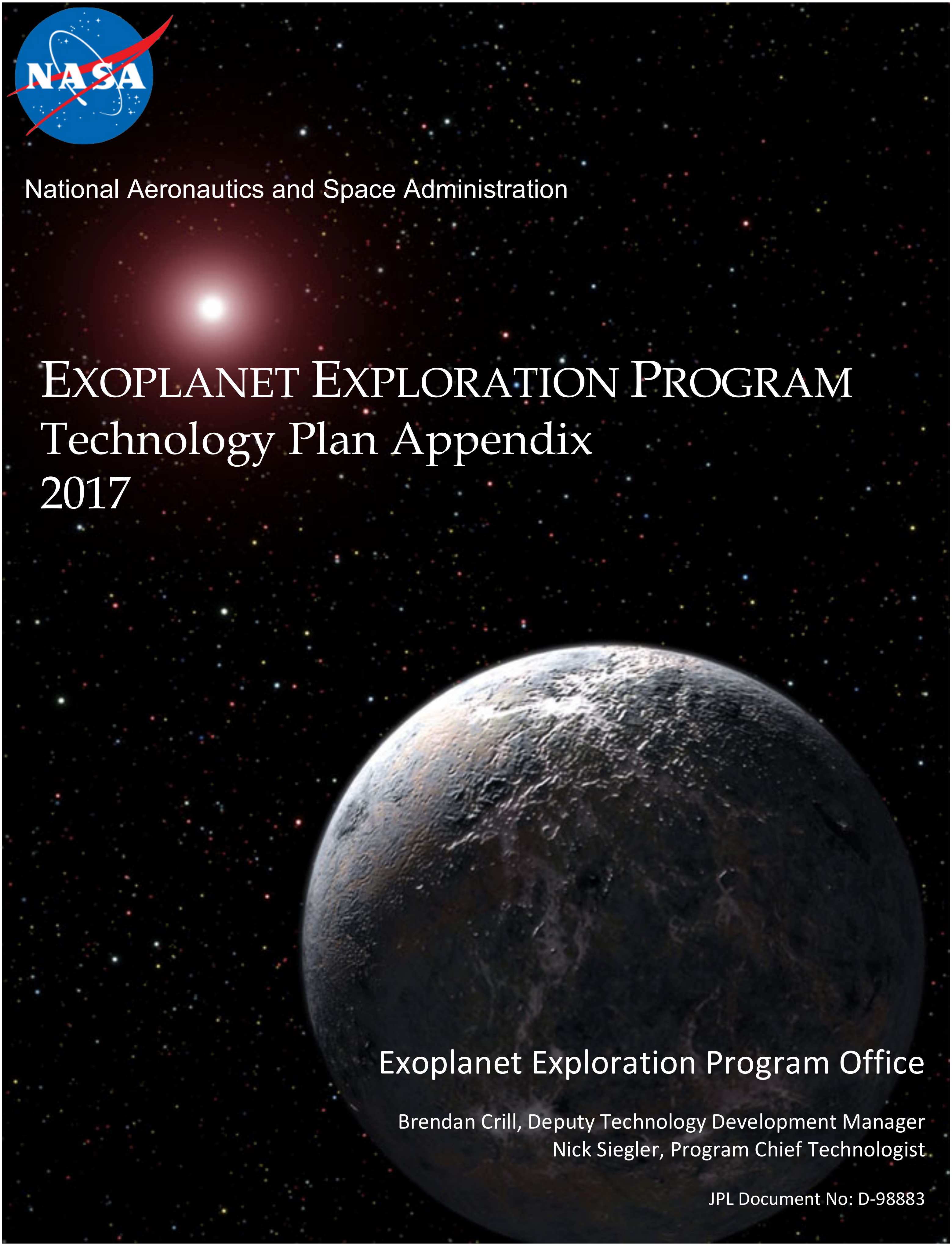

National Aeronautics and Space Administration

EXOPLANET EXPLORATION PROGRAM
Technology Plan Appendix
2017

Exoplanet Exploration Program Office

Brendan Crill, Deputy Technology Development Manager
Nick Siegler, Program Chief Technologist

JPL Document No: D-98883

Acknowledgment

Important contributions were made from Garreth Ruane (California Institute of Technology), Bertrand Mennesson (JPL), Fang Shi (JPL), Brian Hicks (GSFC), John Steeves (JPL), Dan Scharf (JPL), Ilya Poberezhskiy (JPL), John Krist (JPL), Charles Lawrence (JPL), Stuart Shaklan (JPL), Steve Warwick (NGAS), Webster Cash (University of Colorado), Stefan Martin (JPL), Charlie Noecker (JPL), Jeff Jewell (JPL), Tiffany Glassman (NGAS), Doug Leviton (Leviton Metrology), Anthony Harness (University of Colorado), David Webb (JPL), Remi Soummer (Space Telescope Science Institute), Neil Zimmerman (Space Telescope Science Institute), James Breckinridge (University of Arizona / California Institute of Technology), Ruslan Belikov (NASA AMES), Douglas Hudgins (NASA), and Matt Bolcar (GSFC).

This document has been cleared for public release (CL #17-0617).
.

This research was carried out at the Jet Propulsion Laboratory, California Institute of Technology, under a contract with the National Aeronautics and Space Administration.

APPROVALS
Approved by:

E-SIGNED by Gary Blackwood
on 2017-02-01 22:41:17 GMT

__________________________________ ___________

Dr. Gary Blackwood Date
Program Manager
Exoplanet Exploration Program
NASA / Jet Propulsion Laboratory
California Institute of Technology

E-SIGNED by Doug Hudgins
on 2017-02-01 23:47:25 GMT

__________________________________ ___________

Dr. Douglas Hudgins Date
Program Scientist for Programs
Exoplanet Exploration Program
Science Mission Directorate
NASA Headquarters

Concurred by:

E-SIGNED by Karl Stapelfeldt
on 2017-02-02 18:19:41 GMT

__________________________________ ___________

Dr. Karl Stapelfeldt Date
Program Chief Scientist
Exoplanet Exploration Program
NASA / Jet Propulsion Laboratory
California Institute of Technology

E-SIGNED by Keith Warfield
on 2017-01-30 22:51:38 GMT

__________________________________ ___________

Keith Warfield Date
Program Chief Engineer
Exoplanet Exploration Program
NASA / Jet Propulsion Laboratory
California Institute of Technology

Prepared by:

E-SIGNED by Brendan Crill
on 2017-01-30 22:40:00 GMT

____ _____________

Dr. Brendan Crill Date
Deputy Technology Development Manager
Exoplanet Exploration Program
NASA / Jet Propulsion Laboratory
California Institute of Technology

E-SIGNED by Nick Siegler
on 2017-01-31 01:52:49 GMT

____ _____________

Dr. Nicholas Siegler Date
Program Chief Technologist
Exoplanet Exploration Program
NASA / Jet Propulsion Laboratory
California Institute of Technology

Table of Contents

A INTRODUCTION

The purpose of this Technology Development Plan Appendix is to guide near-term (1–5 year) technology development for future space observatories related to NASA's Exoplanet Exploration Program (ExEP or Program). A long-term goal of the Program is a New Worlds Mission, such as that envisaged by the 2010 Decadal Survey *New Worlds, New Horizons in Astronomy and Astrophysics* (NWNH)[1]—a mission capable of directly imaging terrestrial planets in the habitable zones (HZs) of stars in the solar neighborhood, and measuring their spectra to search for signs of life. Such a mission will require extreme starlight suppression and new technology developments.

In the near term, this technology development should also enable other missions, such as probe-class (life-cycle cost less than $1B) missions with compelling science as funded by the Astrophysics Division.

This Appendix lists the enabling and enhancing technology needs of the ExEP that support the efforts of NASA’s Astrophysics Division to respond to the 2010 Decadal Survey and mid-decadal (2016) recommendations.[2] This response is captured in the Astrophysics Division Implementation Plan (updated in 2016).[3] The greatest emphasis is placed on technologies that enable direct imaging and characterization of Earth-like planets around Sun-like stars.

The technology needs sections (Sections B, C, and D) define the technology gaps and quantify, when possible, the difference between expected performance requirements and the current state-of-the-art. These sections also summarize recent key developments and communicate, when known, what is planned in the near future. Alternative technologies are also presented, as appropriate.

This 2017 Appendix includes a broader set of technology gaps than in previous years. The criteria for selecting technology needs for tracking by the ExEP, in response to Exo-TAC recommendations, were broadened to include technologies that enable or enhance direct imaging and characterization of exoplanets, rather than only enabling imaging of habitable zone exo-Earths.

Note that, while the ExEP will track all the listed technology gaps, a number of them are cross-cutting and important to all three Astrophysics Division science themes (Cosmic Origins, Physics of the Cosmos, and the ExEP). Several of the ExEP technology needs may be funded by the other Programs.

This Appendix communicates overall technology needs to aid scientists, engineers, and technology managers in academia, industry, research labs, and NASA centers in deciding which technology areas they are best suited to develop. However, not all the technologies to fly a New Worlds mission listed here are currently solicited under the Research Opportunities in Space and Earth Sciences (ROSES) Strategic Astrophysics Technology (SAT) Program (ROSES 2016, Appendix D.8). The specific technologies that are solicited under the SAT Program are described in the call for proposals. In general, an effort is made to identify the tallest tent poles within the limits of available funding, using the prioritization process described in this

Appendix. Please note that in the case of a discrepancy between the ROSES language and this appendix, the ROSES language has precedent.

A.1 Program Goals

The 2010 Decadal Survey recommended the creation of a New Worlds Technology Development Program “to lay the technical and scientific foundation for a future mission to study nearby Earth-like planets” (pp. 215–217). The Technology Development for Exoplanet Missions (TDEM) element of the SAT Program was established to support the maturation of key technologies that will enable NASA to achieve that goal. Previous work under the auspices of the SAT/TDEM Program, as well as the results of the Exo-Coronagraph (Exo-C) and Exo-Starshade (Exo-S) probe studies,[4] which concluded in 2015, demonstrate that both coronagraphs and external occulters (starshades) are scientifically meritorious and their technology needs feasible for a future New Worlds mission.

The NASA Astrophysics Division response to the Decadal Survey’s recommendations (2016 Astrophysics Implementation Plan Update) describes a path for implementing the Wide-Field Infrared Survey Telescope (WFIRST),[5] the top large-scale mission recommendation and the next strategic mission after the James Webb Space Telescope (JWST). It also recommends concept development for future strategic missions for consideration by the 2020 Decadal Survey.

In 2016, NASA entered the formulation phase of the WFIRST mission, which makes use of one of two 2.4-m-diameter Astrophysics Focused Telescope Assets donated to NASA by another Federal agency. A high-contrast exoplanet coronagraph with wavefront control has been baselined as part of the planned WFIRST implementation. However, a WFIRST coronagraph is not expected to have the contrast sensitivity to directly image exo-Earths. Consequently, this Appendix describes the technologies devoted to instrument performance on post-WFIRST missions capable of directly imaging and characterizing Earth-like planets.

Many of the exoplanet detection and characterization technology needs described here are intended to support the exoplanet science objectives of the two NASA Astrophysics Division 2020 Decadal Survey large mission concept studies—the Large Ultra-Violet Optical InfraRed (LUVOIR) Surveyor and the Habitable Exoplanet Imaging (HabEx) Mission. Both telescope designs are expected to be driven by exo-Earth detection and characterization capabilities, and we assume that, unlike the case with WFIRST, the coronagraph engineering requirements will drive the telescope requirements to meet the challenging contrast requirements. Both mission concept studies commenced in 2016 for approximately three-year durations. The studies are led by Science and Technology Definition Teams (STDTs) and supported by NASA field centers for engineering and design work. While the detailed science goals, system architecture, and instrument suite for each mission concept are still being defined, in the summer of 2016, each of the STDTs submitted a list of technology gaps to the two NASA Program Offices[6] consisting of technology development needs for reaching the likely science objectives of each mission. Each of these STDT gap lists were reviewed as part of the annual ExEP technology selection and prioritization process, and the ExEP technology gap lists presented in this Appendix reflect our initial assessment of the STDTs’s lists. As the work of the STDTs advances, the technology needs may change in future editions.

NASA's ExEP supports activities that contribute to the maturation of key technologies that will enable these exoplanet mission concepts. The Program funds and facilitates experiments and analyses selected by NASA HQ through yearly solicitations issued through the omnibus ROSES NASA Research Announcement (NRA). The Program also provides support in the form of infrastructure, modeling, expertise, and test facilities to selected Principal Investigators (PIs).

As a part of ROSES, NASA currently funds technology development through the Astrophysics Research and Analysis (APRA) solicitation and the SAT/TDEM solicitations. APRA covers low Technology Readiness Level (TRL) technology research (TRL 1-2) while SAT/TDEM covers maturation of mid-range TRL technologies (TRL 3-5). This two-stage approach is intended to support the advancement of technology envisaged by the 2010 Decadal Survey. All the previous tasks funded under the 2009, 2010, 2012, 2013, 2014, and 2015 SAT/TDEM solicitations are listed in **Table 1**; SAT/TDEM whitepapers and abstracts can be found online.[7] Abstracts of funded APRA awards can also be found online.[8]

A.2 Previously Funded Efforts

Table 1 lists the previously funded TDEM awards, grouped by research area. Final Milestone Reports for completed TDEMs as well as Milestone Whitepaper Reports for those still in process are posted on the ExEP Technology website.[9]

Table 1: TDEM awards for calls from 2009, 2010, 2012, 2013, 2014, and 2015.

Year	PI	Institution	Proposal Title
CORONAGRAPH STARLIGHT-SUPPRESSION DEMONSTRATIONS			
2009	Mark Clampin	NASA Goddard Space Flight Center	Visible Nulling Coronagraph Technology Maturation: High Contrast Imaging and Characterization of Exoplanets
2009	Olivier Guyon	Univ. of Arizona	Phase-Induced Amplitude Apodization Coronagraphy Development and Laboratory Validation
2009	John Trauger	JPL/Caltech	Advanced Hybrid Lyot Coronagraph Technology for Exoplanet Missions
2010	Olivier Guyon	Univ. of Arizona	Advances in Pupil Remapping (PIAA) Coronagraphy: improving Bandwidth, Throughput and Inner Working Angle
2010	Richard Lyon	NASA Goddard Space Flight Center	Compact Achromatic Visible Nulling Coronagraph Technology Maturation
2010	Jagmit Sandhu	JPL/Caltech	Visible Nulling Coronagraph (VNC) Technology Demonstration Program
2010	Eugene Serabyn	JPL/Caltech	Demonstrations of Deep Starlight Rejection with a Vortex Coronagraph
2013	Brian Hicks	NASA Goddard Space Flight Center	Segment Aperture Nulling Coronagraphy
2014	Matthew Bolcar	NASA Goddard Space Flight Center	Next Generation Visible Nulling Coronagraph
2014	Eugene Serabyn	JPL/Caltech	Broadband Light Rejection with the Optical Vortex Coronagraph

Year	PI	Institution	Proposal Title
STARSHADE STARLIGHT-SUPPRESSION DEMONSTRATIONS			
2009	N. Jeremy Kasdin	Princeton Univ.	Starshades for Exoplanet Imaging and Characterization: Key Technology Development
2010	N. Jeremy Kasdin	Princeton Univ.	Verifying Deployment Tolerances of an External Occulter for Starlight Suppression
2012	Suzanne Casement	Northrop Grumman Aerospace Systems	Starshade Stray Light Mitigation through Edge Scatter Modeling and Sharp-Edge Materials Development
2012	Tiffany Glassman	Northrop Grumman Aerospace Systems	Demonstration of Starshade Starlight-Suppression Performance in the Field
2012	N. Jeremy Kasdin	Princeton Univ.	Optical and Mechanical Verification of an External Occulter for Straight Suppression *(transferred to starshade technology activity)*
2013	Webster Cash	Univ. of Colorado	Development of Formation Flying Sensors
2013	N. Jeremy Kasdin	Princeton Univ.	Formation Flying for External Occulters *(transferred to starshade technology activity)*
2014	Mark Thomson	JPL/Caltech	Optical Shield for the Starshades Inner Disk Subsystem *(transferred to starshade technology activity)*
WAVEFRONT SENSING AND CONTROL OF SCATTERED STARLIGHT			
2009	John Krist	JPL/Caltech	Assessing the Performance Limits of Internal Coronagraphs Through End-to-End Modeling
2009	M. Charley Noecker	Ball Aerospace	Advanced Speckle Sensing for Internal Coronagraphs and Methods of Isolating Exoplanets from Speckles
2010	Paul Bierden	Boston Micromachines	MEMS Deformable Mirror Technology Development for Space-Based Exoplanet Detection
2010	Michael Helmbrecht	Iris AO	Environmental Testing of MEMS Deformable Mirrors for Exoplanet Detection
2010	N. Jeremy Kasdin	Princeton Univ.	Integrated Coronagraph Design and Wavefront Control using Two Deformable Mirrors
OTHER TECHNOLOGIES			
2009	Donald Figer	Rochester Inst. of Technology	A Photon-Counting Detector for Exoplanet Missions
2010	Stuart Shaklan	JPL/Caltech	Coronagraph Starlight Suppression Model Validation: Coronagraph Milestone Report #3
2013	Eduardo Bendek	NASA Ames Research Center	Enhanced Direct Imaging Exoplanet Detection with Astrometric Mass Determination
2015	Jim Breckinridge	University of Arizona	Threshold Raw Retrieved Contrast in Coronagraphs is Limited by Internal Polarization

A.3 Technology Gap Selection and Prioritization Criteria

The exoplanet science and technology community, including the large mission STDTs, submitted proposed technology needs during an annual solicitation period during the summer of 2016. Along with the technology gaps listed in the 2016 edition of the Technology Development Plan Appendix, these were first judged against selection criteria to determine the relevance to ExEP as follows:

1. Technology Gaps considered for tracking and development by the ExEP must support APD exoplanet science missions as:
    - described in the Astrophysics Implementation Plan;
    - directed through the Science Mission Directorate;
    - selected through open competition;
    - described in the APD 30-year roadmap; and/or,
    - part of the 2020 Decadal Survey large mission concept studies.
2. The subset of these gaps that either enables or enhances the direct detection and characterization of exoplanets are prioritized onto the ExEP Technology Gap List.
3. The remaining technology gaps considered to benefit exoplanet science will be captured onto a watch list of other technology opportunities that may benefit exoplanet science. These gaps will be tracked and re-evaluated annually for potential prioritization.

The subset of the ExEP Technology Gap List that targets coronagraphs and starshades are listed in **Table 3** and Table 4, respectively, in order of priority based on:

- Impact
- Urgency
- Trend

These selection and prioritization criteria were proposed by the ExEP Program Chief Technologist and ExEP Deputy Technology Development Manager, and presented to the Exoplanet Program Analysis Group (ExoPAG) and its Executive Committee for review and feedback. After this review, the criteria were presented to the ExoTAC for formal review. With the addition of this review step, the language used to score the 2017 gap list differs slightly from 2016, reflecting the important feedback from the ExoTAC.

The higher the number within each criterion, the higher the contribution to the prioritization. Results of the prioritization effort can be found in Section F. These criteria are subjectively defined in Table 2. A total score for each technology gap is determined with a weighted sum: Impact and Urgency scores are each weighted by a factor 10 and Trend is weighted by a factor 5. The ExEP Program Chief Technology and ExEP Deputy Technology Development Manager proposed initial scores within each category based on the criteria language. The ExoTAC formally reviewed the scores, providing suggestions which are reflected in the scoring and the resulting ranking shown here.

Table 2: Technology gap prioritization criteria

Impact: (weight: 10)	4: Critical technology - required to meet mission concept objectives; without this technology, applicable missions would not launch
	3: Highly desirable - not mission-critical, but provides major benefits in enhanced science capability, reduced critical resources need, and/or reduced mission risks; without it, missions may launch, but science or implementation would be compromised
	2: Desirable - not required for mission success, but offers significant science or implementation benefits; if technology is available, would almost certainly be implemented in missions
	1: Minor science impact or implementation improvements; if technology is available would be considered for implementation in missions

Urgency (weight: 10)	4: Reduced risk needed for missions currently in pre-formulation or formulation.
	3: In time for the Decadal Survey (2020); not necessarily at some TRL but reduced risk by 2020.
	2: Earliest projected launch date < 15 yr (< 2030)
	1: Earliest projected launch date > 15 yr (> 2030)

Trend (weight: 5)	4: (a) no ongoing current efforts, or (b) little or no funding allocated
	3: (a) others are working towards it but little results or their performance goals are very far from the need, (b) funding unclear, or (c) time frame not clear
	2: (a) others are working towards it with encouraging results or their performance goals will fall short from the need, (b) funding may be unclear, or (c) time frame not clear
	1: (a) others are actively working towards it with encouraging results or their performance goals are close to need, (b) it's sufficiently funded, and (c) time frame clear and on time

B CORONAGRAPH TECHNOLOGY NEEDS

Exo-Earth detections will require starlight suppression that exceeds the current best ground-based performances by several orders of magnitude (**Figure 1**). Coronagraphs come in numerous architectures, each with its own strengths and weaknesses with respect to telescope aperture (monolithic, segmented), obscuration (unobscured, obscured by secondary mirror and its support struts), and wavefront error sensitivity (e.g. line-of-sight jitter, telescope vibration, polarization).

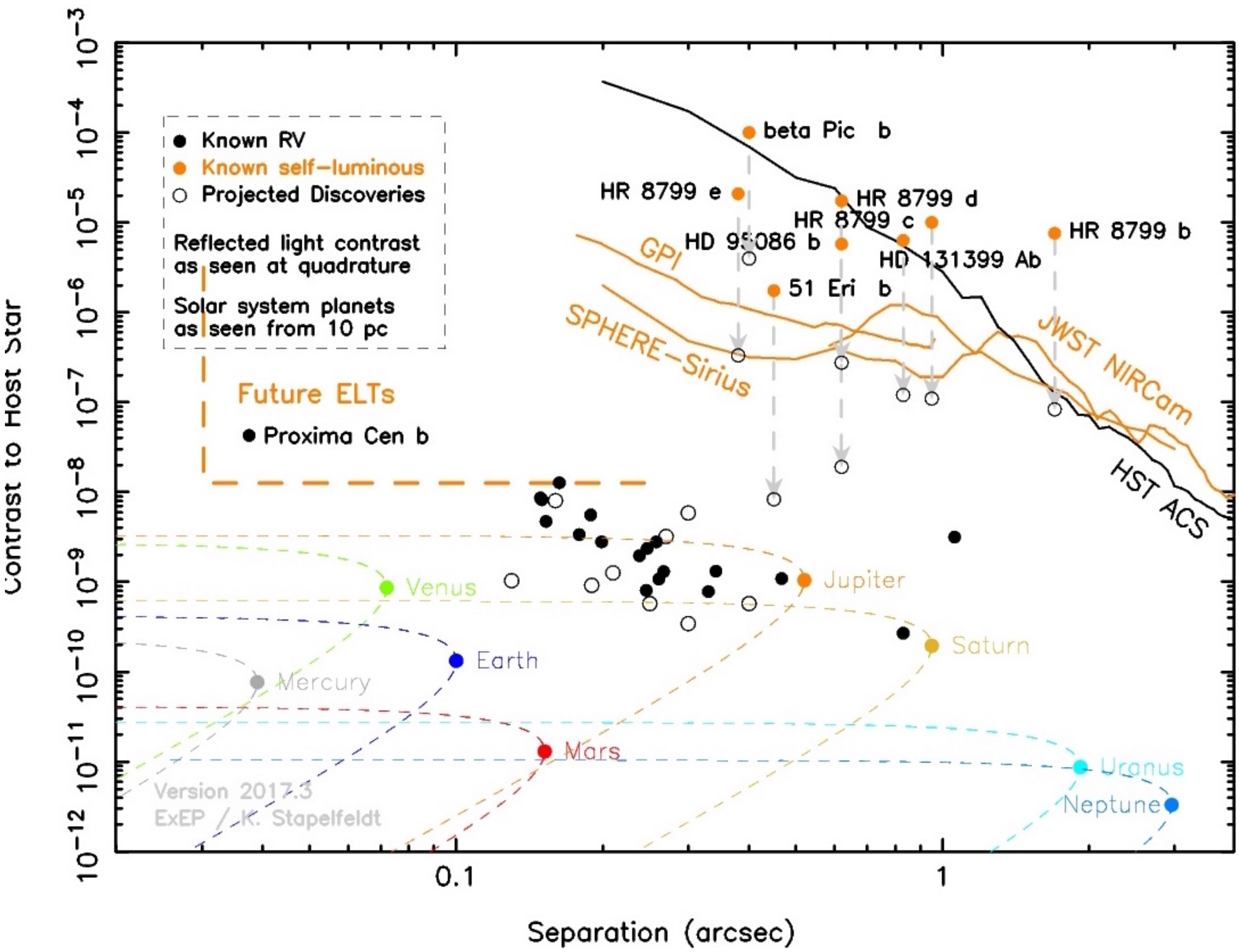

Figure 1: Contrast (ratio of planet brightness to host star brightness) versus angular separation. The filled orange circles indicate the direct imaging of young, self-illuminous planets imaged in the near-infrared by ground-based telescopes. Contrasts for the planets of the Solar System are for analogous planets placed 10 pc away. The solid black dots are contrast estimates of measured radial velocity planets. The solid orange curves show measured performance of ground-based coronagraphs: the GPI curve shows typical performance, while the SPHERE curve shows the best achieved performance to-date on Sirius. Achieved performance with HST/ACS coronagraphic masks, and the predicted performance of JWST/NIRCam masks are also shown. The dashed orange curve assumes future ELTs will reach 10-8 contrast at 0.03 arcsec. Planets discovered in the near-infrared are shown with vertical arrows pointing to the predicted contrast ratios at visible wavelengths.

The removal of diffraction is only part of the coronagraph's design goals. It must also remove the scattered light observed in the focal plane, appearing as speckles, due to imperfections in the optics. This is done through the control of deformable mirrors (Section B.3.6). As a final step, post-processing of the data images (Section B.5) further improves the effective contrast.

The most important development in coronagraph technology is the baselining of a coronagraph instrument on the WFIRST space mission—it will be the first coronagraph with wavefront control to fly in space, advancing both space and ground state-of-the-art starlight suppression. While both the Hubble Space Telescope (HST) and the JWST have onboard coronagraphs, neither have the corresponding wavefront sensing and control required to achieve better than 10^{-8} contrast sensitivity and close inner working angles (IWA) (< 3 λ/D). WFIRST will also have the first ultra-low noise visible detector and deformable mirrors to reach low-Earth orbit or beyond.

The obscured pupil of the WFIRST telescope (due to its on-axis secondary mirror and support struts) introduces complex diffraction features that are absent in designs with unobscured pupils. Consequently, the WFIRST coronagraph architectures and optics have started the era of high-conrast/obscured pupil coronagraph design and demonstration that will serve on-axis and segmented telescope aperture designs of the future.

The ExEP coronagraph technology needs (**Table 3**) target the next generation coronagraphs beyond WFIRST, which will be capable of directly imaging exo-Earths around Sun-like stars in the solar neighborhood. As mentioned earlier, the list of coronagraph technology needs has been broadened to include more of the telescope system since all contributing noise sources must be accounted for if contrasts of 10^{-10} are to be reached at 10^{-11} stability levels.

The coronagraph technology gaps listed in **Table 3** fall into four technology areas shown in Figure 2:

1. **Contrast** – the ability to block the on-axis light from a target star creating a dark region in the science focal plane where the faint off-axis reflected light of a planet could be detected.
2. **Contrast Stability** – the ability to sense and control the incoming starlight maintaining the desired contrast long enough for full science integration.
3. **Detection Sensitivity** – the ability to detect extraordinarily few photons dispersed across many pixels of a spectrograph and not be lost in the detector’s read-out noise.
4. **Angular Resolution** – the ability to probe terrestrial regions around stars (e.g., the habitable zone) requires a minimum aperture size. The more distant the star, the larger the telescope aperture will need to be to probe these regions. Large apertures provide not just improved angular resolution but also improved sensitivity to faint objects (sharper point spread functions), higher throughput, lower integration times, and the capability to probe habitable zones of stars further away.

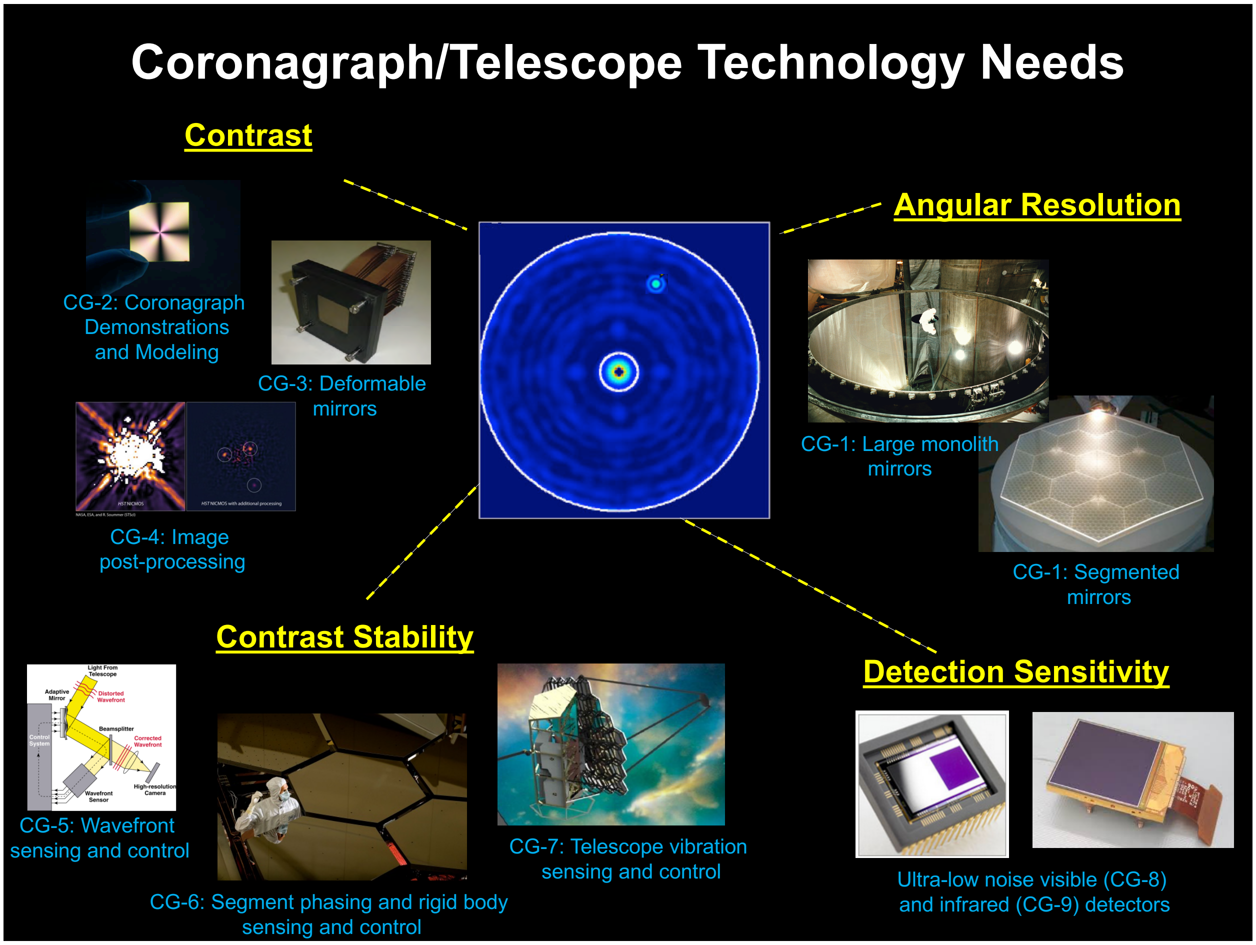

Figure 2: The four technology areas of coronagraph technology needs (in yellow font) to directly image and characterize exo-Earths around Sun-like stars. Several technology gaps involving operation in the UV (CG-10 and CG-12) and mid infrared (CG-11) are not shown in this schematic.

Table 3: ExEP Coronagraph Technology Gap List. Gaps are listed in order of their prioritization scores according to the criteria in Section A.3. The priority column refers to Table 8.

Priority	ID	Title	Description	Current Capabilities	Needed Capabilities
3	CG-1	**Large Aperture Primary Mirrors**	Large monolith and multi-segmented mirrors that meet tight surface figure error and thermal control requirements at visible wavelengths	<u>Flight</u> Monolith: 3.5-m sintered SiC with <3 µm SFE (Herschel) 2.4-m ULE with ~10 nm SFE (HST) Depth: Waterjet cutting is TRL 9 to 14", but TRL 3 to >18". Fused core is TRL 3; slumped fused core is TRL 1. Segmented (no flight SOA): 6.5 m Be with 25 nm SFE (JWST) Non-NASA: 6 DOF, 1-m class SiC and ULE, < 20 nm SFE, and < 5 nm wavefront stability over 4 hr with thermal control	Aperture: 4–16 m; SFE < 10 nm rms (wavelength coverage 400–2500 nm) Wavefront stability better than 10 pm rms per wavefront control time step. Segmented apertures leverage 6 DOF or higher control authority meter-class segments for wavefront control. Environmentally tested
3	CG-2	**Coronagraph Demonstrations and Modeling**	Coronagraph optics and architecture that suppress diffracted starlight by a factor of < 10^{-9} at visible and infrared wavelengths	<u>Lab:</u> 6×10^{-10} raw contrast at 10% bandwidth across angles of 3-15 λ/D demonstrated with a linear mask and an <u>unobscured</u> pupil in a static vacuum lab environment (Hybrid Lyot) < 1.6x10^{-9} raw contrast at 10% bandwidth across angles of 3-9 λ/D demonstrated with a circularly-symmetric mask and <u>obscured</u> pupil in a static vacuum lab environment (WFIRST) <u>Flight:</u> 10^{-4} raw contrast 540 nm at 10 λ/D (HST)	Coronagraph masks and optics capable of creating circularly symmetric dark regions in the focal plane enabling raw contrasts ≤ 10^{-9}, with minimal contribution from polarization aberration, IWA ≤ 3 λ/D, throughput ≥ 10%, and bandwidth ≥ 10% on obscured and segmented pupils in a simulated dynamic vacuum environment.

Priority	ID	Title	Description	Current Capabilities	Needed Capabilities
3	CG-6	**Mirror Figure/ Segment Phasing Sensing & Control**	Segmented or monolith large aperture mirrors require segment phasing and rigid-body sensing and control of the segments or the surface figure to achieve tight static and dynamic wavefront errors.	6 nm rms rigid body positioning error and 49 nm rms stability (JWST error budget) SIM and non-NASA: nm accuracy and stability using laser metrology No flight SOA; ground-based (Keck) achieved 6 nm positioning error in operations	Systems-level considerations to be evaluated but expect will require WFE stability less than 10 pm rms sensitivity and control over periods of tens of minutes
3	CG-7	**Telescope Vibration Sensing and Control**	Isolation and/or damping of spacecraft and payload vibrational disturbances	80 dB attenuation at frequencies > 40 Hz (JWST passive isolation) Disturbance-free payload demonstrated at TRL 5 with 70 dB attenuation at "high frequencies" with 6-DOF low-order active pointing	Monolith: 120 dB end-to-end attenuation at frequencies >20 Hz Segmented: 140 dB end-to-end attenuation at frequencies > 40 Hz
3	CG-9	**Ultra-Low Noise Near-Infrared Detectors**	Near-infrared wavelength (900 nm to 2.5 μm), extremely low noise detectors for exo-Earth spectral characterization with Integral Field Spectrographs	Lab: HgCdTe photodiode arrays have read noise $\lesssim$ 2 e- rms with multiple nondestructive reads; 2k×2k format; dark current < 0.001 e-/s/pix; very radiation tolerant (JWST) HgCdTe APDs have dark current ~10–20 e-/s/pix, RN << 1 e- rms, and < 1k×1k format Sub-Kelvin photon-counting detectors (KID,TES): 0 read noise/dark current; radiation tolerance is unknown; <1k×1k format Flight: HST WFC3/IR HgCdTe dark current 0.05 e-/px/s, 12 e- read noise, 1k×1k format	Read noise << 1 e- rms, dark current noise < 0.001 e-/pix/s, in a space radiation environment over mission lifetime ≥ 2k×2k format

Priority	ID	Title	Description	Current Capabilities	Needed Capabilities
4	CG-5	**Wavefront Sensing and Control**	Sensing and control of line-of-sight jitter and low-order wavefront drift	Lab: < 0.5 mas rms per axis LOS residual error demonstrated in lab with a fast-steering mirror attenuating a 14 mas LOS jitter and reaction wheel inputs; ~12 pm rms sensitivity of focus (WFIRST) Higher low-order modes sensed to 10–100 nm WFE rms on ground-based telescopes Flight: No SOA	Sufficient fast line-of-sight jitter (< 0.5 mas rms residual) and slow thermally-induced WFE sensing and control (≤ 10 pm rms sensitivity) to maintain closed-loop < 10^{-9} raw contrast with an obscured/segmented pupil and simulated dynamic environment
4	CG-3	**Deformable Mirrors**	Flight-qualified large-format deformable mirrors and their electronics	Lab: Electrostrictive 64×64 actuator DMs have been demonstrated to meet ≤ 10^{-9} contrasts and < 10^{-10} stability in a vacuum environment and 10% bandwidth; 48×48 actuator DM passed random vibe testing Flight: No SOA	4 m primary mirror: ≥ 96×96 actuators 10 m primary mirror: ≥128×128 actuators Enable raw contrasts of ≤ 10^{-9} at ~20% bandwidth and IWA ≤ 3 λ/D Flight-qualified device and drive electronics (radiation hardened, environmentally tested, life-cycled including connectors and cables)
4	CG-8	**Ultra-Low Noise Visible Detectors**	Low-noise visible detectors for faint exoplanet characterization with an Integral Field Spectrograph	Lab: 1k×1k silicon EMCCD detectors provide dark current of 7×10^{-4} e^-/px/sec; CIC of 2.3x10^{-3} e^-/px/frame; effective read noise < 0.2e- rms (in EM mode) after irradiation when cooled to 165.15K (WFIRST) 4k×4k EMCCD fabricated but still under development Flight: HST WFC3/UVIS CCD 3.1e^- read noise, dark current 2×10^{-3}, format 2k×2k	Effective read noise < 0.1e- rms; CIC < 3×10^{-3} e-/px/fram; dark current < 10^{-4} e-/px/sec tolerant to a space radiation environment over mission lifetime ≥ 2k×2k format

Priority	ID	Title	Description	Current Capabilities	Needed Capabilities
6	CG-4	**Data Post-Processing Algorithms and Techniques**	Data post-processing techniques to uncover faint exoplanet signals from residual speckle noise at the focal-plane detector	Few 100× speckle suppression has been achieved by HST and by ground-based AO telescopes in the NIR and in contrast regimes of 10^{-4} to 10^{-5}, dominated by phase errors.	A 10-fold contrast improvement in the visible from 10^{-9} raw contrast where amplitude errors are expected to be important (or a demonstration of the fundamental limits of post-processing)
7	CG-10	**Mirror Coatings for UV/NIR/Vis**	Mirror coatings that enable high reflectivity to wavelengths as short as 90 nm	Al coating with combination of MgF_2, LiF, and/or AlF_3 overcoat: 90-120 nm: < 50% reflectivity 120-300 nm: 85% reflectivity 300 nm-2 µm: > 90% reflectivity Polarization differences between orthogonal polarization states, uniformity, and durability of coatings on large optics is unknown. Flight: HST uses MgF_2; 85% reflectivity λ > 120 nm; 20% reflectivity λ < 120 nm	A mirror coating that that achieves 90-120 nm: > 70% reflectivity 120-300 nm: > 90% reflectivity 300 nm-2 µm: > 90% reflectivity Polarization phase and amplitude difference < 1% between orthogonal polarization states.
8	CG-11	**Mid-infrared Spectral Coronagraph**	Coronagraph architecture suitable for mid-Infrared direct imaging and spectral characterization of cool giant exoplanets.	Flight: no SOA. Lab: JWST-MIRI: four-quadrant phase masks, contrasts to 10^{-4} from 10.65-15.5 µm with inner working angles of 0.33 - 0.49" no spectral dispersion.	contrast 10^{-6}; inner working angle of 0.1" at 10 µm; spectral dispersion R ~500.
9	CG-12	**Ultra-Low Noise UV Detectors**	Low-noise ultraviolet (200-400 nm) detectors to characterize exoplanets with an integral field spectrograph.	MCP: 0 read noise, $\lambda \sim$ 90 - 300nm, spurious count rate 0.05-0.5 counts/cm2/s; QE 20-45%; resol. el. size 20 mm. EMCCD: 0 read noise, dark current >0.005 e-/res/hr; QE 30-50%; resol. el. size 20 µm Flight: HST HRC: In relevant UV band (250nm): QE 33%, read noise 4.7e-, dark current 5.8×10^{-3}, 1024x1024	Read Noise: 0 e- Dark Current: 0 e- / resol/s Spurious Count Rate: < 0.05 counts/cm^2/s QE: 75% Resol Size ≤ 10 µm Tolerant to space radiation environment over mission lifetime.

B.1 Decadal Survey Testbed

In anticipation of coronagraph demonstrations to support large monolithic and segmented telescopes reach the 10^{-10} contrast requirement, the ExEP is upgrading one of the High Contrast

Imaging Testbeds (HCIT) and vacuum chambers at JPL. Called the Decadal Survey Testbed, work will begin in the spring of 2017 taking advantage of the excellent progress made by the WFIRST CGI team and further reduce the noise floor limiting 10^{-10} contrast levels. Contributing noise sources include testbed and chamber jitter, thermal changes, and stray light. A Hybrid Lyot coronagraph (Section B.2.2) has been chosen to initially work with an unobscured pupil as this architecture is the laboratory state-of-the-art at 10% bandwidth (**Figure 5**). The Hybrid Lyot is baselined on WFIRST and was also the selected primary coronagraph from the Exo-C study[10] for off-axis monolith mirror space telescopes.

Achievement of the 10^{-10} contrast milestone is planned for the summer of 2018 at which point another coronagraph architecture could be selected in support of an off-axis monolith mission concept such as HabEx or a static segmented mask could be inserted to demonstrate performance with a simulated on-axis segmented telescope such as HabEx or LUVOIR. The subsequent step in 2019 could be the addition of a simulated telescope and disturbance source for either coronagraph architecture to produce a “dynamic” demonstration. “Static” demonstration here and throughout implies no intentionally introduced line of sight errors or other wavefront disturbances, while “dynamic” refers to the experiments where at least some of these disturbances expected on orbit are simulated in the testbed.

The ExEP will work and consult with other coronagraph testbeds operating in ambient conditions in potentially advancing coronagraph performance from mid-contrast to high-contrast demonstrations. Examples are the HiCat facility at the Space Telescope Science Institute (PI Remi Soummer; see B.2.4), the new testbed at Caltech (PI Mawet), at NASA Ames (PI Belikov), and the University of Arizona (PI Guyon).

B.2 Coronagraph Demonstrations and Modelling (CG-2)

Specialized coronagraph optics suppress on-axis starlight and allow the off-axis planet light to transmit through the instrument achieving the high contrast detection of the planet with respect to its host star. A continuing program to advance the performance of masks, apodizers, and beam-shaping optics to better than WFIRST coronagraph performance requirements ($< 10^{-8}$, 3 λ/D, 10% bandwidth) is needed. This should include designs to improve inner working angles (< 3 λ/D), contrast performance ($< 10^{-9}$), bandwidth ($\geq 10\%$), and core PSF throughput ($\geq 10\%$), in dynamic vacuum environments on both obscured and segmented apertures.

Various architectures of coronagraphs have achieved contrasts in laboratory tests that begin to approach these requirements.[11] Demonstrated state-of-art results with unobscured pupils at monochromatic, 2%, 10%, and 20% bandwidths are shown in **Figure 3–6**. The deepest narrowband (2% bandwidth; **Figure 4**) simulated starlight suppression achieved is 1.2×10^{-10} raw contrast at 800 nm across angles of 3-16 λ/D. It was demonstrated in the HCIT with a Hybrid Lyot Coronagraph (HLC) linear mask on an unobscured pupil in a static vacuum lab environment.[12,13,14]

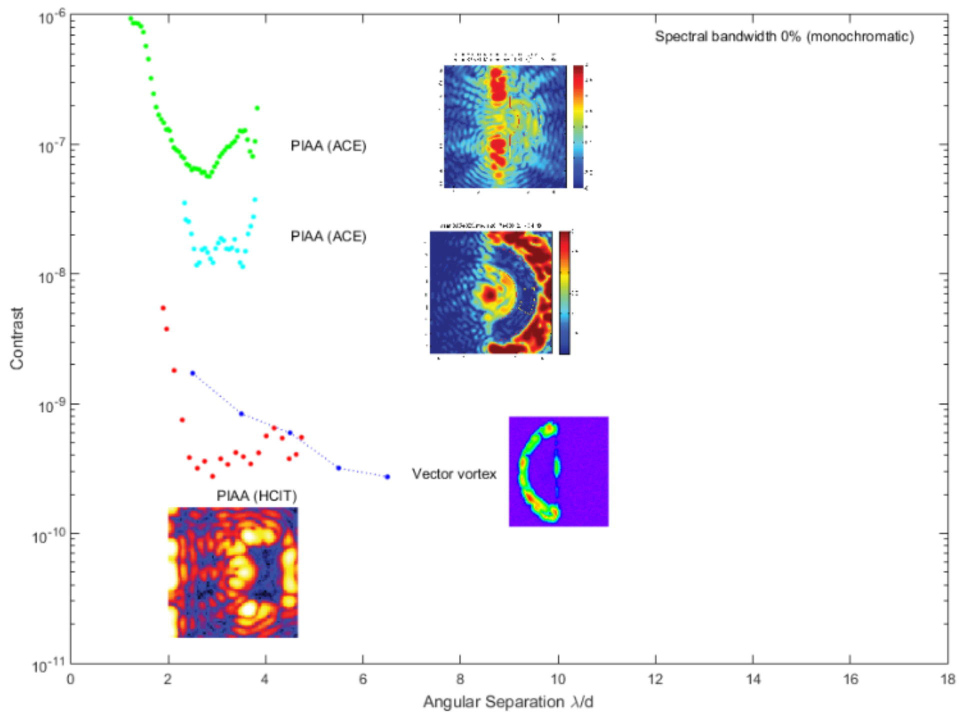

Figure 3: Coronagraph laboratory demonstrations using monochromatic spectral bandwidth with visible light.

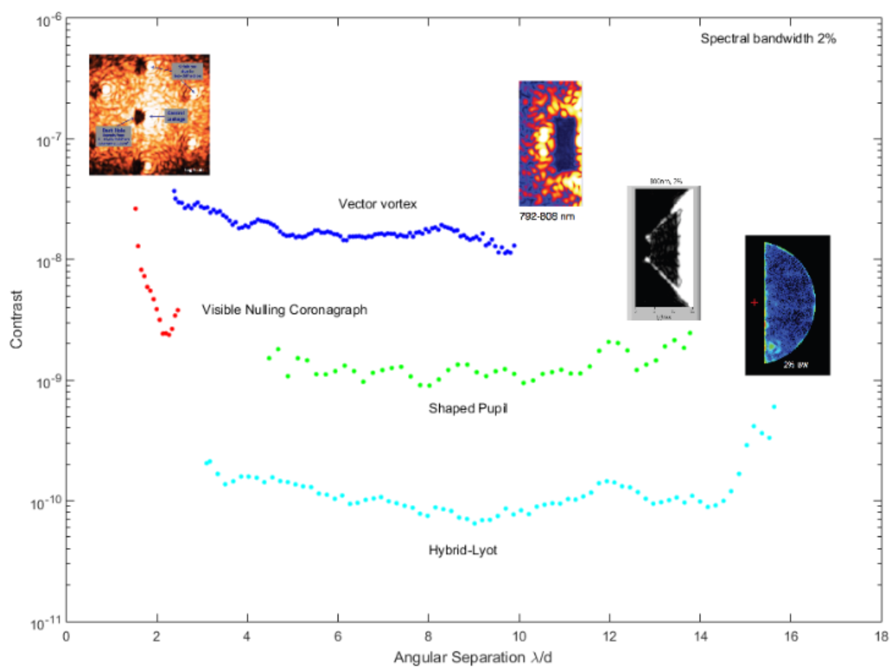

Figure 4: Coronagraph laboratory demonstrations using 2% bandwidth visible light.

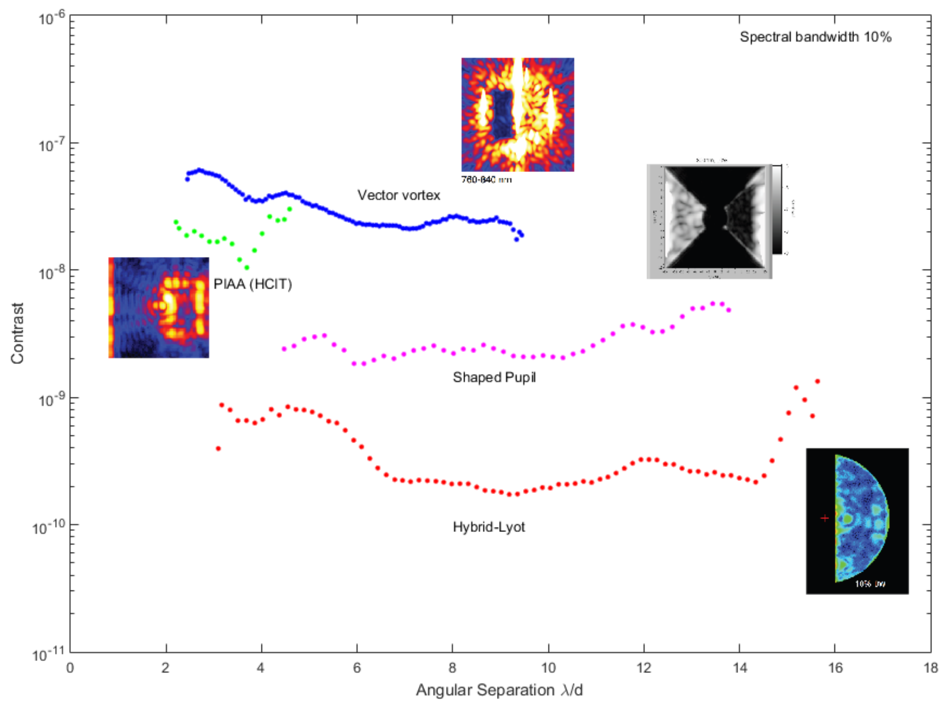

Figure 5: Coronagraph laboratory demonstrations using 10% bandwidth visible light.

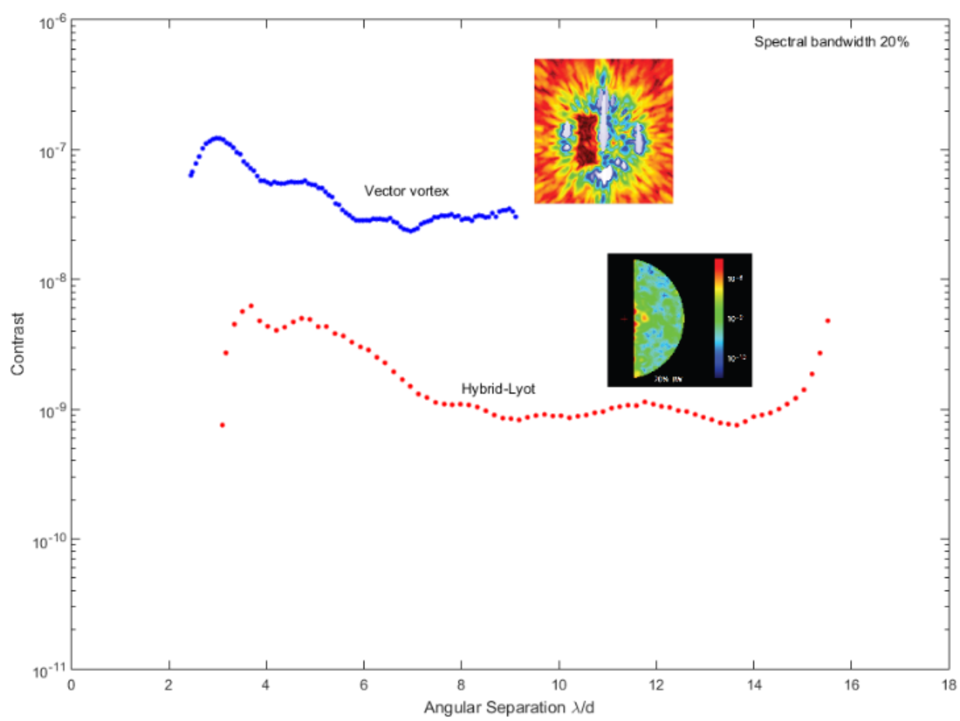

Figure 6: Coronagraph laboratory demonstrations using 20% spectral bandwidth visible light.

Demonstrated coronagraph contrast results with unobscured apertures as a function of optical bandwidth are shown in **Figure 7**.
The next level of difficulty for internal coronagraphs is working with obscured apertures. Pupil obscurations occur in on-axis design due to the secondary mirror and its structural supports. Pupil obscurations further diffract light making deep contrasts more challenging.

Additionally, the next generation of large space telescopes may have a segmented primary mirror, also adding additional challenges to coronagraphs' abilities to meet the contrast, IWA, and throughout goals. In 2016, the ExEP funded a Segmented Coronagraph Design and Analysis (SCDA) study (see Section B.3.3) for several groups to investigate, using modeling, different coronagraph designs that enable the direct imaging of exo-Earths with large segmented-aperture, partially obscured telescopes.

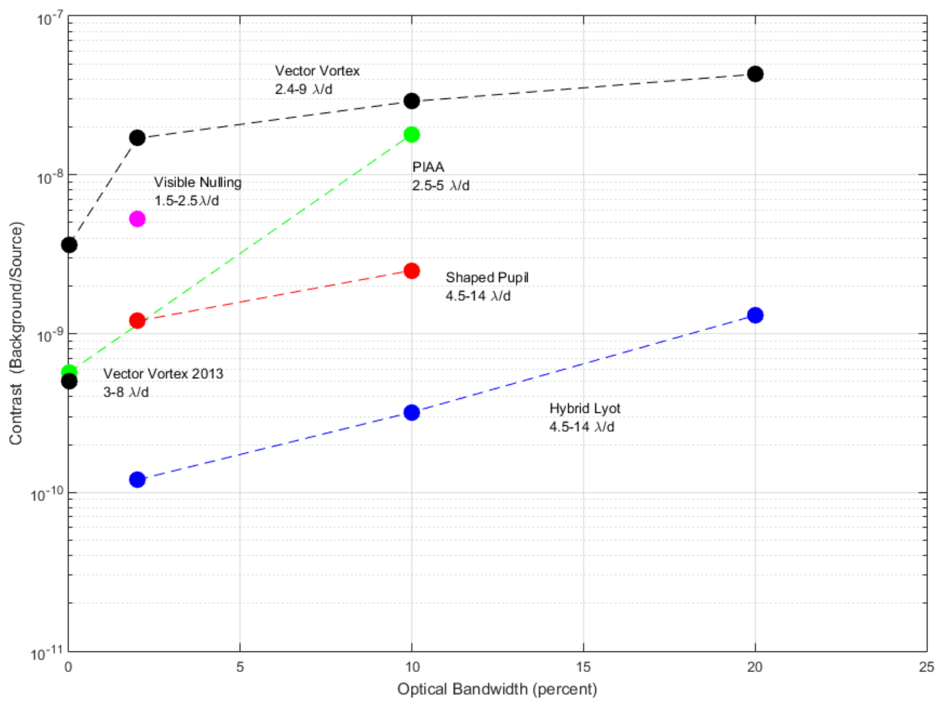

Figure 7: Demonstrated coronagraph contrast as a function of bandwidth. All experiments were conducted with unobscured pupils and demonstrated in vacuum chambers under static environment conditions at 800 nm to near-IR light.

B.2.1 Polarization Effects

In a coronagraph system, the highly reflective metal mirrors alter the polarization content across each wavefront to create polarization-induced wavefront aberrations which result in an image plane irradiance distribution that contains four nearly superimposed incoherent images. The wavefront aberrations cannot be corrected with a deformable mirror, potentially limiting a coronagraph's starlight suppression performance.[15,16] Investigations in polarization-induced wavefront aberrations in the context of coronagraphy and potential mitigating devices are therefore of great interest. Jim Breckinridge and Russell Chipman were awarded a TDEM-15[17] to investigate polarization in coronagraphy.

B.2.2 Hybrid Lyot Coronagraph

The HLC is a modification of the classical Lyot coronagraph that consists of an occulting mask located at an intermediate focal plane followed by a Lyot mask at a subsequent pupil plane. In the HLC, the focal plane mask is a combination of a patterned amplitude modulator (usually a metal coating such as nickel) with an overlaid phase modulator (a patterned dielectric coating), hence the "hybrid". Both are simultaneously optimized to provide an optimal combination of IWA, contrast, bandwidth, and throughput with the wavelength-dependent characteristics of the materials included. The hybrid occulter provides better performance over broad spectral bands than previous amplitude-only designs.

John Trauger (JPL), with a 2009 TDEM award and linear mask, demonstrated mean raw contrasts of 6×10^{-10} with a 10% bandwidth in a 284 $(\lambda/D)^2$ field extending from 3–15 λ/D (**Figure 5**). Raw contrasts of 1.3×10^{-9} were demonstrated with a 20% bandwidth (**Figure 6**). These results are the current state of the art for unobscured pupils.

Like other coronagraphic techniques, the performance of the HLC is seriously degraded by obscurations in the telescope, especially asymmetric ones such as the WFIRST secondary support struts. As part of the design optimization process, deformable mirrors (DMs) were used to alter the wavefront to reduce the diffractive effects of these structures, resulting in a pattern of nominal actuator settings with relatively large strokes of ~ 0.2 µm peak-to-valley. The DM patterns have become an inherent part of diffraction control and would be used whether there were aberrations in the system or not. The occulter and DM patterns were optimized to provide reduced sensitivity to pointing errors assuming a pointing jitter as high as 1.6 mas rms per axis.[18]

The large DM strokes introduce significant mid-spatial-frequency wavefront variations that, while beneficial to achieving good overall contrast when combined with the occulter and Lyot stop, resulted in a degraded planet point spread function (PSF) with 4.3% total "PSF core" throughput (accounting for coronagraph mask losses).

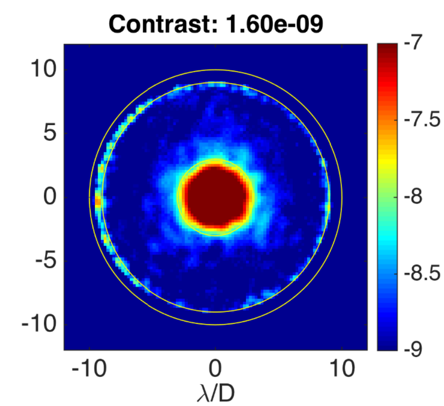

Figure 8: Static environment focal-plane image from the WFIRST HLC testbed in HCIT at JPL showing mean contrast of 1.6×10^{-9} at 10% broadband centered at 550 nm across a 3–9 λ/D dark hole (WFIRST; Milestone #9). The 10% bandwidth was achieved using five 2% bands averaged together; calibration uncertainty is ±2%.

Circularly symmetric masks (**Figure 9**) have been fabricated for the first time as a part of the WFIRST technology development and static performance demonstrations with the simulated telescope obscured pupil have already achieved a contrast of 8.5×10^{-9} at 550 nm with 10% bandwidth between angles 3 to 9 λ/D, as shown in **Figure 8** (WFIRST coronagraph technology Milestone #5). Wavefront control was achieved with two DMs and the dark hole region covered the full 360 degrees annulus.

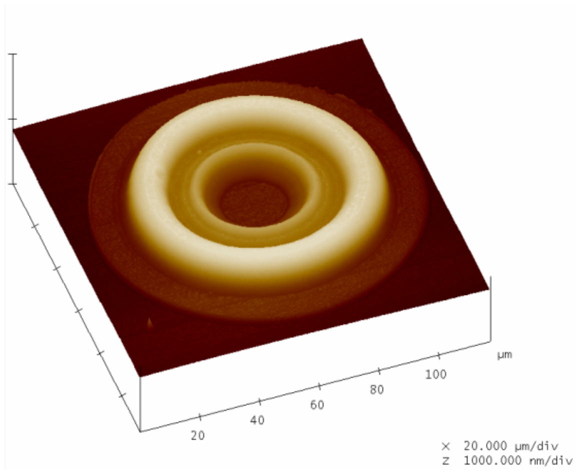

Figure 9: The WFIRST HLC focal plane mask is only 100 µm in diameter, composed of a flat nickel base layer and a super-imposed patternable dielectric layer made of PMGI (polymethylglutarimide). The mask was fabricated by e-beam lithography at JPL's Microdevices Laboratory.

B.2.3 Shaped Pupil Coronagraphs

A shaped pupil (SP) is a binary pupil-plane mask that blocks or passes light in different regions of the pupil and thus shapes the PSF of the coronagraph in the image plane to create dark, high-contrast regions. A field stop is usually placed at a focus between the SP and the camera to limit the dynamic range seen at the camera.

Early SP designs were optimized in 1D for open telescope apertures and could be manufactured as free-standing, through-hole masks. New designs for obstructed telescope apertures, such as that for WFIRST, require a 2-D optimization that produces non-freestanding opaque regions that must be placed on a substrate[19] (**Figure 10**). Ghosting and dispersion discouraged a transmissive glass substrate from being used for WFIRST, so the new SPs act in reflection off a thick silicon wafer with aluminum-coated regions that reflect light and black silicon regions that absorb light. The main challenges of manufacturing reflective SPs are achieving sufficiently low specular reflectance in the black silicon regions and not damaging the aluminum sections during the cryogenic etching process that creates black silicon (WFIRST coronagraph milestone #1).

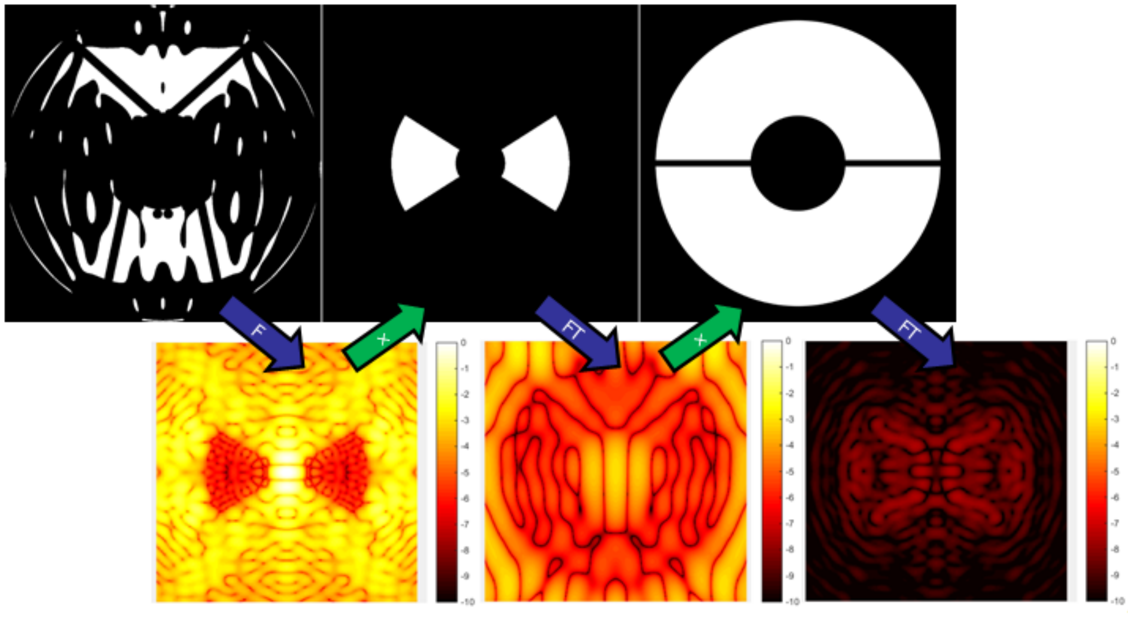

Figure 10: Shaped pupil coronagraph mask used to meet the < 10^{-8} contrast performance requirement on WFIRST. Demonstration was conducted in the HCIT-1 with the obscured WFIRST pupil under vacuum with no dynamic disturbances applied. The mask was fabricated at JPL's Microdevices Laboratory.

The SP used has a pupil transmission of 40% compared to the nominal obstructed aperture. No polarizers were used in these experiments.

Designs for WFIRST now include a diffractive focal plane mask and Lyot stop in a Shaped Pupil Lyot Coronagraph (SPLC)[20]. Such designs offer some of the robustness of a SP to low-order aberrations along with the improved performance (contrast, throughput, and/or IWA) of a Lyot-type coronagraph. WFIRST results with a reflective SPLC at 10% bandpass (five 2% filters) yielded a raw contrast of 8×10^{-9} in two bow-tie shaped regions between 2.8 and 8.8 λ/D (**Figure 11**). The WFIRST SPLC design has a PSF core throughput of 3.7%.

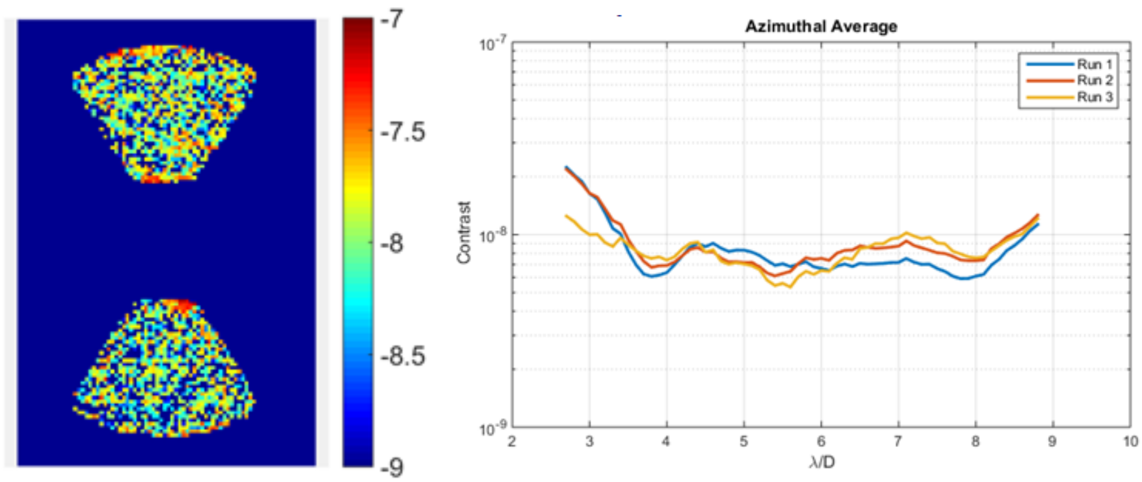

Figure 11: (Left) Focal-plane image from the WFIRST shaped pupil coronagraph testbed in HCIT-1 at JPL. (Right) 10% broadband result centered at 550 nm with mean contrast of 8×10^{-9} across a 3-9 λ/D two-sided 65° wedge dark hole (WFIRST; Milestone #5). The 10% bandwidth was achieved using five 2% bands.

B.2.4 Apodized Pupil Lyot Coronagraph (APLC)

The APLC/shaped pupil hybrid approach is based on the general APLC design[21] implemented on several ground-based telescopes (Gemini, Very Large Telescope, Palomar) with a pupil apodizer, a hard-edged focal plane mask, and a Lyot stop.[22,23,24,25] N'Diaye and Zimmerman have developed a novel approach to introduce image plane contrast metrics as the target of the optimization as is done for shaped-pupil type optimizations.[26,27,28] APLC/SP designs are extremely interesting for their very high tolerance to low-order aberrations including jitter and focus. For instance, the gray-scales designs introduced in N'Diaye et al.[29] are virtually insensitive to jitter or tip/tilt up to ±10 mas in simulation. Other tolerances can be included as part of the optimization process.

The conceptual development of the APLC has progressed rapidly under ExEP's SCDA study (see Section B.3.3) beginning in 2016.[30] Highlights include:

I. Creation of a software toolkit to automate the exploration of thousands of coronagraph design parameter combinations on a NASA computing cluster, and the completion of several large design "surveys." An example design evaluation is portrayed in **Figure 12**.
II. Integration of a Design Reference Mission (DRM) scientific yield metric into solution evaluations, which takes into account the full two-dimensional coronagraph PSF and intensity maps, including the effects of target star angular diameter.[31]
III. Proof-of-concept investigations into several strategies to improve the robustness of APLC designs to fabrication and alignment errors.

The Space Telescope Science Institute (STScI) team's comparison of APLC performance across the seven reference SCDA telescope apertures has already established major conclusions relevant to observatory architecture evaluation:

I. APLC performance is mainly driven by the presence and size of the central obscuration, and the deviation of the primary mirror perimeter from a circle. The struts and segment gaps considered by SCDA are geometrically thin enough (~1% or less of pupil diameter) such that performance is only weakly affected by the specific segmentation pattern within the telescope pupil.
II. The impact of the central obscuration on throughput and IWA is significant but does not pose a fundamental threat to mission objectives. In our preliminary DRM yield analysis, the number of exo-Earths detected with an obscured 12-meter diameter telescope is within 30% of the number detected by the same telescope aperture without central obscuration.

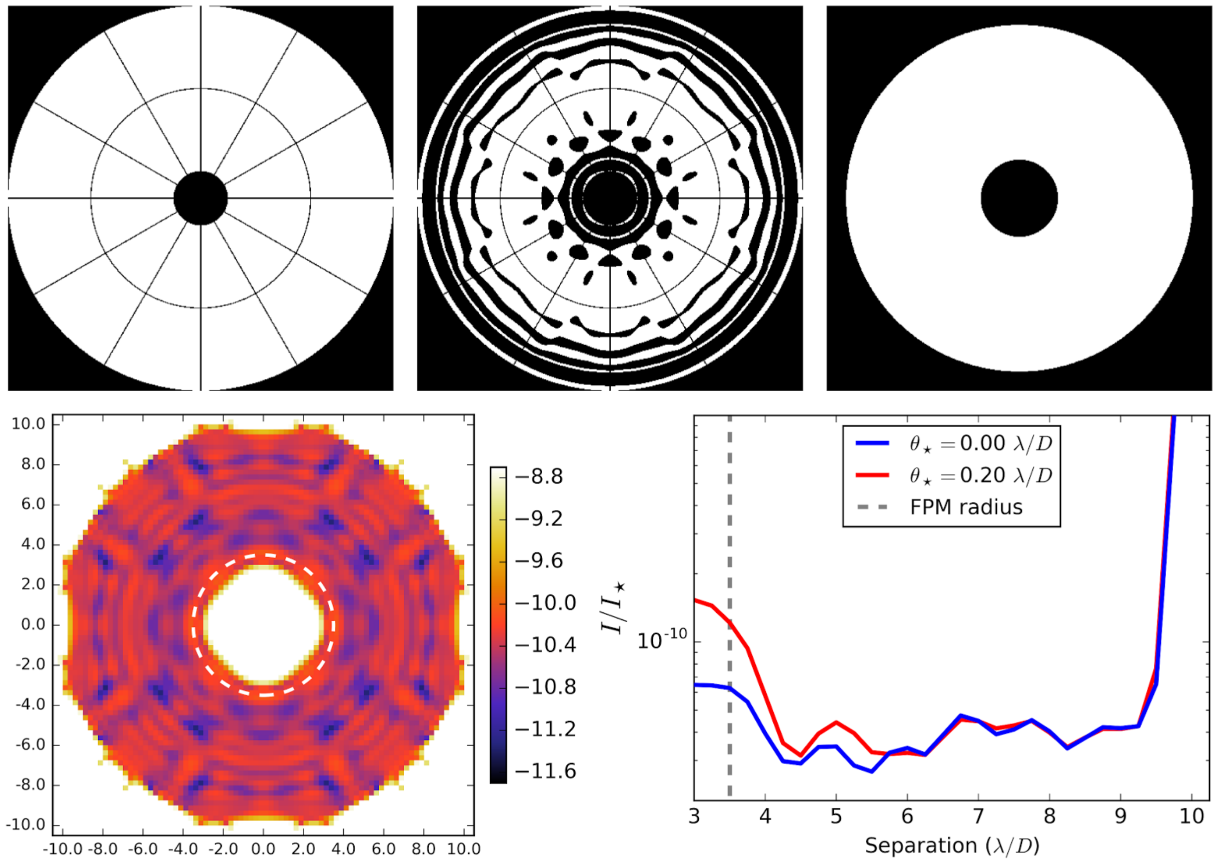

Figure 12: Example of an APLC design produced by the SCDA study for an obscured “Keystone-24” aperture, producing a 10^{-10} contrast dark zone with inner working angle 3.5 λ/D over a 15% bandpass. *Top row from left to right*: Telescope pupil, apodizer, and Lyot stop. Bottom left: ideal on-axis PSF. *Bottom right*: azimuthally averaged intensity, for an unresolved star (blue curve) and a star of angular diameter 0.2 λ/D (red curve), approximately equivalent to 2 mas for a 12-meter telescope at 600 nm.

For future APLC concept development, significant territory remains: parameter studies to achieve efficient designs at smaller IWA (≤ 3 λ/D, using spatially restricted dark zones and/or hybrids with different focal plane mask types); understanding the fabrication tolerances of shaped pupil apodizers for 10^{-10} contrast designs; relating aberration sensitivity to requirements on the observatory and the wavefront sensing & control system; how best to utilize deformable mirrors to offload alignment robustness and as an adjunct to reaching a given contrast goal.

Performance demonstration of the APLC is also being conducted on the HiCAT (High-Contrast Imager for Complex Aperture Telescopes) testbed under development at STScI to integrate wavefront sensing and control with starlight suppression by coronagraphy for telescopes with complex aperture shapes (i.e., in the presence of central obstruction, support structures, or segmentation). The testbed design has the flexibility to enable studies with increasingly complex telescope aperture geometries from off-axis telescopes, to on-axis telescopes with central obstruction and support structures (e.g., WFIRST), up to on-axis segmented telescopes concepts such as the LUVOIR. Hardware procurement, optical alignment and preliminary DM calibrations were completed in 2015. The testbed will ultimately include two Boston

Micromachine MicroElectroMechanical Systems (MEMS) DMs for wavefront control, as well as an Iris AO MEMS DM with 37 hexagonal segments to simulate a segmented aperture; it will also include a hybrid SP/APLC[32] with a reflective SP apodizer and a hard-edge circular focal plane mask. The testbed operates in air and is therefore intended to focus on a moderate-contrast, system-level integration to develop and demonstrate some of the key technologies for LUVOIR high-contrast imaging. The testbed will offer a flexible platform for system-level development and testing of LUVOIR high-contrast technologies, including segment phasing through a coronagraph, wavefront stability studies and segment vibration mitigation, low-order wavefront sensing (LOWFS), and optimization of broadband starlight suppression.

B.2.5 Phase-Induced Amplitude Apodization Complex Mask Coronagraph (PIAACMC)

Phase-Induced Amplitude Apodization (PIAA) is a technique for controlling diffraction that offers high throughput and small inner working angles.[33,34,35] Apodization of pupil amplitudes is achieved by a pair of aspheric mirrors absorbing no light aside from reflective losses. In a classic PIAA configuration, the mirrors have strong aspheric shapes and produce a PSF with very dark side lobes. PIAA designs have been further developed to incorporate diffraction at an occulting mask, producing the PIAA Complex Mask Coronagraph (PIAACMC), which can operate efficiently on obscured pupils[36] (see **Figure 13**). The PIAACMC under development as the backup design for WFIRST had much milder-shaped mirrors than the classic PIAA designs (reducing complexity and cost in their fabrication), and the occulting masks have phase-only surface patterns suitable for nano-fabrication.

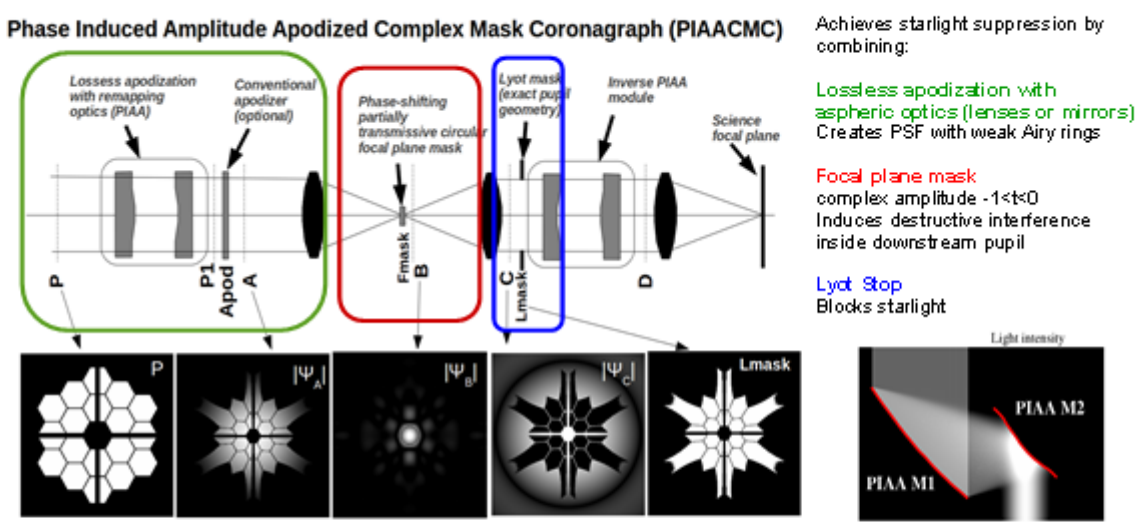

Figure 13: PIAACMC: The segmented input pupil is remapped into an apodized pupil. A phase focal plane mask creates a destructive interference inside the geometric pupil, moving all starlight outside the pupil.

Classic PIAA coronagraphs have been tested at the Subaru observatory in Hawaii, NASA Ames, and the ExEP's HCIT. In 2014, testing in the HCIT completed Guyon's TDEM-09 Milestone #1,[37] monochromatic contrast < 10^{-9}, and Guyon's TDEM-10 Milestone #3,[38] 10% broadband contrast < 10^{-9}. The monochromatic milestone was met with 6×10^{-10} contrast from 2–4 λ/D, while the broadband 10% milestone was not met but achieved 1×10^{-8} from 2–5 λ/D. Also in 2014, the

WFIRST project completed its Milestone #3, which was fabrication and characterization of a PIAACMC designed to meet the WFIRST coronagraph science requirements.

The WFIRST-PIAACMC "Gen-3" design is the best-studied PIAACMC design for an obscured pupil. A full PIAACMC-based optical system has been evaluated taking into account chromatic diffractive propagation between optics, static and dynamic wavefront errors in the telescope, demonstrated level of manufacturing errors (including diamond-turned PIAA optics and a focal plane mask made at JPL's MDL), and wavefront control (provided by a single 48×48 DM). Simulations predicted a 1.3 λ/D IWA with high throughput, delivering a 1.3×10^{-9} raw contrast in a 1-8 λ/D half dark hole in a 10% spectral band centered at 565 nm.

The raw contrast is currently dominated by manufacturing errors in the focal mask and telescope jitter (few mas per axis for the telescope, reduced to < 0.6 mas per axis after LOWFS correction). Advances in component manufacturing capabilities are expected to improve the raw contrast. At longer wavelength, these errors are a smaller fraction of a wave, so contrast values will be even better. The PIAACMC design promises better optical throughput and improved IWA of just 1.3 λ/D, creating the opportunity to search the HZ of more distant stars.

To meet the WFIRST project's Milestone #8, in 2016 the PIAACMC attempted demonstration of $< 10^{-8}$ raw contrast with 10% bandwidth centered at 550 nm in a static lab environment. As of November 2016, testing of the WFIRST PIAACMC had ended, with the team demonstrating contrast levels of 2.6×10^{-8} in monochromatic light, and 1.8×10^{-7} in a 10% band. The tip-tilt sensitivity resulting from the combination of optical components and DM wavefront control was not as successful as the model predicted. Reworking of the DM control algorithm, and/or using the measured DM performance to design a new occulting mask could potentially lead to further improvement in the contrast with this promising coronagraph design.

The WFIRST project will make a formal decision on its plans to continue with PIAACMC demonstrations in early CY17.

B.2.6 Vortex Coronagraphs

A vortex coronagraph consists of an image-plane mask that applies an azimuthal phase delay of two or more even-number of cycles to cause starlight to diffract outside of a downstream Lyot stop.[39,40] The vortex coronagraph offers broadband cancellation of a star while maintaining high sensitivity to faint companions at small angular separations.[41] In addition, the vortex phase mask may be readily designed to be robust to low order aberrations, jitter, and stars with non-negligible angular diameter.[42]

Laboratory demonstrations of vector vortex coronagraphs have achieved raw starlight suppression levels of 10^{-9} or better at angles of 2 λ/D in the HCIT[43] and an average contrast of 10^{-8} across 1.5–9.5 λ/D for 10% bandwidth light. Several major ground-based facilities have vortex coronagraphs that operate in the mid-infrared by means of sub-wavelength annular groove phase masks[44] as well as in the visible/near-infrared using liquid crystal polymers.[45]

Eugene Serabyn (JPL), with a 2010 TDEM award, demonstrated mean raw contrasts of 3.2×10^{-8} with a 10% bandwidth in a 60 $(\lambda/D)^2$ field extending from 2.4–9.4 λ/D.[46] His team later demonstrated contrast performance 4.3×10^{-10} in monochromatic light. Serabyn was awarded a TDEM-14 to continue unobscured vacuum demonstrations at 10% and 20% broadband. Testing will begin in the spring of 2017.

The vortex coronagraph is being studied as part of the ExEP SCDA task. Due to its widespread implementation on various on-axis (and thus obscured) ground-based telescopes, the question of unfriendly apertures was considered early on. Several solutions have been proposed such as the multistage vortex coronagraph[47] and various apodization methods, including gray scale,[48,49,50] binary shaped-pupil,[51] phase-induced pupil remapping,[52,53] and Lyot plane phase masks.[54] These solutions provide leverage against the detrimental effect of obscured apertures (including spiders and segments). Both the multistage and gray-scale apodized vortex coronagraphs have been tested in the lab and on-sky with ground-based telescopes.[55] Apodized vortex coronagraphs for segmented aperture space telescopes will be validated on the High Contrast High-Resolution Spectroscopy for Segmented Telescopes Testbed (HCST)[56] at California Institute of Technology in 2017. The theoretical performance of an apodized vortex coronagraph is shown in **Figure 14** for a favorable aperture geometry, which demonstrates high throughput and capacity to suppress stars with angular diameter up to 0.1 λ/D (or ~1mas for a 12m space telescope in the visible). However, the throughput and robustness to jitter, stellar diameter, and aberrations depends on the aperture geometry, where the best performance is typically obtained for on off-axis (unobscured) telescope architectures.

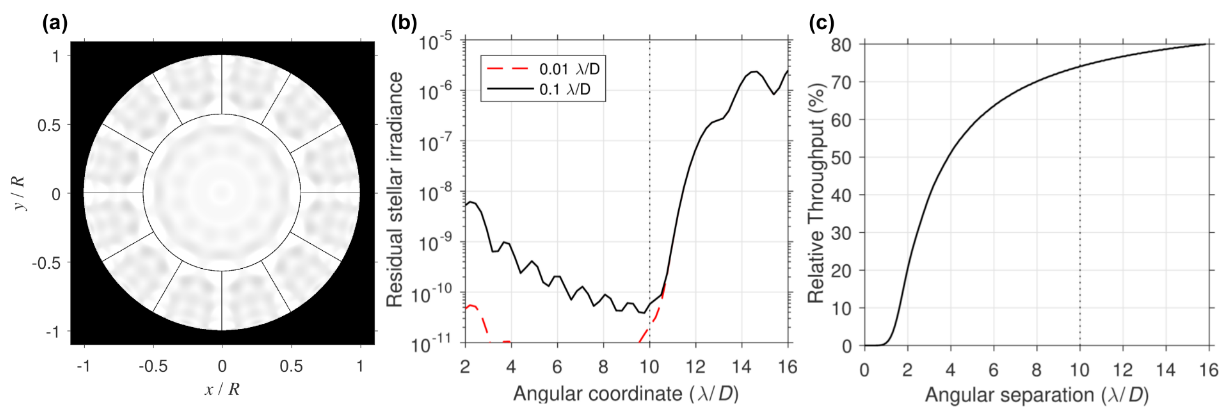

Figure 14: Example of a charge 6 apodized vortex coronagraph design for an off-axis (unobscured) segmented aperture telescope. (a) The apodization pattern. (b) The residual stellar irradiance after the coronagraph for stars with angular diameters of 0.01 λ/D (dashed) and 0.1 λ/D (solid). (c) The relative throughput for an off-axis point source, calculated within 0.7 λ/D of the source position.

The optical configuration is essentially identical to that of the Hybrid Lyot coronagraph architecture. No fundamental change to the mask design would be needed for flight (although material compatibility assessment in a radiation environment is still needed). The current limitation in performance is related to the ability to manufacture masks with a vortex pattern that is maintained to very small offsets from the center of rotation, and to extend the designs to broadband multilayer masks. For the current experiments, a polarizer is required prior to the pinhole of the source.

The throughput would ideally be 100%, but the Lyot stop was undersized to 85% for the monochromatic demonstrations and to 92% for the broadband demonstrations, yielding a 72%

and 85% transmission, respectively. Additionally, a polarizer is used at the source (as mentioned above), and so the effective throughput is approximately 36% monochromatic and 43% broadband.

B.2.7 Visible Nulling Coronagraphs

A Visible Nulling Coronagraph (VNC) splits light from a telescope into one of two outputs via optical interference. A broadband optical delay is paired with an Iris AO PTT489 DM with 163 piston, tip, and tilt controllable segments that can be used to control coupling into an array of single-mode optical fibers for optimal minimization of starlight in the “dark” output where high-contrast measurements are made. By energy conservation, the signal in the second “bright” output is maximized, and wavefronts in both outputs are sensed to provide active feedback for control of the DM and broadband delay. Lab demonstrations to date have produced a wedge-shaped dark hole in the region of 2–5 λ/D. A larger outer working angle would be achieved using a DM with at least 300, but preferably 925 segments. Modeling will be required to determine if a flight configuration would use 1) an array of single-mode fibers paired with a matched-geometry DM, each having the same number of fibers and segments, respectively, or 2) two DMs. Both options enable simultaneous control of phase and amplitude errors over full azimuthal coverage in the focal plane. A fiber array has been used to demonstrate coherent imaging, but has not been used in the high-contrast demonstrations reported here.

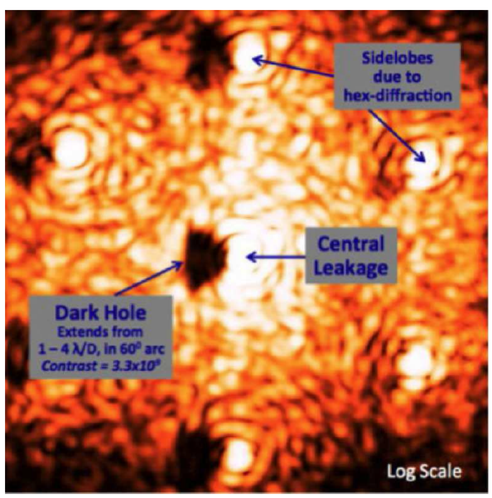

Figure 15: Focal plane image of Visible Nulling Coronagraph from TDEM-09 result by Mark Clampin and Richard Lyon (NASA-GSFC).

Mark Clampin and Richard Lyon (NASA-GSFC), with their 2009 TDEM (TDEM-09) award, demonstrated[57] mean raw contrasts of 5.7×10^{-9} with a 1.2 nm wide bandpass center on 632.8 nm over a 1 λ/D diameter circular field extending from 1.5–2.5 λ/D. Broadband efforts from Lyon’s 2010 TDEM were not able to further advance previous contrast or IWA performance (results are summarized in their Final Report approved by the ExoTAC in July of 2016[58]). A 2013 TDEM led by Brian Hicks (NASA-GSFC) intends to accomplish the goals not met in the TDEM-10 and use their VNC with a segmented pupil consisting of controllable mirrors to demonstrate starlight suppression for a simulated segmented mirror telescope.[59] A 2014 TDEM led by Matthew Bolcar (NASA-GSFC) intends to build the Next Generation Visible Nulling Coronagraph, an evolution of the VNC concept that demonstrates off-axis transmission.[60] Commencement of work on this TDEM is contingent on successful performance of the TDEM-13 effort. Hence

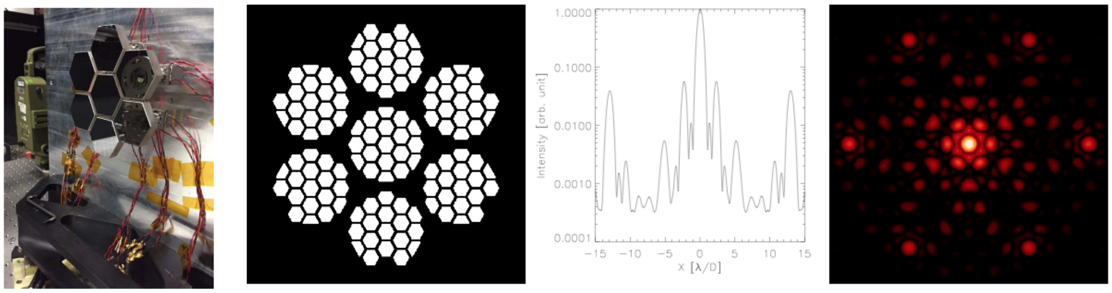

Figure 16 (left to right): the VNC TDEM-13 segmented telescope primary, the Lyot mask formed by the primary overlaid with a PTT489 DM, and a cross-section and stretch of the corresponding point spread function.

proposals for TDEM funding for VNC-based architectures as described here are not sought under TDEM-16.

B.3 Wavefront and Structural Stability Demonstrations and Assessments

In order to achieve 10^{-10} starlight suppression needed to directly image and characterize Earth-like exoplanets, a telescope/coronagraph system must conduct long integration observations requiring sub-nanometer wavefront stability. There are many important component and subsystem contributors to this stability, as captured in a number of items on the ExEP Technology Gap List (in particular CG-1, CG-6, CG-7, CG-3, CG-5 and CG-9). These subsystem performances are inter-dependent and can be traded between each other. Therefore, a systems-level view is particularly interesting; “Wavefront Stability Demonstrations and Assessments” are included in the TDEM component of the 2016 SAT. Component-level investigations are also of interest if they can be shown to have wavefront and structural stability applications across multiple telescope/coronagraph architectures.

B.3.1 Large Aperture Mirrors (CG-1)

The habitable zone of an exo-Earth at 10 pc has an angular resolution of 100 mas at planet quadrature (see **Figure 1**). To just detect such a planet at 400 nm, a telescope should have an angular resolution of 25 mas if we conservatively assume a 3 λ/D coronagraph. This telescope would then have a primary mirror aperture that is 3.3 m. However, our end objective is spectral biosignatures. Imposing the same parameters for detecting the planet at 760 nm (oxygen line) would require a 6.3-m telescope; water at 940 nm would require a telescope aperture approaching 8 m. Improvements in inner working angle can help drive the aperture size down, as would investigations of our solar neighborhood limited to within 10 pc.

Large primary mirrors enable more than just improved angular resolution, they enhance planet sensitivity due to sharper PSFs, reduce science integration time due to greater collecting areas and throughput, and enable probing of a larger number of more distant stars’ habitable zones. The telescope’s primary mirror size and architecture (monolithic or segmented, obscured versus unobscured) is among the most important decisions a space telescope team will have to make, especially when considering optimizing the performance of a coronagraph.

The biggest unknown needed to select the telescope size is the fraction of Sun-like stars with Earth-size planets in their habitable zones, also known as η_{Earth}. As η_{Earth} increases, sufficient statistics about the habitability of exoplanets can be built with fewer observations of planetary systems. If η_{Earth} is near 0.1, then a 10-m-class telescope is required to detect and characterize approximately 30 candidate habitable zones for exo-Earths[61]. If η_{Earth} is above 0.8 then only a 4 m-class telescope would be required to detect and characterize the same number of candidate habitable zones. η_{Earth} is expected to be better constrained in 2017, based on additional analysis of the Kepler data.

Proposals for the development of large aperture mirror and associated technologies are solicited under the TDEM element of the SAT 2016 call as part of a systems-level study. Specific technology development in this area may be suitable for the Technology Development for the Cosmic Origins Program (TCOP) element of the SAT 2016 solicitation or under the APRA 2016 solicitation. Proposers should contact the cognizant program officer to confirm the suitability of their investigation for those programs in advance of submitting a proposal.

B.3.2 Large Monolithic Mirrors

The maximum size monolithic mirror has been limited to approximately 4 m by currently available 5-m-class launch vehicle fairings. For example, the largest monolithic space telescope ever flown is the Herschel Telescope and its primary mirror is 3.5 m. Fortunately, with the advent of NASA's Space Launch System (SLS) and its planned 8.4- and 10-m fairings, it is possible to consider monolithic 4- to 8-m-class mirrors. Mirror mass and diameter traditionally have been key telescope design parameters, especially with respect to cost. This has led to light-weighting technologies that continue to this day. But the SLS's larger fairings and greater mass capacity may allow designers to reconsider the benefits of more mass in the overall system (greater stiffness, lower resonance frequencies, greater thermal inertia, etc.). It is expected that the 2020 Decadal Survey will consider large monolithic mirror (> 4 m) mission concept studies that can fit in 5-, 8.4-, and 10-m fairings.

Thermal stability and control is a key challenge for monolith mirrors. HST had the challenge of the diurnal thermal cycle of low-Earth orbit. While any future large space mission will probably be in the thermally stable Earth-Sun L2 Lagrange orbit, there will still be thermal load variations as a function of pointing angle relative to the Sun (as shown on JWST). Analysis indicates that exoplanet science requires a primary mirror that has a total wavefront error that is stable on the order of 10 pm per wavefront control step.[62]

No previous space telescope has ever required < 10 pm wavefront stability. Historically, space telescopes use passive thermal control. JWST's telescope is in a Sun-shade shadow. HST's telescope is in a heated tube. And again, while not designed to meet the requirements of a UVOIR exoplanet science mission, JWST is predicted to have a 31 nm rms WFE response to a worst-case thermal slew of 0.22 K and take 14 days to passively achieve < 10 pm per 10 min stability. Obviously, this is too long for a coronagraphic exoplanet mission. HST is a cold-biased telescope heated to an ambient temperature. However, it is not a controlled thermal environment. Thus, HST's wavefront error changes by 10–25 nm every 90 min (1–3 nm per 10 min) as it moves in and out of the Earth's shadow.

The HabEx mission concept study team is exploring the scientific benefits and technology needs of large monolith primary mirrors.

B.3.3 Large Segmented Mirrors

The development of large segmented mirrors and their structures will enable astronomy to build ever-increasing large telescopes advancing both exoplanet and general astrophysics science. However, segmented mirrors have their own challenges for reaching previously unmet contrast ratio levels of 10^{-10} at close IWAs. These challenges include: diffraction from the segmentation pattern and segment to segment rigid body motion (i.e., tip/tilt and piston).

JWST is a segmented aperture telescope scheduled for launch in 2018. Its primary aperture is 6.5 m in diameter composed of 18 gold-coated beryllium segments, each 1.32 m tip-to-tip. Working in the near- to mid-infrared, the telescope operates at a temperature below 50 K. A major cost driver of JWST was the need to verify and validate performance specifications at the 50 K operating temperature. Fortunately, by operating at a warmer temperature, due to its visible to near-infrared observational spectrum, a potential exoplanet imaging mission can use more conventional materials for its optical components and structure.

The experience of controlling 6 degree of freedom (DOF) segments can be built upon to gain a higher precision, more stable segmented aperture for exoplanet imaging. The surface figure error is required to be less than 10 nm rms and drift less than 10 pm due to thermal and dynamic instability during a wavefront control cycle. Possible design architectures include the ATLAST (Advanced Technology Large Aperture Space Telescope) design[63] and the High Definition Space Telescope (HDST) concept.[64]

To advance the understanding of coronagraph performance with segmented telescope apertures, the ExEP launched in FY16 a Segmented Coronagraph Design and Analysis task to provide a first look at current capabilities and what potential future developments may yield. Although not a down-select, five state-of-art coronagraph architectures using 6–7 segmented reference aperture architectures (**Figure 17**) will be designed by coronagraph experts and submitted to the ExEP for consistent analysis and exoplanet yield based on contrast and IWA performance. This initial study will not include telescope dynamics (e.g., jitter, thermal, segment-to-segment phasing errors) but rather study what can be achieved with a static aperture. A finite stellar angular diameter (~1 mas) will be assumed, which is expected to exceed the residual corrected telescope jitter achieved by a coronagraph’s low-order wavefront sensor and control. The coronagraph architectures to be studied in the initial analysis will be:

1. PIAA CMC (University of Arizona/NASA-Ames/JPL)
2. APLC/SPC (Space Telescope Science Institute/Princeton)
3. Vortex (Caltech/JPL)
4. Hybrid Lyot (Caltech/JPL)
5. Visible Nulling Coronagraph (NASA–GSFC)

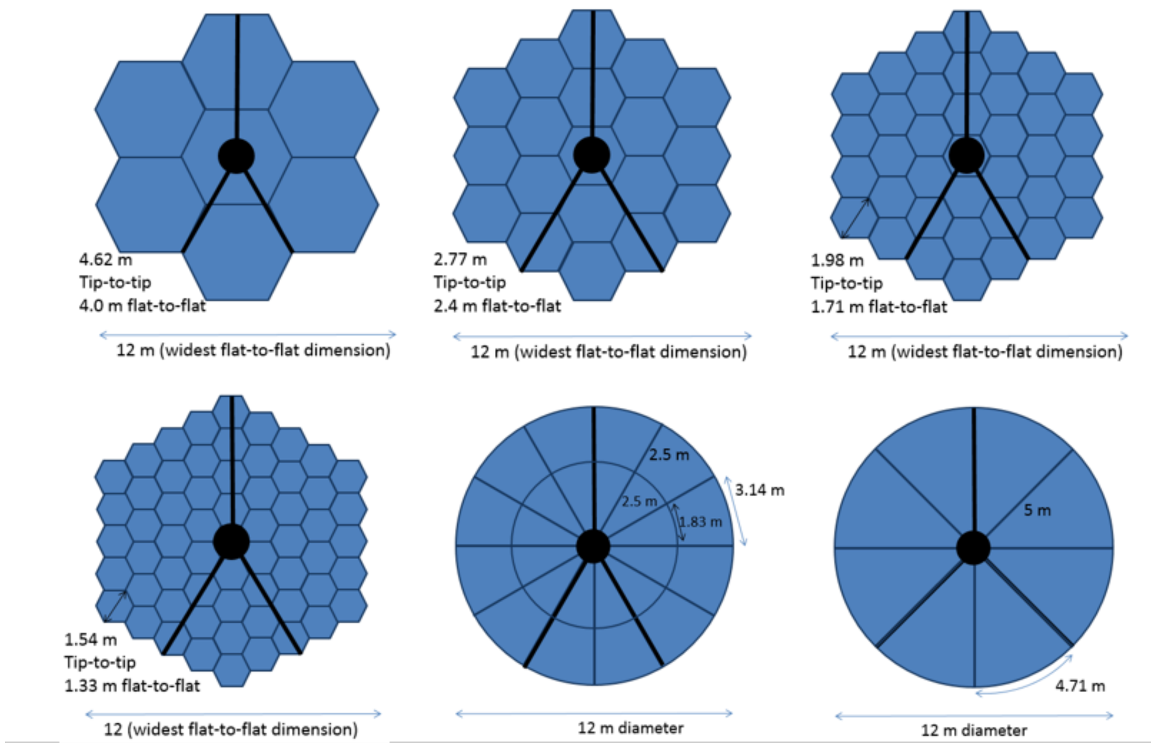

Figure 17: 12 m aperture designs being considered for the ExEP Segmented Coronagraph Design and Analysis study.

The HabEx and LUVOIR mission study teams are exploring the science benefits and technology challenges of segmented primary mirrors.

B.3.4 Mirror Figure / Segment Phasing Sensing and Control (CG-6)

Unlike a traditional monolithic telescope mirror, a multi-segment large-aperture mirror will require phasing and rigid-body sensing and control of the segments to achieve tight static and dynamic wavefront errors at visible wavelengths. Wavefront errors caused by segment rigid body positioning errors, dynamic vibrations, and slow thermal drifts can significantly impact coronagraph coherent imaging and hence contrast. For example, a coronagraph working with a segmented mirror, to avoid speckle noise brighter than typical exoplanets, requires a segment-to-segment dynamic co-phasing error of under 10 pm rms between WFSC updates (from a few minutes to many tens of minutes depending on the host star's brightness).

A segmented tertiary DM could also provide segment phasing and jitter control. Segment position and phase errors sensed by a wavefront sensor can be sent to the segment rigid body actuators (for coarse correction) and to the DMs of the coronagraph, or a segmented DM dedicated to fine segment tip/tilt and phasing control (for fine correction).

The Keck ground-based telescope and JWST sense and control the rigid-body positions of their segments by utilizing wavefront sensing and control, such as phase retrieval, Shack-Hartman sensing, and dispersed fringe sensing.[65] Keck also uses edge sensors. JWST's optical error budget includes 6 nm rms for rigid body positioning and 49 nm rms stability. While these methods are proven for phasing diffraction-limited segmented optical systems such as JWST, Keck, and the Thirty Meter Telescope, it remains to be seen if they can achieve the picometer-level stability required for exoplanet imaging at visible wavelengths.

A potential solution is a laser metrology truss to measure positional changes of the large optics to the expected pm-level stability requirements. Picometer-accuracy laser metrology was demonstrated by the Space Interferometry Mission (SIM) with large beam launchers. More compact beam launchers, lightweight enough to mount to the edges of segments, have been developed over the last few years for non-NASA customers but were designed to operate at the nanometer-precision level. Additional development in laser metrology is needed if a laser metrology truss is to be used for sensing segment positioning.

Future work defining requirements and architectures is being explored by the HabEx, LUVOIR, and OST mission concept studies that commenced in 2016.

B.3.5 Telescope Vibration Sensing and Control (CG-7)

Isolation and damping of spacecraft and payload vibrational disturbances is critical in enabling a coronagraph to reach 10^{-10} contrast levels at IWAs less than 3 λ/D. Leakage of starlight due to pointing instability or jitter and vibration in the telescope that exceed the control range of the coronagraph's low-order wavefront sensor and controller (LOWFS/C) will potentially scatter light onto the imaging detector and decrease the detection contrast within the dark hole. Precision pointing stability needed by the telescope during integration to keep the star inside the correction capabilities of the coronagraph may need to be better than a few mas[66] (depends on LOWFS/C capability; see Section B.3.7) Typical expected attenuations for monolith primary mirrors are 120 dB end-to-end attenuation at frequencies larger than 20 Hz; segmented primary mirrors are 140 dB end-to-end attenuation at frequencies greater than 40 Hz.[67,68] "End-to-end" implies isolation between disturbance source and the optical telescope element.

Several aerospace companies have demonstrated systems that allow for active dynamic isolation candidates. A noncontact isolation system by Lockheed Martin[69] demonstrated 68 dB of broadband isolation in a testbed and is self-assessed at TRL 5 for large observatories. The payload and spacecraft bus are separate bodies that fly in close-proximity, allowing precision payload control and simultaneous isolation from spacecraft disturbances. Micropropulsion thrusters for fine pointing, used exclusively or in a hybrid fashion with reaction wheels, is another option. Active vibration dampening and hybridizing the LOWFS/C fast steering mirror system with the fine guidance system are also credible.[70]

Telescope stability, like wavefront stability in general, is a systems-level challenge and is most efficiently addressed by a reference design that includes selected coronagraph and telescope architectures. Future work in defining requirements is expected within both the LUVOIR and HabEx mission concept studies. In addition, characterizing the WFIRST transmitted disturbances to the coronagraph instrument will be valuable for understanding the threshold disturbance the coronagraph LOWFS/C can attenuate.

B.3.6 Deformable Mirrors (CG-3)

High-contrast stellar coronagraphs depend on deformable mirrors (DMs) to (1) create dark regions where the starlight is suppressed sufficiently to observe companion planets at the detector's image plane and (2) maintain the dark region (stability). Creating dark regions requires removing both the natural effects of diffraction as light interacts with the telescope aperture and its optics as well as modulate and remove the residual scattered starlight (aka speckles) due to imperfections in the telescope and coronagraph optics. DMs maintain speckle stability in the dark region by correcting for the relatively slow thermal drifts the observatory will experience in its orbit during science observations.

The next generation of high-contrast coronagraphs will rely even more on DMs as they play critical roles in achieving two-sided symmetric dark regions (improving exoplanet search space) and, in some cases, the DMs can be "pre-shaped" to work in concert with the coronagraph masks to mitigate the diffraction effects of obscured apertures.[71,72]

To achieve two-sided symmetric dark regions in the focal plane, some coronagraphs will require two DMs to operate in series allowing for both amplitude and phase error corrections. This was first achieved in the HCIT by Jeremy Kasdin's TDEM[73] in 2013 reaching raw contrasts of 3.6×10^{-9}. In 2015, the WFIRST study used two DMs in both their coronagraph testbeds (shaped pupil and hybrid Lyot) achieving broadband contrasts less than 10^{-8} with the obscured telescope pupil.

The WFIRST coronagraph will use two 48×48 element electrostrictive lead magnesium niobate (PMN) DMs made by Adaptive Optics Associates Xinetics in Devens, MA, a subsidiary of Northrop Grumman. These mirrors have been routinely used in the HCIT vacuum testbeds since 2003. With a 500 µm actuator stroke, they have participated in all the HCIT demonstrations better than 10^{-9} with unobscured pupils. These DMs are built up from electro-ceramic blocks with actuators separated by 1 mm (see **Figure 18**). These blocks are assembled into modules covered by a single-mirror facesheet and driven by a Gen 5 voltage supply (not multiplexed) with 100 V range and 16-bit resolution. One Xinetics DM has already successfully undergone a 3-axis random vibration test to 10.8 G rms.

WFIRST will help advance the DM state-of-the-art over the next few years. Expected activities include:

- Flight qualifying the drive electronics
- Redesigning the electronic interconnects to the actuators
- Miniaturizing the drive electronics
- Improving the facesheet surface figure error so as to gain more stroke
- Life test the DM actuators
- Complete environment testing including thermal, dynamic, and radiation testing

Future DM needs for larger space telescopes will include larger format sizes, stability, and stroke and pitch sizes. Larger format DMs allow for larger outer working angles for debris disk science as well as probing the closest exoplanetary systems. Format needs for 4 m-class telescopes may be 96×96 actuators and 10m-class telescopes may even request 128×128 actuators or larger. Larger Xinetics DMs have been built through mosaicking smaller units. A

64×64 actuator device has operated successfully in the HCIT for over a decade. This larger format was achieved by mosaicking four 32×32 ceramic blocks. A 66×66 unit has also been mosaicked from 11×11 units for the Palm 3000 adaptive optics system at the Palomar Observatory. It is expected that the same technique could be used to meet future large format DM needs although no investments have been made. The challenge is believed to not be the mosaicking of 48×48 devices or 32×32 devices (to reach 128×128) but rather dealing with the enormous number of interconnects and their electronics.[74]

Wavefront aberrations less than 1/10,000th of a wave will have to be maintained in a coronagraph if contrasts of 10^{-10} are to be achieved. At visible wavelengths, this implies wavefront control at sub-angstrom levels. To measure the DM surface figure errors along with other key parameters, WFIRST and the ExEP have upgraded an existing testbed, the Vacuum Surface Gauge, which is intended to characterize all flight and non-flight DMs. The Vacuum Surface Gauge is a customized Michelson interferometer that can measure both accuracy and stability of DMs along with other key parameters such as wavefront stability, cyclic errors, cross talk, and hysteresis. This testbed has demonstrated optical surface measurement accuracy less than 100 pm rms, becoming a premier ExEP facility instrument for the community.

There is also interest in smaller pitch (< 1 mm) to reduce the size of the optical beam and hence the optical train and in larger stroke (> 500 nm) devices.

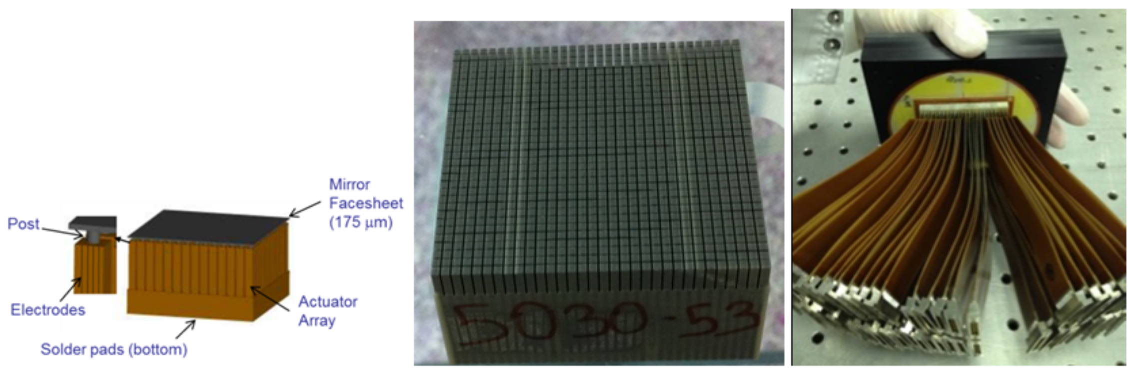

Figure 18: (Left) Schematic of the bulk ceramic block with cut actuators mounted to a facesheet. (Center) Bulk block with 1 mm cut posting actuators. (Right) Connector cables extending from the back of the DM.

Alternative DMs are the MEMS devices fabricated by Boston Micromachines Corp (BMC). These DMs are made of a polysilicon membranes coated with one or more layers for the reflective surface and are actuated by 32×32 or 64×64 electrostatic actuators on the backside. BMC offers both continuous face-sheet and segmented mirrors. Pitch sizes come less than 0.5 mm and maximum stroke is about 5 µm for 250 V drive voltage.

Iris AO DMs are MEMs devices with three electrostatic actuators underneath a segmented mirror surface. The three actuators provide piston, tip, and tilt to a segment. The hexagonal segments are 700 microns wide, vertex to vertex. The actuators are long stroke (8 µm or 5 µm, depending on the model) over 200 V. The small step precision is limited by electronics digital/analog bit depth. The current Iris AO built electronics are 14 bits, but 20 bit super-resolution electronics are in development. Their environmental testing TDEM is expected to complete in CY17. An Iris AO MEMS DM has demonstrated a monochromatic raw contrast of 5×10^{-9} over angular separations of 1.5–2.5 λ/D using a Visible Nulling Coronagraph at GSFC.[75]

There are currently no plans to advance MEMS DMs with WFIRST further than what is being done through the TDEM program. Two separate TDEM awards were funded to BMC and Iris AO to continue environmental testing of continuous facesheet DMs as well as segmented DMs, respectively. The goal of these TDEMs is to better characterize their failure modes, and thus raise the TRL of the respective DM models. BMC is expected to complete environment dynamic testing and present their results in CY17. In the past, they have undergone partial environmental testing[76] and have flown on a sounding rocket experiment,[77] although in the latter case, no performance data was acquired.

The development of segmented DMs to be used in conjunction with segmented apertures may provide additional wavefront error control. A segmented DM can provide pure segmented mode correction for segment tip-tilt-piston errors with large stroke and without cross-talk or aliasing (which may occur when using a continuous face sheet DM to do the segment mode correction). Segmented DMs can also be adapted with figure control to further drive wavefront errors down and potentially relax other telescope stability requirements. This will require a systems-level trade study. A segmented DM could be a third DM in the optical train or replace one of the two in series.

B.3.7 Wavefront Sensing & Control (CG-5)

Focal plane speckle suppression algorithms (single star)

A coronagraph suppresses starlight diffraction (e.g. Airy rings) and can suppress any other stellar leak that is static and known a priori. However, usually this still leaves random speckles (static, quasi-static, and dynamic) that are not known a priori at contrast levels on the order of 10^{-6} to 10^{-4}, depending on the optical component quality. An adaptive optics (AO) system is necessary if better contrasts are required. Unlike conventional ground-based AO, high contrast AO for space missions is typically accomplished by using a focal-plane based Wavefront Control (WFC) system in order to avoid non-common path errors. A deformable mirror (DM) is used to provide the necessary measurement diversity in focal-plane images as well as to subsequently remove the speckles. A simple and robust algorithm called Speckle Nulling was developed and used at HCIT.[78] Although it still remains in use, more advanced model-based algorithms were subsequently developed that take advantage of the system model in order to achieve faster convergence and often deeper contrasts: for example, Energy minimization,[79] Electric Field Conjugation (EFC),[80] and stroke minimization.[81] Sometimes the term "EFC" is used to describe this entire class of algorithms. More recently, algorithms based on the Kalman filter have been proposed, which take advantage of prior control history to achieve even faster and better results than EFC, when properly tuned. Great success has been achieved in testing these technologies for a variety of coronagraphs in several laboratory testbeds, including contrasts of $\sim10^{-8}$ in broadband light at NASA JPL's HCIT (at modest inner working angles), and inner working angles as aggressive as 1.2 λ/D in broadband light at NASA ARC's ACE as well as Lockheed Martin ATC vacuum testbed (at modest contrast levels).

Challenges still remain, however, especially in the area of achieving faster wavefront control in the presence of realistically low light levels. Existing systems are believed to still be orders of magnitude away from the information-theoretic limit on algorithm efficiency and can thus in theory be significantly improved in terms of speed. Other areas of improvement include achieving control in a wider wavelength band, even deeper contrasts, and in multiple polarization channels.

Multi-star wavefront control

The majority of non-M-dwarf stars are in multi-star systems. For example, within 4pc there are 5 multiples (α Cen, Sirius, Procyon, 61 Cyg, ε Ind) and only 2 singles (ε Eri, τ Cet). Some of the multiples have a separation large enough that the leak from the companion is negligible, but there are many cases for which current single-star high contrast techniques are insufficient. A particularly important case is Alpha Centauri, which is 2.4 times closer than any other Sun-like star.

Although it is important to baffle the off-axis star for practical reasons, a baffle or a coronagraph does not remove random speckles from the off-axis star in the region of interest around the on-axis star. Therefore, wavefront control of both stars is necessary, while coronagraphic suppression of the second star is not sufficient and may not be necessary. A multi-star wavefront control system without a coronagraph may be sufficient if the second star is ~10 λ/D away or greater, because at that distance, wavefront control can suppress diffraction and Airy rings along with random speckles. The main challenge in wavefront control of 2 or more stars comes from the fact that light from two stars is incoherent with respect to each other. Thus, a wavefront control system must suppress speckles from both stars independently and simultaneously. This appears to be possible and a technique called "multi-star wavefront control" has already been demonstrated.[82] This technique also does not in principle need any changes in hardware of existing space mission designs like WFIRST, LUVOIR, and HabEx (although it could benefit from a mild "print-through" pattern commonly found on many DMs, or another mild grating in the system). However, further development is necessary to bring this technique to TRL4+, or in general to advance any method for binary star imaging.

Low-order Wavefront Sensing and Control

The coronagraph's low-order wavefront sensor and control (LOWFS/C) is the critical component for achieving contrast stability during science measurements. It utilizes the bright starlight rejected by the coronagraph optics or the out-of-band light not used by the coronagraph as the source of information to sense and maintain the state of the optical wavefront established by the high contrast imaging wavefront control (WFC). The starlight wavefront is sensed at high temporal frequency to suppress vibration-induced fast line-of-sight errors besides attitude control system (ACS) pointing drift or inter-segment vibration for a segmented telescope. LOWFS/C also senses and corrects low-order wavefront aberrations due to telescope thermal drifts.

Future space missions for direct exo-Earth imaging will likely require wavefront stability of 10s of pm over update rates around 10 minutes to achieve a dark hole contrast close to 10^{-10}. They will have to be able to sense and correct fast line of sight jitter (tip/tilt), and, with a large segmented telescope, fast segment mirror tip/tilt/piston jitter, as well as several low-order, thermally-induced wavefront error modes. Alternatively, or in addition, future missions will need to be able to passively isolate or dampen such motions below the required wavefront stability (see Section B.3.5).

A first step in this direction was accomplished with the development of the PIAA coronagraph system in the HCIT- 2 in 2013. Sub-mas pointing stability was demonstrated in vacuum with a servo system, with the intent of eventually expanding it to demonstrate low-order wavefront sensing and control.[83]

WFIRST has carried out a series of laboratory demonstrations of a LOWFS/C subsystem which uses a Zernike wavefront sensor (ZWFS) that provides information for tip/tilt control using a fast steering mirror and low-order wavefront correction using the coronagraph DMs.[84] This effort is considered to be the state-of-art for high-contrast imaging coronagraphs. As a part of the WFIRST technology development effort, lab tests have demonstrated a line-of-sight post-correction residual of < 0.5 mas in the presence of line-of-sight jitter and ZWFS low-order wavefront error sensitivity of ~ 10 pm. Performance against focus, tip, and tilt errors was demonstrated in 2015 by the WFIRST coronagraph team (Milestone #6) where a 14 mas line-of-sight input error was attenuated to a residual error below 0.5 mas rms per axis (**Figure 19**). Testing for WFIRST coronagraph technology Milestone #9 (expected to be met in early 2017) integrated the ZWFS with the WFIRST coronagraphic mode and demonstrated contrast levels of order 10^{-8} at working angles from 3 - 9 λ/D while the optical input delivered to the coronagraph included simulated flight environment dynamical disturbances. See **Figure 20** for preliminary results.

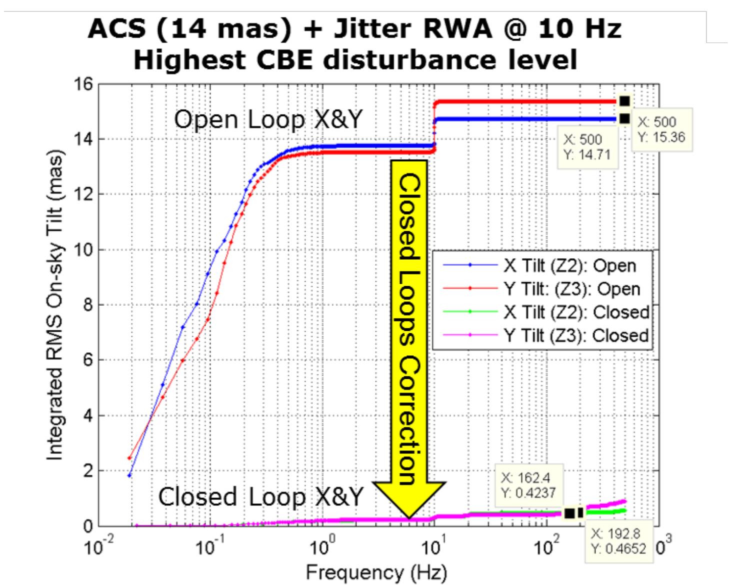

Figure 19: WFIRST coronagraph results from their Milestone #6 Technical Assessment Committee review. Sensor and correction was for tip/tily disturbances only using a fast steering mirror and a simulated WFIRST telescope aperture.

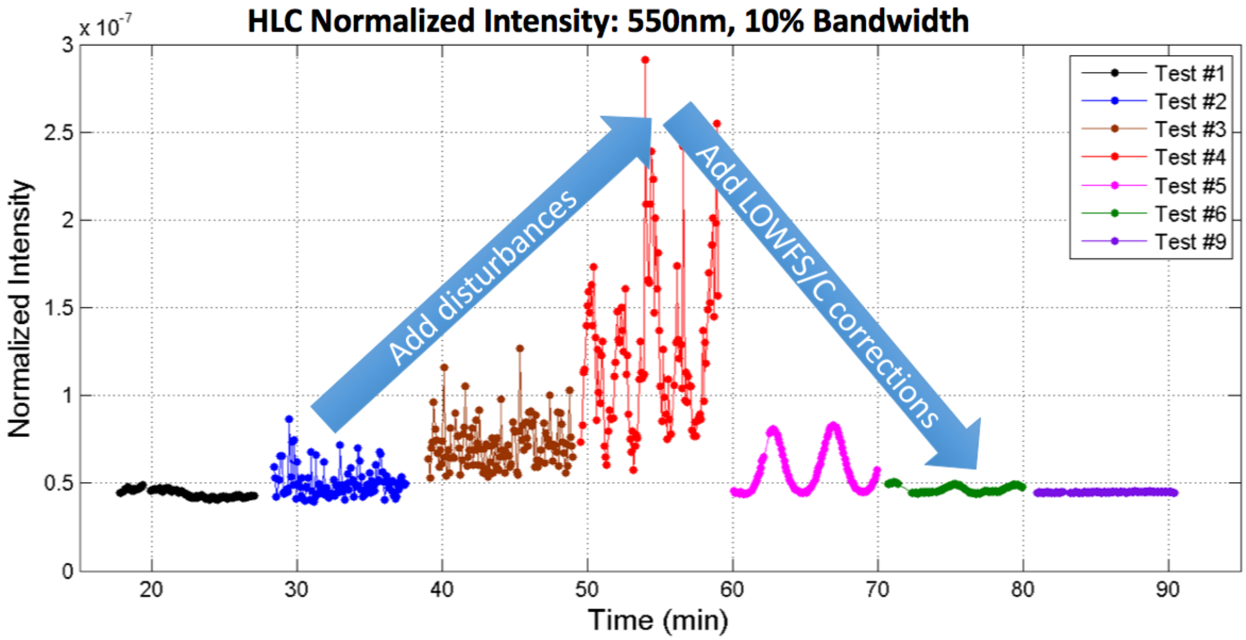

Figure 20: Preliminary data for WFIRST Milestone #9, the demonstration of high contrast in a dynamic environment. Tests 1 through 4 show the addition of dynamic disturbances, followed by turning on the low order wavefront sensing and control. (image credit: Fang Shi)

B.3.8 Mirror Coatings for Ultraviolet / Visible / Near Infrared (CG-10)

The measurement of broad atmospheric features in the ultraviolet band can enhance the direct detection and characterization of exoplanets. For example, at wavelengths shortward of 300 nm, the reflectivity of planets with O_3 in their atmosphere (such as in an Earth-like planet) is very low, while a different reflectivity cutoff shortward of 220 nm occurs for planets with SO_4-rich atmospheres (such as a Venus-like planet).[85] While a future space observatory (such as HabEx or LUVOIR) could be driven to a short wavelength cutoff less than 100 nm by general astrophysics science goals, wavelengths less than 200 nm are not likely to benefit exoplanet science directly. However, a space mission that requires both high throughput at wavelengths < 120 nm and wavefront uniformity for coronagraphy must develop appropriate mirror coatings. Coatings are needed to protect aluminum optics, which are reflective to light with λ < 120 nm , from oxidation. Non-uniformities in these coatings, which may also change with time, can induce wavefront errors at longer wavelength that a coronagraph system would have to correct. The ExEP is therefore interested in technology development in this area, particularly in the impact of coating uniformity on the performance of a telescope/coronagraph system.

The state-of-the art in space UV mirror coatings is HST and the Galaxy Evolution Explorer, which used aluminum optics coated with a thin layer of MgF_2. The reflectivity was > 85% for λ > 120 nm but dropped to 20% at shorter wavelengths. Hennessy et al (2016)[86] report 2 nm rms coating uniformity for multi-layer coatings on small samples but the uniformity over large primary mirror apertures is unknown.

While investigations into the uniformity of mirror coatings are not solicited as part of the TDEM component of the SAT call, a comprehensive systems-level study of an opto-mechanical structure and active control of wavefront errors would include them.

B.4 Ultra-Low Noise, Large-Format Detectors

The collected photon flux rate from exo-Earths, depending on telescope size and system throughput, is expected to be about one per several minutes. Consequently, the imaging detectors for both the detection and spectrometer channels of a coronagraph instrument must be highly sensitive, have ultra-low noise, and must be radiation hardened. In addition, the need for low spectral-crosstalk spectroscopy and large outer working angles to carry out disk science and imaging of the nearest exoplanets lead to the requirement for large format focal plane array—2k×2k pixels or larger.

Ongoing WFIRST investments are funding electron multiplying charge coupled device (EMCCD) development, though improvements in QE between 0.85 and 1 μm is desirable where there are important water spectral lines. Hence larger format and sensitivity in this spectral region is crucial for the implementation of a future exo-Earth imaging and spectroscopy missions. Proposals for the development of ultra-low noise, large-format near-infrared detectors and large-format ultraviolet detectors are solicited not under the TDEM element of the SAT 2016 call but rather under the TCOP element or the APRA 2016 solicitation, both through the PCOS/COR Programs. Proposers should contact the cognizant program officer to confirm the suitability of their investigation for those programs in advance of submitting a proposal.

B.4.1 Visible Detectors (CG-8)

The leading candidate detector technology in the visible is the silicon EMCCD detector, which can provide dark current noise of order 5×10^{-4} e-/px/sec while operating at 165 K after lifetime irradiation and clock induced charge (CIC) of order 3×10^{-3} e-/pix/frame. The effective read out noise can be < 1 e- rms using EM gain; the level of EM gain, or amplification, will depend on the native read out noise of the output amplifier that is being used. These detectors can operate in three modes: conventional CCD, EM gain with analog output, and EM gain with photon counting output.

The WFIRST coronagraph study has baselined the e2v CCD201-20 detector (1024×1024; 13 ×13 µm pixel pitch) for both of the coronagraph science cameras (imaging and IFS) and is carrying out full characterization and displacement damage dose (DDD) radiation testing. In 2015, this detector was characterized by WFIRST at the JPL Detector Lab using a NüVü EM N2 camera and found to meet the WFIRST beginning-of-life performance requirements (see **Figure 21**).

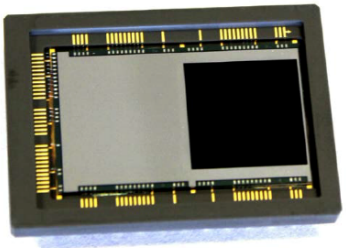

WFIRST Detector Performance Requirements

Specification	Goal	Requirement	Measurement	Unit
Effective read noise w/gain	0.2	0.2	<0.2	e^-
Dark current	1×10^{-4}	5×10^{-4}	1.01×10^{-4} *	e^-/pix/sec
Clock induced charge (CIC) @ 5.5σ threshold	0.0010	0.0018	0.0017	e^-/pix/fr

Figure 21: e2V CCD201-20 (1k×1k) detector and its characterization results conducted at the JPL CCD Detector Lab in 2015; data is beginning of life.

As part of the WFIRST coronagraph technology development program, the EMCCD 201-20 underwent a two phase DDD radiation test in 2015 simulating an L2 orbit of 6-year duration. In the first phase, a single radiation dose equivalent to six years at L2 was directed at two devices at ambient temperature to quickly assess the survivability of the EMCCD and to lay the ground work for an extended cryo-test. In Phase II, a single device was irradiated in four separate doses cumulatively simulating six years in an L2 orbit. The device was in the powered state and held at a fixed cryo temperature during the entire four-dose campaign. The cumulative six-year DDD equivalent dose was 7.5×10^9 protons/cm^2 assuming a specific camera shielding design. Radiation for test Phases I and II were conducted at the Scherrer Institute Beamline facility in Switzerland and Harwell Helios 3 Beamline in the U.K., respectively. In August 2016, the end-of-life characterization of the detector completed and showed a negligible increase of dark current to 7×10^{-4} e^-/pix/s, easily meeting the required $<10^{-3}$ e^-/pix/s. The read noise was unaffected and CIC degraded by an acceptable 10%. EM gain degraded by 25% due to device aging, not the radiation, and can be easily compensated with a change in drive voltage. The EMCCD detector thus shows robustness to the radiation environment at L2, met the WFIRST Milestone #7 requirements, and took an important step towards the needs of future exoplanet.

In 2014, e2V began development of the larger format 4k×4k EMCCD sponsored by a single customer.[87] At the time this Appendix was released, the company was still debugging the detectors and the larger device is unlikely to be considered for WFIRST. Given the current state of technology, a closely butted 2×2 mosaic of 1k×1k EMCCDs is far more mature than this larger format. The only drawbacks to the mosaic architecture are 1) the physical gap between the individual CCDs (they can be butted together but there is still a small gap) and 2) the extra mass of discrete electronics for each of the four CCDs.

Alternative photon-counting visible detector technology work was funded through a TDEM-09 award[88] (Donald Figer, Rochester Institute of Technology) looked at raising the technology readiness of silicon Geiger-mode Avalanche Photodiode arrays (480–1060 nm). A silicon 256×256 diode array was fabricated, hybridized to a CMOS readout integrated circuit, hybridized, and tested. This device has a 100% fill factor and a good response from 300–1000 nm. However, performance degradation after radiation testing led to only 3 of the 5 success criteria being met.

Microwave Kinetic Inductance Detectors (MKID) and Transition Edge Superconducting (TES) arrays are cryogenic alternatives capable of performing at visible wavelengths. Both are less mature than EMCCDs (more about these two promising detectors in Section B.4.2).

B.4.2 Near Infrared Detectors (CG-9)

Near infrared detectors with high sensitivity in the spectral region of 900 nm to 2.5 µm (and maybe greater) are critical for the spectral characterization of exoplanets and identification of possible biosignatures. Future exo-Earth missions (HabEx, LUVOIR) will consider infrared spectroscopy capabilities to detect hydrocarbons such as methane (1.00 µm, 1.69 µm, and 2.32 µm). The presence of methane in an oxygen-rich atmosphere like Earth's is one of the few known spectral combinations that point to a biotic origin with small probability of false positives.

Spectral characterization of exo-Earths in the infrared requires sub-electron read noise and the dark current noise < 0.001 e-/pix/s, in a space radiation environment over mission lifetime. These properties in a larger array, such as 2k×2k or 4k×4k, are desirable.

HgCdTe photodiode arrays hybridized to astronomy readout integrated circuits are the state of the art with a read noise < ~ 2 e- rms with multiple non-destructive reads, dark current of < 0.001 e-/s/pix. These detectors have flown in Earth orbit and have proven to be very radiation tolerant. Two large format 4k×4k pixel arrays offered by Teledyne Imaging Sensors, with 10 and 15 µm pixel pitch are at TRL 4 (H4RG-10™ and H4RG-15™).

Reducing the spurious count rate should be the top priority of non-cryogenic photon-counting detectors followed then by radiation hardening tests. Although conventional HgCdTe photodiode arrays may never function as photon-counting detectors due to leakage current at non-cryogenic temperatures, it is possible that today's H2RG and H4RG detectors are not yet approaching the fundamental physical noise limits of the photodiodes themselves.[89] Work distinguishing the contributions from the photodiode, interconnects, field-effect transistor, etc. would be valuable.

Other candidate detector technologies are currently less mature but worth watching. With appropriately optimized process, the HgCdTe avalanche photodiode (APD) array offers the possibility of the high gain and low effective read noise of EMCCDs while being capable of the same QE performance as the JWST arrays. Because gain is built into each pixel—unlike the EMCCD—they promise photon counting if the dark current is sufficiently suppressed.[90] The state-of-the-art Selex SAPHIRA arrays have reported ~10–20 e^-/pix/s dark current[91]. More work is needed to determine the actual noise floor and understanding the noise contributions from the HgCdTe photodiode versus the integrated readout circuit.

Cryogenic (superconducting) detectors such as microwave kinetic inductance detectors (MKIDs) have essentially no read noise or dark current solving the spurious count rate problem associated with the non-cryogenic devices.[92] These devices are scalable to large arrays. Transition edge sensor (TES) microcalorimeter arrays are also candidate cryogenic detectors with built-in energy resolution like the MKIDs. Both will require solutions for dynamic isolation, particularly from their cooler vibrations, and resolution (pixel count). The immediate challenge will be providing zero vibration cooling. While cooling is not a detector technology, future telescope architectures will want to mitigate all vibrations sources to enable the coronagraph performance to reach the dual driving instrument goals of 10^{-10} contrast ratios at <3 λ/D. Also, their radiation tolerance is unknown. NASA's PICTURE-C balloon experiment is baselined to include a 10–20 kpix MKIDs device in 2019. NASA-GSFC is considering maturing TES devices for future exoplanet imaging missions.[93]

The built-in energy resolution capabilities of the MKIDs and the TES devices are currently R ≤ 20, short of the R ≥ 70 desired by future biosignature-seeking spectrographs. Of course, these detectors could be positioned after the spectrograph.

Bernard Rauscher et al.[94] present a nice summary on the state-of-art and potential detector candidates for low-flux environments (see **Figure 22**):

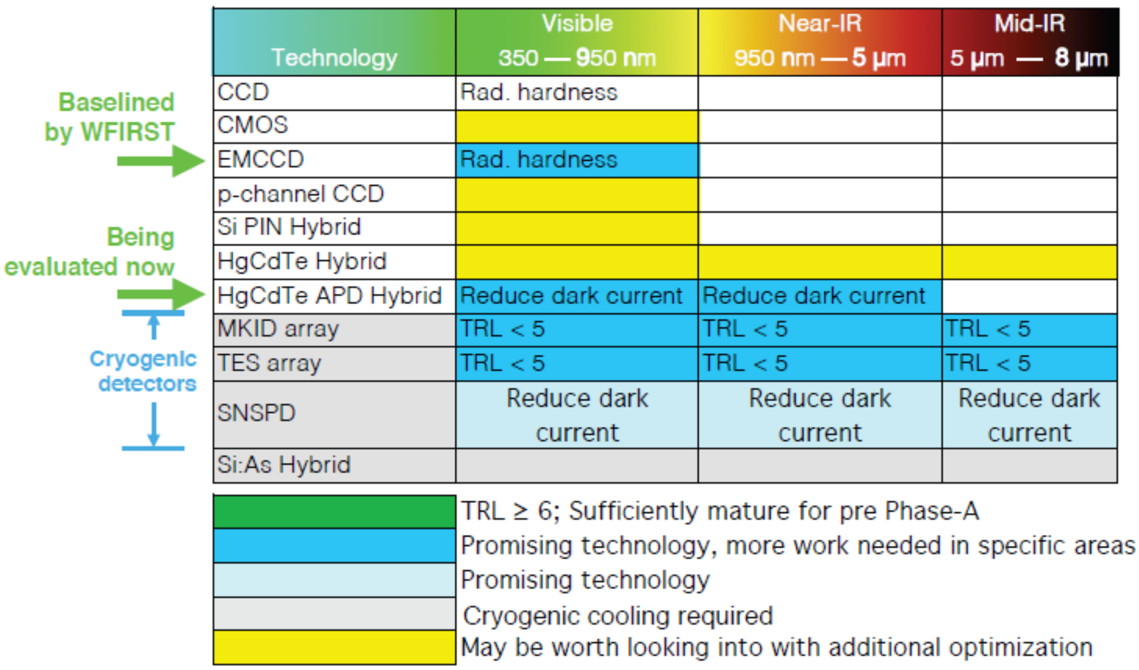

Figure 22: Summary of visible to mid-IR detectors for exoplanet science (Rauscher et. al. 2015).[95]

If future mission concepts do indeed require near-infrared spectral detections, then much work is needed in advancing the technology readiness of ultra-low noise infrared detectors.

B.4.3 Ultraviolet Detectors (CG-12)

The measurement of broad atmospheric features in the ultraviolet band can enhance the direct detection and characterization of exoplanets. For example, at wavelengths shortward of 300 nm, the reflectivity of planets with O_3 in their atmosphere (as in an Earth-like planet) is very low, while a different reflectivity cutoff shortward of 220 nm occurs for planets with SO_4- rich atmospheres (such as a Venus-like planet).[96]

The Habex and LUVOIR STDTs will determine the detailed requirements for UV detectors for exoplanet science applications during their ongoing studies; the needs listed in **Table 3** represent requirements linked to general astrophysics applications of UV detectors, and include desired sensitivity to wavelengths shorter than 100 nm.

We assume that wavelengths shorter than 200 nm are not likely to benefit exoplanet science directly. In the 200-400 nm band, there are several candidate technologies whose state-of-the-art is close to the needs for imaging spectral characterization of exoplanets, including EMCCD detectors and microchannel plates (MCP): see Bolcar et al. 2016[97] for a summary. Noise levels are adequate, but improvement is needed in quantum efficiency and detector lifetimes. Cryogenic MKID and TES detectors also operate in this band (Section B.4.2).

B.5 Data Post-Processing (CG-4)

The removal of quasi-static speckle noise from imagery data can further improve the final contrast and inner working angle capabilities achieved by coronagraphs. Post-processing activities can help reduce not just the overall performance of the coronagraph but also relax system-level requirements throughout the observatory. For example, counting on an order of magnitude improvement in the final contrast may loosen both wavefront control and telescope stability requirements. Some post-processing techniques require angular diversity by rolling the instrument (and spacecraft) azimuthally with respect to the star, or rely on observing a reference star. The specifics of the post-processing technique, however, levy operational requirements and calibration requirements on the spacecraft system and should be understood from the system level and early in the design process.

Applying state-of-art post-processing techniques onto image data already at 10^{-9}-level contrasts in the visible are unprecedented. This is a regime where amplitude wavefront errors may become as important as phase errors. In addition, most of the high contrast coronagraphic imaging post-processing algorithms and applications have been conducted in the near-infrared so far.

Remi Soummer et al.[98] applied ground-based techniques to HST NICMOS data and achieved signal-to-noise (SNR) improvements of 100 times for data with an initial contrast of 10^{-5} in the near-infrared. The use of similar techniques to improve contrast 10–100 times in the visible is under study via simulation in the WFIRST study. Initial results are promising with expected contrast improvement of 10×[99, 100] for initial contrasts of around 10^{-9} to 10^{-8}, depending on angular separation and actual post-processing method, as shown in **Figure 23**. However, it is important to note that such post-processing improvements are only obtained in the speckle noise-limited regime, i.e. when shot noise is negligible compared to speckle noise.

The WFIRST post-processing efforts will continue during the mission preparation and pave the way for future contrast gain studies. They will eventually provide fully optimized algorithms and even more realistic predictions of contrast gain as the coronagraph instrument gets assembled and closer to its final flight design conditions (spectral bandwidth, dynamical perturbations, etc.).

Since the advancement of algorithms for improved post-processing of coronagraph data is currently being addressed under the WFIRST technology development program, investigations in this area are not solicited under the TDEM element of the SAT 2016 call.

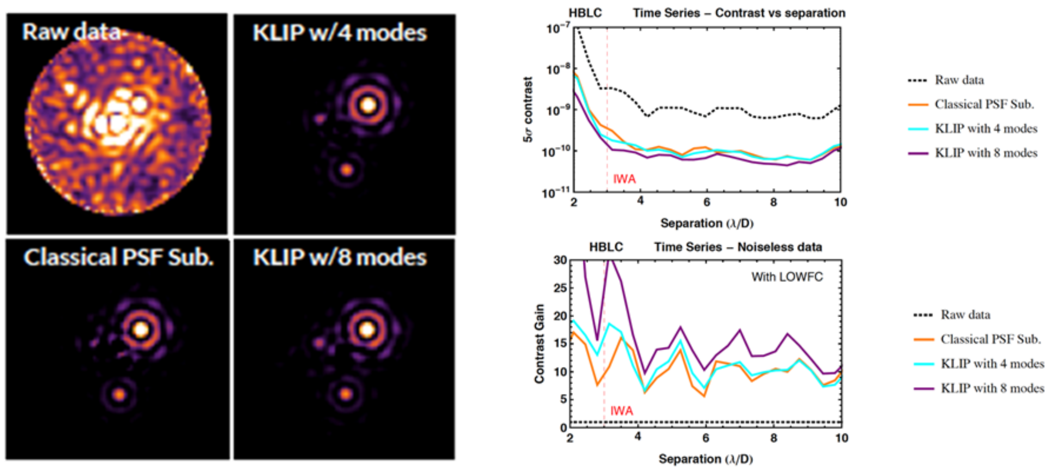

Figure 23: Post-processing improvements to simulated WFIRST HLC data. Realistic sequences of raw speckles fields are derived from full end-to-end simulations of a representative observing sequence. These include wavefront perturbations from expected thermal and structural disturbances.

B.6 Mid-Infrared Spectral Coronagraph (CG-11)

The ExEP has focused its coronagraph technology development on visible and near-infrared wavelengths because at a fixed telescope aperture size, the available inner working angle degrades linearly with wavelength. However, in the mid-infrared where a planet could be detected in thermal emission rather than in reflected starlight, the starlight suppression requirement is less stringent. The Origins Space Telescope (OST)[101] is another large mission concept study focused on far- and mid- infrared science, and formulating its mission in parallel with those of HabEX and LUVOIR. The OST's STDT noted a preliminary technology gap for coronagraph architecture suitable for mid-infrared direct imaging and spectral characterization of cool giant exoplanets. Achieving these science goals will require coronagraph technology with specific optimization for mid-infrared wavelengths.

The state-of-the-art in the mid-infrared are the four-quadrant phase masks on JWST-MIRI, which are predicted to achieve contrasts to 10^{-4} at 10.65 to 15.5 μm wavelengths with inner working angles of 0.33 - 0.49" in wide bands (i.e. no spectral dispersion).[102] To achieve its exoplanet imaging science goals, the OST STDT preliminarily estimates that it will need a coronagraph that achieves a contrast 10^{-6} with inner working angle (IWA) of 0.1" at 10 micron. The 0.1" IWA is needed to detect a 300 K Neptune-sized planet at 10 pc at a 1-2 AU separation, and the contrast requirement would detect a Saturn analog at 10 pc (~ 1 μJy at 24 μm, R~10, and 3 λ/D for a 16 m aperture). The maximum spectral dispersion must be sufficient to resolve the 15 μm CO_2 band, implying R ~ 500. The OST science case and reference design is still in development, and for now, ExEP prioritizes mid-infrared coronagraph technology relatively low compared to technology needed for visible and near-infrared wavelengths (Section F). Therefore, proposals for TDEM funding in this area are not solicited at this time.

C STARSHADE TECHNOLOGY NEEDS

External occulters, or starshades, block starlight by shadowing the entrance pupil of a telescope using a physical separation between the starshade and the telescope sufficient to provide the needed inner working angle. Depending on the size of the telescope and wavelength range, this typically requires the starshade to be tens of meters in diameter and located tens of thousands of kilometers from the telescope (**Figure** 24).

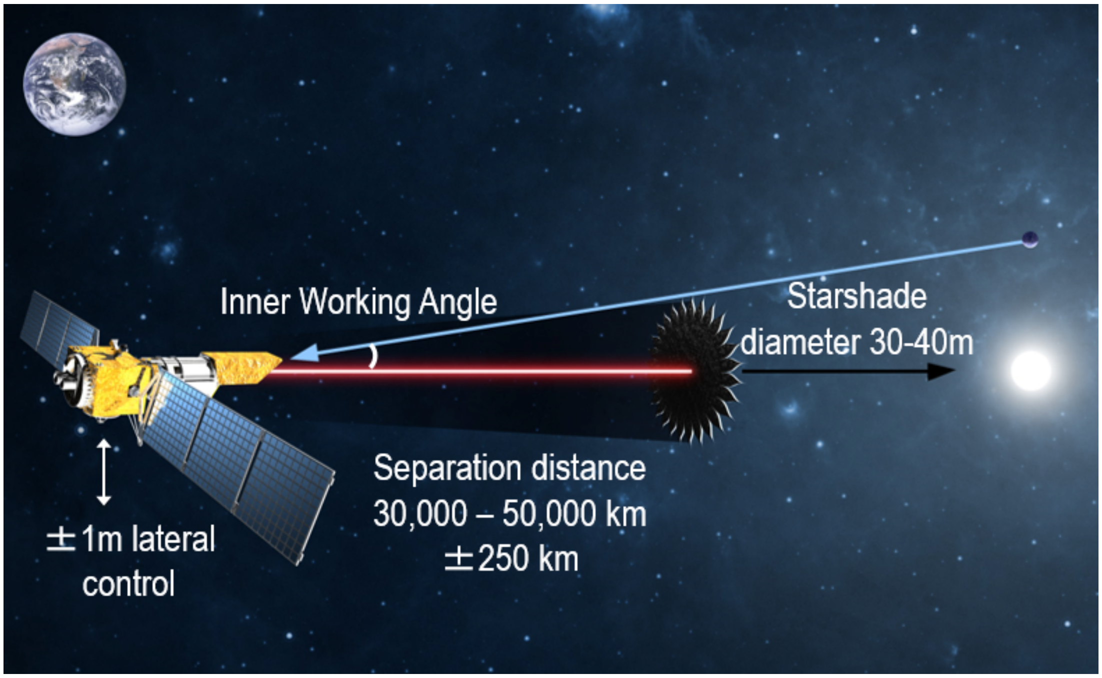

Figure 24: A typical starshade/telescope configuration. The starshade blocks starlight from reaching the telescope pupil, but allows light from the exoplanet.

A starshade suppresses on-axis starlight so that the reflected starlight from the off-axis planets can be imaged. It consists of an inner disk and flower-like petals shaped to create an apodization function to control diffracted starlight. It must also be opaque and limit the amount sunlight scattered from the petal edges into the telescope.

If a circular occulter were used rather than one with numerous petals, a Poisson spot would result in the telescope's focal plane ruining the ability to image faint exoplanets. Independent optical modeling predictions have shown excellent agreement concerning the contrast sensitivity to petal shape errors,[103] and detailed preliminary error budgets have been proposed.[104]

The five starshade technology gaps are listed in Table 4. They target starshades capable of flying on a probe-class mission, a possible Rendezvous mission to L2 with the WFIRST telescope, and/or possible LUVOIR/HabEx missions. The technology needs are largely based on an assumed WFIRST Rendezvous reference mission as detailed in the architecture of the NASA Exo-S probe study.[105] This study, sponsored by NASA's Astrophysics Division in 2014 demonstrated the valuable science return of a starshade mission with a 1.1-m telescope and the 2.4-m WFIRST telescope. The starshade needs of the LUVOIR and HabEx mission concepts have not yet been defined. In some cases, the needs listed in Table 4 will remain applicable, but in others, the requirements may change as the HabEx and LUVOIR STDTs further narrow advance their mission concepts.

The five technology gaps listed in Table 4 fall into three technology areas (as shown in **Figure 25**).

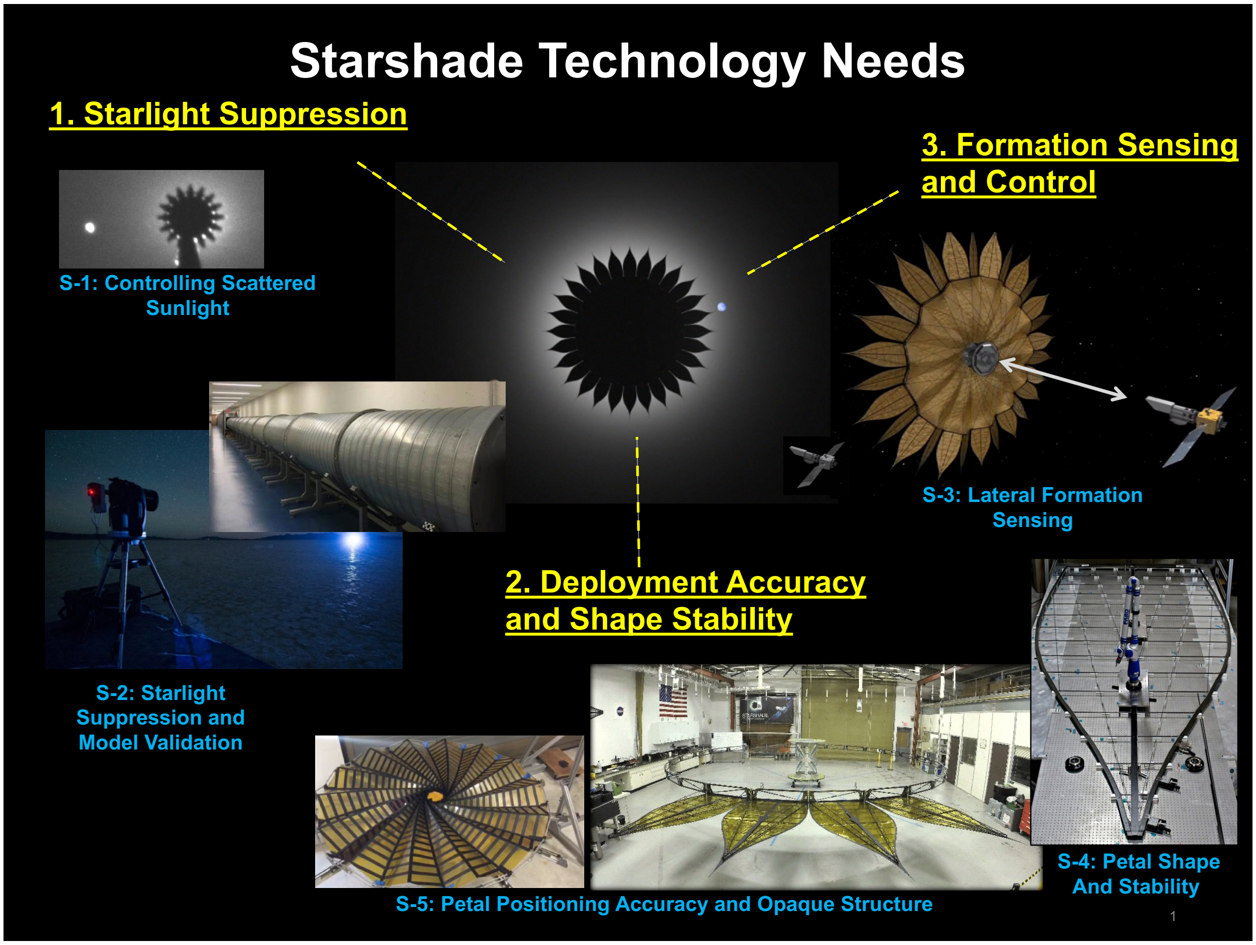

Figure 25: The three categories of starshade technology needs (in yellow font) to directly image and characterize exo-Earths around Sun-like stars.

1. **Starlight Suppression** – the ability to fabricate petals and their integrated optical edges to the design tolerances needed to create contrasts near the petal edges to better than 10^{-10} at the image plane. Fabricated petals that meet design requirements will minimize the diffraction from on-axis starlight and scatter/diffraction from off-axis Sun light detected at the science focal plane. The starlight suppression capabilities of the starshade must be demonstrated to validate optical models so that the models can predict performance in a space environment.
2. **Deployment Accuracy and Shape Stability** – the ability to stow, survive launch, and deploy the petals and inner disk to within the deployment tolerances budgeted to meet the shape, and ultimately, the contrast requirements. The optical shields within both the petals and the inner disk fully deploy intact with no damage.

3. **Formation Sensing and Control** – the ability to sense and control the lateral offset between the starshade and the telescope maintaining the desired contrast long enough for full science integration.

The criteria and rationale of the prioritization of the technology gaps can be found in Section A.3; the results of the prioritization can be found in Section F.

The published literature on starshades is inconsistent in defining starlight suppression, contrast, Fresnel number, and even the radius of the starshade (which can be defined in various ways due to the apodization function). Section C.3.1 of this document proposes clarification of these definitions, which we attempt to follow throughout this document wherever possible.

The SAT/TDEM program has succeeded in receiving proposals and funding all of the three key areas of starshade technology needs shown in **Figure 25**. The petal deployment technology gap (Section C.6) has remained unfunded by the TDEM program but has been the subject of several Small Business Innovation Research (SBIR) awards.

In 2016, NASA approved a directed starshade technology activity to be led by the ExEP to coordinate on-going and future development (see Section C.1 for further explanation). Consequently, the SAT/TDEM program will no longer accept starshade proposals.

Table 4: ExEP Starshade Technology Gap List. Gaps are listed in order of their prioritization scores according to the criteria in Section A.3. The priority column refers to Table 8. Please note discussion in Sect. C.3.1 of the definition of starlight suppression vs. contrast, and of the definition of Fresnel number at full apodization $F_{1.0}$.

Priority	ID	Title	Description	Current Capabilities	Needed Capabilities
1	S-2	**Starlight Suppression and Model Validation**	Experimentally validate at flight-like Fresnel numbers the equations that predict the contrasts achievable with a starshade.	Validated optical model with demonstrated 10^{-6} suppression at white light, 58 cm mask, and $F_{1.0}$ =210; 6×10^{-6} suppression demonstrated at $F_{1.0}$ =15; 1.3×10^{-7} suppression demonstrated at $F_{1.0}$ ~50	Experimentally validated models with total starlight suppression ≤ 10^{-8} in scaled flight-like geometry, with $F_{1.0}$ between 5 and 40 across a broadband optical bandpass. Validated models are traceable to 10^{-10} contrast system performance in space.
1	S-1	**Controlling Scattered Sunlight**	Limit edge-scattered sunlight and diffracted starlight with optical petal edges that also handle stowed bending strain.	Machined graphite edges meet all specs but edge radius (≥ 10 µm); etched metal edges meet all specs but in-plane shape tolerance (Exo-S design).	Integrated petal optical edges maintaining precision in-plane shape requirements after deployment trials and limit solar glint contributing < 10^{-10} contrast at petal edges.
1	S-3	**Lateral Formation Sensing**	Demonstrate lateral formation flying sensing accuracy consistent with keeping telescope in starshade's dark shadow.	Centroid star positions to ≤1/100th pixel with ample flux. Simulations have shown that sensing and GN&C is tractable, though sensing demonstration of lateral control has not yet been performed.	Demonstrate sensing lateral errors ≤ 0.20 m accuracy at scaled flight separations (± 1 mas bearing angle). Control algorithms demonstrated with scaled lateral control errors corresponding to ≤ 1m.

Priority	ID	Title	Description	Current Capabilities	Needed Capabilities
1	S-5	**Petal Positioning Accuracy and Opaque Structure**	Demonstrate that a starshade can be autonomously deployed to within its budgeted tolerances after exposure to relevant environments.	Petal deployment tolerance (≤ 1 mm) verified with low fidelity 12 m prototype and no optical shield; no environmental testing (Exo-S design).	Deployment tolerances demonstrated to ≤ 1 mm (in-plane envelope) with flight-like, minimum half-scale structure, simulated petals, opaque structure, and interfaces to launch restraint after exposure to relevant environments.
1	S-4	**Petal Shape and Stability**	Demonstrate a high-fidelity, flight-like starshade petal meets petal shape tolerances after exposure to relevant environments.	Manufacturing tolerance (≤100 μm) verified with low fidelity 6m prototype and no environmental tests. Petal deployment tests conducted but on prototype petals to demonstrate rib actuation; no shape measurements.	Deployment tolerances demonstrated to ≤ 100 μm (in-plane envelope) with flight-like, minimum half-scale petal fabricated and maintains shape after multiple deployments from stowed configuration.

C.1 Starshade Technology Development Activity

After five years of funding starshade through the competed SAT/TDEM program, in March of 2016 the NASA APD Director approved the formation of a focused starshade technology development activity. This approval allowed technology development for the starshade to transition from a competed, PI-led, SAT-funded effort to a directed, Program-managed, ExEP-funded activity. The activity's purpose is to reach TRL 5 for future starshade mission concepts that include WFIRST Rendezvous, HabEx, and LUVOIR starshades. It will be managed by the ExEP using NASA Procedural Requirements (NPR) 7120.8 as a management guideline. The authorization extends only through a first phase, akin to a planning or formulation phase. A formal review will be held before the activity can enter an implementation phase.

The key goals of the initial planning phase of the activity will include:

1. Defining an initial reference design
2. Evaluating alternative approaches and completing the key trade studies
3. Defining a Starshade TRL 5 Development Plan with key performance parameters and milestones
4. Planning the execution stage

C.2 Starshade Readiness Working Group

The starshade concept requires two highly aligned spacecrafts separated by distances too large to demonstrate to scale on the ground. To better understand the technology development roadmap to a potential starshade mission, NASA APD chartered in January 2016 the Starshade Readiness Working Group (SSWG). Bringing together subject matter experts from industry, academia, and NASA centers, the Working Group's objective was to determine if some form of a flight demonstration to mitigate technical risks would be required before NASA should agree to commence a starshade mission.

The SSWG's key findings and conclusions were:

1. A ground-only development strategy exists to enable a starshade science flight mission such as WFIRST Starshade Rendezvous and hence a prior flight technology demonstration is not required prior to a mission KDP-C.
2. Technology development for a Starshade Rendezvous mission is likely to provide significant technology benefits to both the HabEx and LUVOIR large mission studies.

The final SSWG briefing package can be found at *https://exoplanets.nasa.gov/exep/studies/sswg/*.

C.3 Starlight Suppression (S-2)

Starshades must demonstrate experimentally at a subscale level they can reach ≤ 10^{-10} contrast in a scaled flight-like geometry with Fresnel numbers ≤ 20 across a broadband optical bandpass. The challenge is that the large starshade-telescope separation distances required prohibit ground-based optical performance verifications of large starshades. Instead performance will need to be verified in a two-step process. First, subscale tests will demonstrate contrast performance consistent with imaging an exo-Earth and validate the optical models, upon which full-scale shape tolerances are based. The scaling approach is to match the flight design in terms of the number of Fresnel zones across the starshade such that the diffraction equations defining the dark shadow are identical. Second, the deployment accuracy and shape tolerances will be verified on a full-scale petal and deployment mechanism. Key capabilities have already been demonstrated via early prototypes, however, only a limited number of tests have been conducted at a flight-like Fresnel number (< 20).

Several experiments over the last decade demonstrate the viability of creating a dark shadow with a starshade to contrasts better than 10^{-10} just outside the petal edge. They include lab demonstrations at the University of Colorado,[106,107] Northrop-Grumman,[108,109] Princeton University,[110,111] larger scale tests in a dry lakebed by Northrop Grumman as part of their TDEM-12,[112] and larger scale demonstrations using the McMath Pierce solar observatory on astronomical objects. Each of these experiments has been limited in contrast performance to some extent by a subset of the following test environment issues:

- Wavefront errors due to collimating optics
- Dust in open air testing
- Diffraction effects due to the finite extent of the optical enclosure
- Diffraction off starshade support struts
- Imperfections in shade due to small dimensions
- Scattered light from imperfections in optics

The TDEM-12 activity led by Tiffany Glassman and Steve Warwick of NGAS was completed in 2015. It tested 58 cm starshades in open air on a dry lakebed with a starshade-telescope distance of 1 km and a "star"-starshade separation of 1 km (see **Figure 26**). The light source was a 1 W white-light LED.

The configuration parameters compared to flight are shown in

Table 5.

Figure 26: Optical demonstration setup in a Nevada dry lake bed. A 4-cm Celestron telescope is positioned 1 km from the 58-cm starshade prototype. A 1 W white light lamp simulating a distant star is positioned an additional km from the starshade. LEDs of various intensity simulating exoplanets are positioned near the lamp (photo: Northrop Grumman).

Table 5: Configuration parameters for Northrop Grumman's desert tests.

Test/ Obser vatory	Starshade to Telescope Separation (km)	Starshade Diameter tip to tip (m)	Starshade Radius r_e (m)	Telescope Diameter (m)	Resolution ($n\lambda/D_{SS}$)	Inner Working Angle to Tips (arcsec)	Fresnel Number (F_e)
1	0.5	0.58	0.24	0.04	16.0	61	210
2a	0.45	0.29	0.12	0.12	53.3	66	87
2b	0.45	0.20	0.08	0.08	23.7	46	42
2c	0.45	0.10	0.04	0.04	5.9	23	10
3	2.4	0.29	0.12	0.04	10	12.4	14
Space	~ 50,000	~ 40	16.5	2.4	1.6	0.1	< 20

Northrop Grumman was able to reach a contrast result of 9×10^{-10} near a petal edge (**Figure 27**).

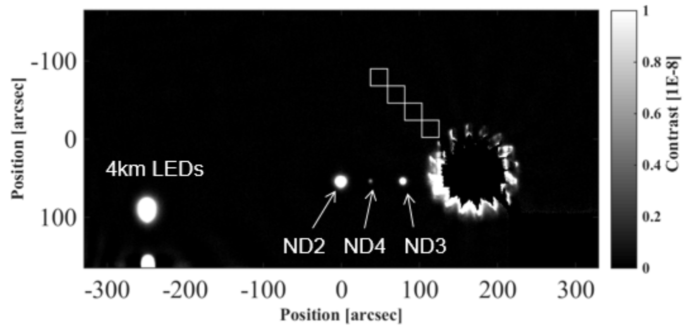

Figure 27: Combined 112 images; 3σ standard deviation in box closest to the starshade is 9.09×10^{-10}. Planet LEDs have neutral density (ND) filters in front; ND4 planet ~ 8×10^{-9} below main source. Light scatter from dust is modelled and subtracted from the image. (credit: Northrop Grumman)

During the TDEM-12 tests, intentionally flawed starshades were measured and compared to predicted results generated using Northrop Grumman, JPL, Princeton, and University of Colorado models. In CY16 the four groups were able to bring their model predictions to within a few percent of each other (**Figure 28**).

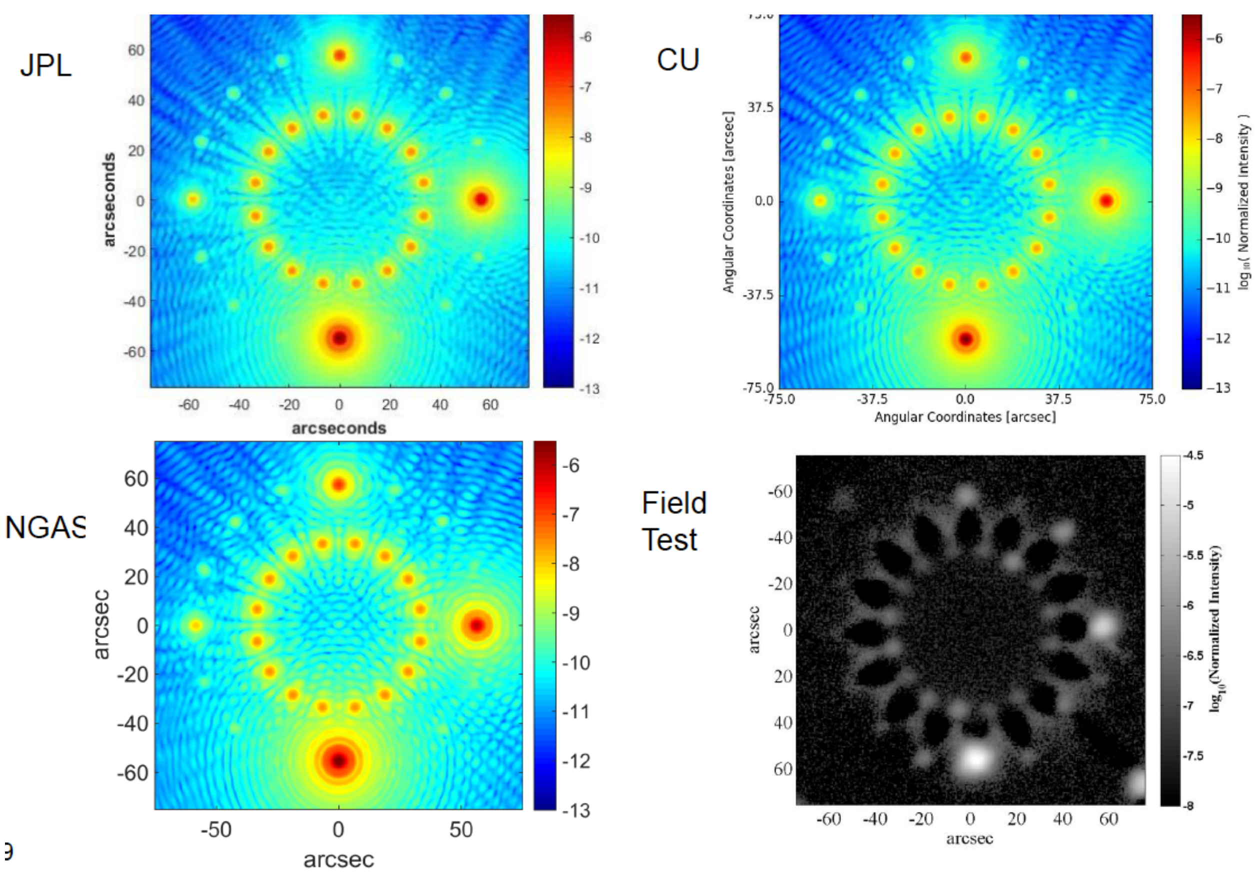

Figure 28: Figure Model Verification. Three independent models predicted the impact of intentional flaws on the optical performance of the starshade. Truncated-tip model results (top, bottom-left) and actual measurement

(bottom-right) are shown here, showing model agreement to a few percent and good reproduction of measurements.

Northrop Grumman and the University of Colorado have also carried out optical testing of the starshade at the McMath Pierce solar observatory outside of Tucson (**Figure 29** and **Figure 30**). This testing allows the starshade optics to be tested at close to the flight-like Fresnel numbers and uses parallel light from actual astronomical sources rather than the diverging source used in the desert. Use of a heliostat to track the position of the stars allows long integration times (~1 hr of stacked images).

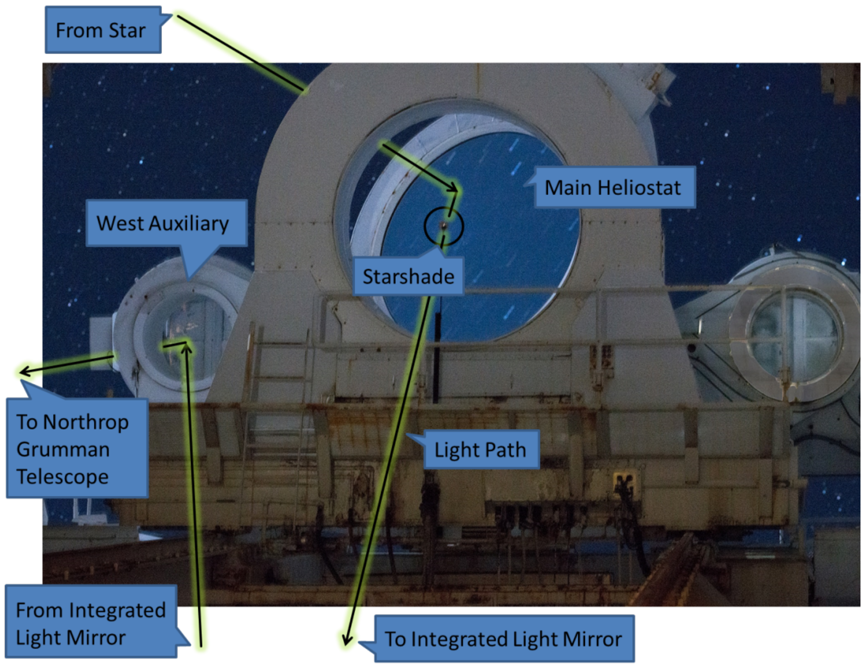

Figure 29: Light from a bright star or planet is reflected off the main heliostat and interacts with a small (~10 cm) starshade mounted directly after the heliostat. That light is shone off the integrated light mirror approximately 80 m down the McMath tube and back up onto the West Auxiliary heliostat (**Figure 30**) where it is directed over to a different collection site on the mountain. (credit: Northrop Grumman)

Figure 30: The Northrop Grumman collection telescope points at the west heliostat mirror approximately 250 m away collecting the light from the bright star and the starshade. The total optical separation of the starshade and collecting telescope is approximately 420 m. (credit: Northrop Grumman)

Demonstrations using this setup have been carried out against a number of astronomical objects (**Figure 31**) and sizes of starshades, covering Fresnel numbers ($F_{1.0}$) of ~ 90 to 10, as shown in

Table 5 for tests 2a-2c. A further collection site at 2.4 km has been tested (Test 3) and has been shown to be viable for future tests in 2016, allowing another step closer to flight like Fresnel numbers and inner working angles.

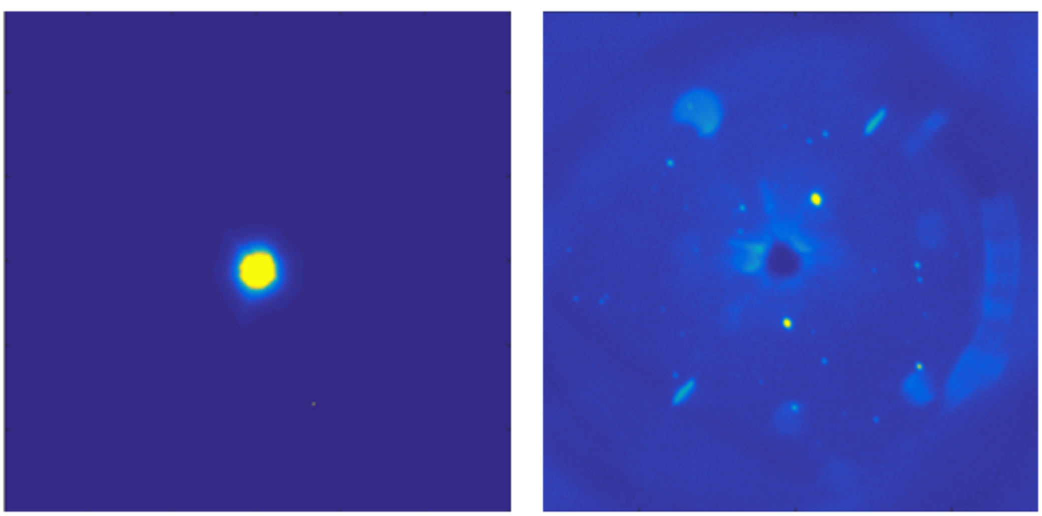

Figure 31: The 20 cm starshade (Test 2b) against the star Vega. A 1 sec exposure on the left is completely saturated. A 20 min exposure of Vega obscured by a starshade on the right allows much dimmer stars in the proximity of Vega to be seen. The two bright stars close to the center at ~10,000 times dimmer than Vega, with angular separation of ~2 arcmin. Dimmer stars in the image are approximately 10^{-6} of the brightness of Vega. All other optics are the same between the two images. (credit: Northrop Grumman)

An additional test at a flight-like Fresnel number (14.5) began in 2016.[113] A 77 m-long starshade optical testbed at Princeton University addresses a number of the limitations identified above (PI is Jeremy Kasdin, TDEM-12; see **Figure 32**).

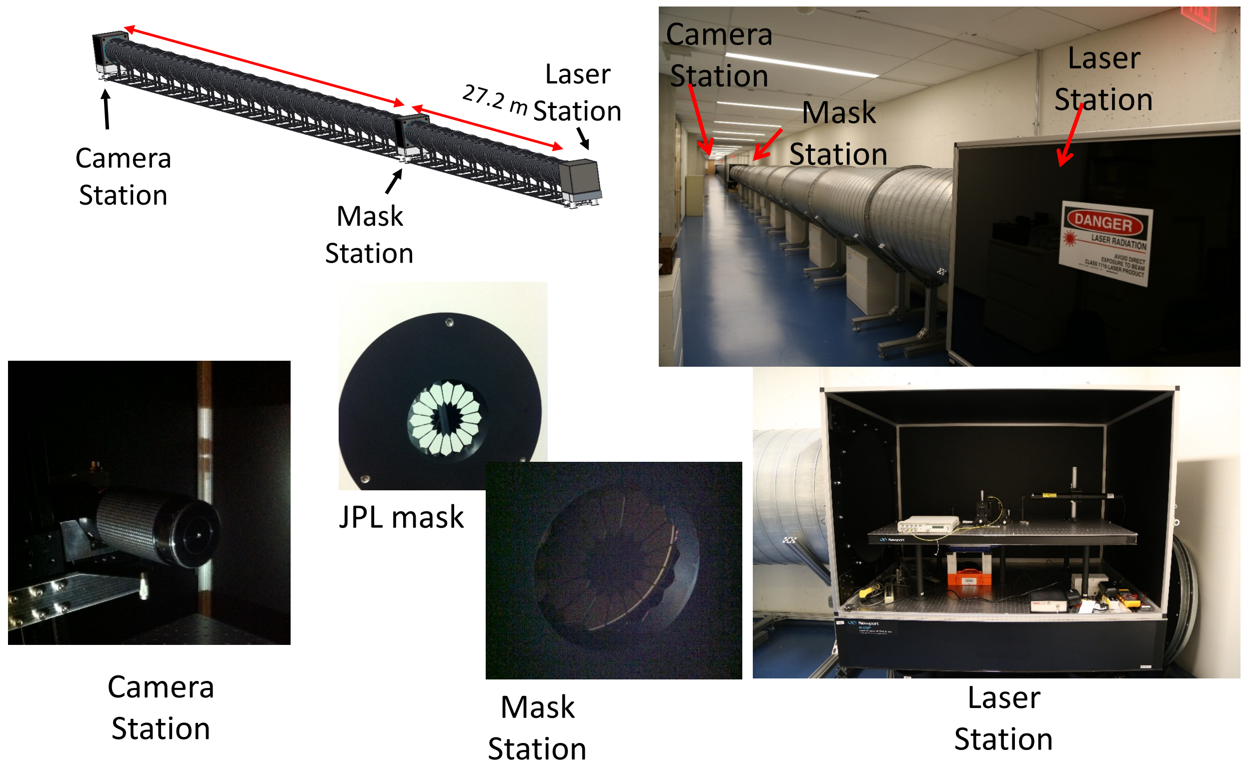

Figure 32: Schematic diagrams and pictures of the Princeton University starshade performance testbed (TDEM-12; PI Kasdin). Tubes are each 2 m in length and 1 m in diameter. They are painted with low reflectivity black paint and will include baffles to suppress stray light.

An expanding beam will be used to eliminate collimating optics and the testbed length is constrained to an available indoor facility with an optical enclosure that limits dust effects. Diffraction effects from the optical enclosure and support struts are mitigated with an innovative mounting scheme whereby the starshade is supported by an outer ring with an apodization profile optimized in similar fashion to the starshade profile (see Figure 33). This introduces a non-flight outer working angle limit at the tip of the outer ring. The demonstration is expected to match the flight Fresnel number (14.5) and first light of the testbed is expected in early CY16 and aims for 10^{-9} starlight suppression.

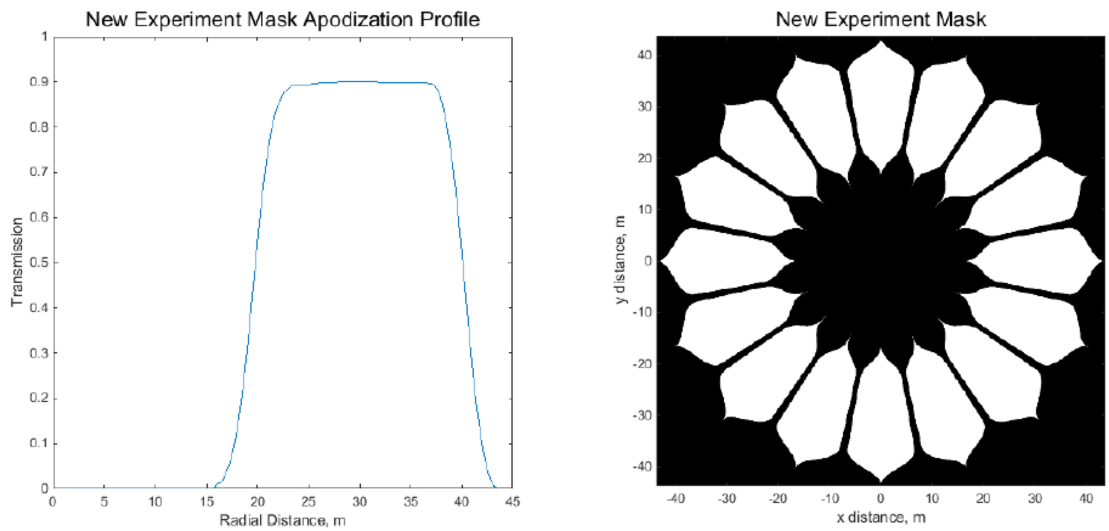

(a) (b)

Figure 33: (a) Kasdin TDEM-12 designed apodization profile including outer ring and struts. (b) Binary realization of mask profile.

JPL's Microdevices Laboratory, in support of Kasdin's TDEM-12, was able to reduce their starshade manufacturing resolution from 500 nm to 250 nm. This improvement is expected to reduce contributing contrast noise from the 26-mm-scaled shade. Significantly, the test results match well with analytical predictions for the shape resolution and defects. Testbed results, as of December 2016, are in process.

C.3.1 Contrast, Suppression, and Ground Measurements

Contrast and suppression have often been used interchangeably to describe the light-blocking ability of starshades. However, while related, these terms have different definitions, and in addition, several variants of each have been used. We use the following definitions here, and suggest they be adopted as standards:

Contrast ratio is the ratio of starlight irradiance in an arbitrary resolution element of the focal plane to the irradiance that would be seen in that same resolution element were the star to be centered there.

Suppression is the ratio of the total starlight that enters the telescope with the starshade in place to that without the starshade. It is measured in the pupil plane.

Contrast ratio is defined at a resolution element in the focal plane. It has meaning for both coronagraphs and starshades. It varies over the focal plane and is only meaningful when a location is specified. In practice, an average value over an annulus between an inner working angle and an outer working angle is sometimes given. Since a "resolution element" depends on the properties of the optical system, including the telescope, the contrast ratio is affected by the performance of the entire system, not just the starshade.

Suppression, on the other hand, depends only weakly on the telescope, and therefore is determined essentially by the starshade alone. Since it involves quantities integrated over the pupil plane, it is always a single number.

Because the telescope focuses the residual starlight onto the image plane, forming an image of the starshade, light leaking around starshade petals becomes concentrated into certain areas of the image plane, so that the contrast ratio (e.g., 10^{-10}) is always 'deeper' than the suppression (e.g., 10^{-9}). The relationship between them depends on the position of interest in the image plane, the telescope resolution and the number of pixels across which the starshade is imaged.

The fundamental diffractive property of the starshade depends on the Fresnel number, $F \equiv r^2/(\lambda Z)$, where r is the starshade radius, λ is the wavelength, and Z is the effective separation between the starshade and telescope. We note that the starshade radius can be defined at the tips ($r_{1.0}$), the 50% transmission point ($r_{0.5}$), the 1–1/*e* transmission point (r_e), or any other convenient point*, and likewise there are corresponding Fresnel numbers $F_{1.0}$, $F_{0.5}$, and F_e. We recommend that for clarity a subscript should always be included to indicate which definition is used. The starshade inner working angle can be smaller than the apparent angular extent of the starshade (IWA < $r_{1.0}/Z$), as is the case with a coronagraph, so it can be useful to reference different points along the starshade transmission function. In this document we use $r_{1.0}$ and $F_{1.0}$.

In space, the star is at essentially infinite distance, and Z is simply the starshade-to-telescope separation, Z_t. In laboratory testing, the source distance Z_s is often finite, and the parameter Z is given by $1/Z = 1/Z_s + 1/Z_t$. Typical Fresnel numbers in space are 8 – 15, with $Z \sim 40{,}000$ km and $r \sim 20$ m. Obviously, such large distances cannot be duplicated on Earth; a full-scale experiment can only be conducted in space. However, on Earth we can scale down r, λ, and Z to maintain the same F, e.g., $r = 2$ cm and $Z = 40$ m. The diffraction equations governing the two systems are identical, allowing for the laboratory measurements to demonstrate diffraction for the space case.

Several ground experiments have been carried out with large F, typically $50 < F < 500$. In some cases, this is done so that the measured effects are not washed out by atmospheric turbulence, and in others it is due to limited laboratory space. Two major issues arise. First, the nature of the shadow and the diffraction equation can vary from the space case, leading to potentially different sensitivities to misalignments and perturbations. Second, the starshade is typically well-resolved by the telescope, leading to localization of any shadow-perturbing defects into small image-plane resolution elements. High contrast is obtained in close proximity to the imaged perturbations. When the starshade is highly resolved by the telescope, a contrast of 10^{-10} could be obtained near the petal tips or between the petals while the suppression level is as large as 10^{-5}. In such cases, contrast measurements could lead to a false sense of success. In space, on the other hand, the telescope resolution is only a third or a fourth of the starshade diameter, and the contrast falls off much more slowly with angle, leading to a closer

* The starshade transmission function is slightly different from the amount of energy transmitted from an off-axis source to the telescope because of geometrical and diffraction considerations.

relationship between suppression and contrast ratio. Suppression measurements indicate that the performance of the starshade is largely independently of the telescope, but do not distinguish where the light appears in the image plane and how it affects planet detection. Furthermore, it can be challenging to measure the suppression of a test setup, and several ground-based experiments have measured contrast instead. Suppression is then estimated by integrating the measurable light over the image plane.

Figure 34 shows suppression vs. Fresnel number measured in several ground-based tests. A highly-resolved starshade with poor suppression would appear in the upper right corner. A brief description of each measurement is given below, in chronological order. We have included only published results. Other measurements underway or planned can be added as the results are published in the future.

CU-Leviton: Suppression was directly measured in the pupil plane photometrically. It was also measured at the focal plane of a camera (Leviton et al., Proc. SPIE 6687, 2007). After removing scatter known to originate at support wires as well as from the worst starshade defects, the measured suppression was $1.3 \times 10^{-7} \pm 1 \times 10^{-8}$. Fresnel values used are based on r_e rather than r_1. The range of Fresnel numbers is based on wavelengths at the half-power points of the convolution of the source spectrum, coupling optics spectral transmissions, and detector spectral response.

NG-Samuele: This experiment measured contrast of a starshade with r_1 = 23 mm suspended from three narrow wires. The light source was a collimated beam covering 450 – 800 nm. The distance between the starshade and telescope was 42.8 m (Samuele et al., SPIE 7731, 2010). Suppression is estimated by visually integrating the light in Samuele et al. Figure 10 and discounting the two spots known to be caused by the suspension wires. Samuele et al. reports that the two brightest speckles not related to wires have summed contrast of 1.2×10^{-6}. Visual inspection of the remaining speckles and halo leads to an estimated suppression of 2×10^{-6} – 1×10^{-5}.

Princeton-Cady: This experiment utilized an "outer" starshade in conjunction with the usual starshade to mitigate diffraction from the finite extent of the laboratory. Suppression was directly measured in the pupil plane with values of $1.7 \times 10^{-5} \pm 1.5 \times 10^{-6}$ at three wavelengths (520, 633, and 638 nm; Sirbu, Kasdin, and Vanderbei, SPIE 9143, 2014). In an earlier experiment using the same facility and nearly identical mask, Cady measured monochromatic suppression of 5.6×10^{-6} and broadband contrast (400–1000 nm) of 3.3×10^{-5} (Cady et al., Proc. SPIE 7731, 2010). The error bars are plotted to show the range of experimental suppression results. The Fresnel number range is based on the starshade parameters in Table 1 of Sirbu and the bandpass in Cady.

NG-Desert: A starshade with r_1 = 29 cm was placed between a light source and telescope separated by 2 km. The effective distance was Z = 500 m. The effective bandpass was 450–650 nm. Contrast was measured near the starshade tips to a level of $\sim 7 \times 10^{-10}$. The scatter in the image plane indicates that the starshade is working near its theoretical suppression limit of 1×10^{-6} within an estimated 50% uncertainty, based upon the accuracy of contrast measurements and model uncertainty. Detailed contrast results are given in Glassman et al., 2012 TDEM Report, NG Document #1469885 (2015).

NG-McMath: This experiment measured contrast that was calibrated to ~ 20%, based on published magnitudes of faint background stars in the field. A starshade with r_1 = 9.7 cm was placed in the beam reflected by the McMath solar telescope heliostat. The effective distance was Z = 450 m, and the bandpass was 450–650 nm (Novicki et al., SPIE 9904, 2016). The telescope and filters from the desert tests were used here as well. Suppression is roughly estimated by visually integrating the observed image plane halo to a flight-like resolution (roughly a factor of 100 lower resolution than in the McMath images), with error bars of $\pm$ 3 times the best estimate.

Flight: The gray area represents the region of parameter space we need to investigate if we are to successfully fly a full-scale starshade. All suggested flight starshade designs lie between Fresnel numbers of 5 and 40. There is little point in pushing total suppression below 10^{-9}, as Solar System Zodiacal Light alone is greater. Suppressions poorer than 10^{-8} can have a substantial and adverse effect on a flight mission, so effects that are significant at the 10^{-8} level need to be studied.

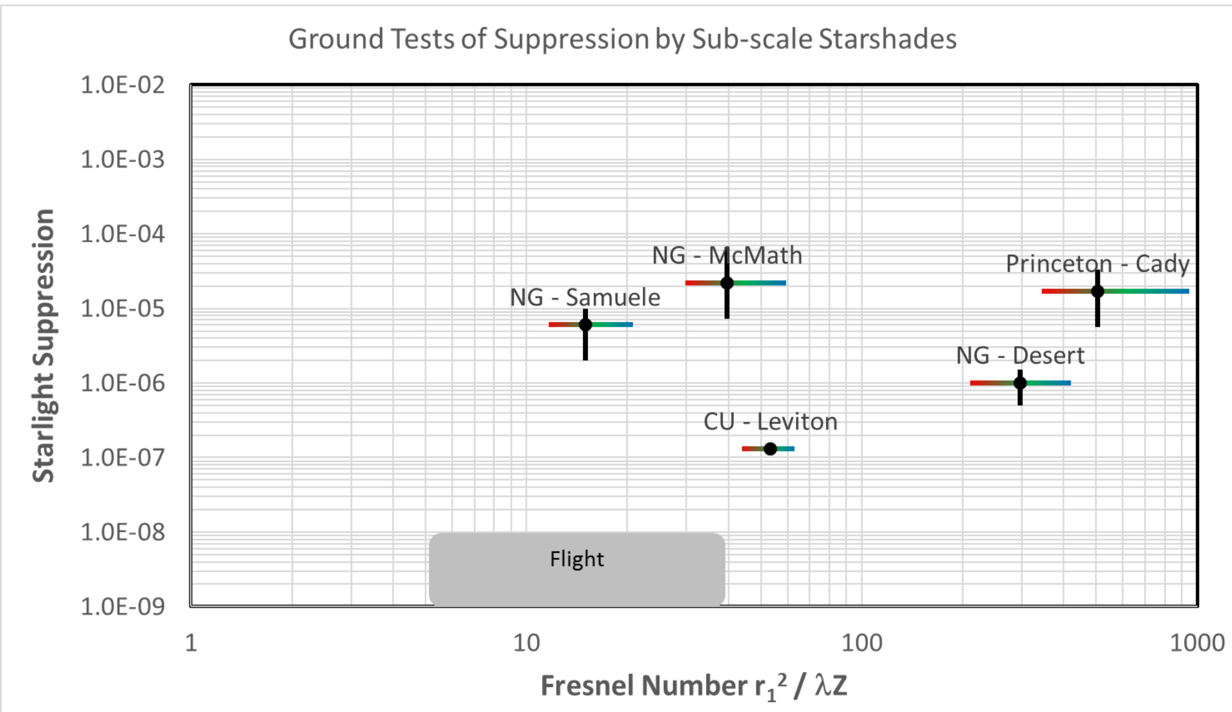

Figure 34: Light suppression versus Fresnel number for published starshade experiments. The grey box indicates the parameter space expected for a flight starshade.

Based on experience to date, achieving suppression levels in the flight range (10^{-8} – 10^{-9}) in ground tests will be a challenge, but improvements over past measurements can clearly be made. Measurements at flight-like Fresnel numbers could reach the grey area either by direct measurement of suppression near 10^{-9}, or alternatively by deep contrast measurements near 10^{-11} shown to be in good agreement with models. Either way, vigorous pursuit of such ground measurements is essential.

C.4 Controlling Scattered Sunlight (S-1)

The primary goal of the starshade optical edges is to provide the correct apodization function in order to suppress starlight to sufficient levels for exoplanet direct imaging. However, in order to do so light emanating from sources other than the target star must also be taken into consideration as this has the potential to significantly degrade the image contrast. Of greatest importance is the issue of light from our Sun scattering (reflecting) off the optical edges and entering the telescope. This solar glint appears primarily as two large lobes, spread by the telescope PSF, originating from a few petals oriented with edges broadside to the Sun. Methods to effectively eliminate this phenomenon such as spinning the starshade have been established, however the overall intensity of scattered light must be limited to levels below that from the exozodiacal background.

The required need is a solution that can be integrated to the petal's structural edge to (1) meet and maintain precision in-plane shape requirements after deployment and over a broad thermal environment, and (2) limit the intensity of solar glint such that a 10^{-10} contrast ratio can be established. Based on analyses for an Exo-S petal architecture[114] it was determined that the optical edges must maintain an in-plane profile to ≤ 20 µm rms to meet the shape requirement, and should have a sharp beveled edge with low reflectivity to meet the requirement on solar glint. This requires limiting the product of edge radius and reflectivity to less than 12 µm-%, while maintaining a stable in-plane shape, limiting thermal deformation of the petal and accommodating stowed bending strain.

In 2015, an effort funded by JPL internal research and technology development was established to produce prototype optical edges. These edges were constructed using thin strips of amorphous metal as the absence of material grain structure allows for extremely sharp edges to be produced. Chemical etching techniques were used to manufacture the edges as it provides a means to produce the necessary beveled edge and can be implemented at the meter-scale with micron-level in-plane tolerances. Multiple coupon level samples were constructed and their geometry characterized using SEM images. It was identified that a terminal radius of < 0.5 µm was achieved with low levels of variability across each coupon. The solar glint performance of these coupons was also established using a custom scattered-light testbed and measurements indicate that the scattered flux is predominantly dimmer than the predicted intensity of the background zodiacal light over a broad range of sun angles[115]. Further improvements to this performance can be achieved through the addition of low-reflectivity coatings on the optical edge, an area currently under consideration. While suitable performance specifications on solar glint were demonstrated at the coupon level, the in-plane shape requirements were not met on prototypes at the meter scale. This is attributed to a redistribution of internal stresses in the material during the etching process. Current efforts are focused on implementing a supported-etching technique to mechanically constrain the optical edge foil until it is ultimately attached to the petal structure.

Another effort within the ExEP starshade technology activity is dedicated to characterizing the sensitivity of edge scatter performance to edge defects and/or dust that can be attracted to statically charged optical edges. The dust environment in the launch vehicle fairing during launch will be evaluated and compared to the laboratory environment. One of the milestones is to verify solar glint performance at the petal level after testing to all relevant environments.

Northrop Grumman has implemented an alternative solution for the optical edges as their architecture for the starshade and its petals require looser optical edge requirements. Their method is to use traditional metal materials (titanium, beryllium copper, aluminum) which allows for standard manufacturing techniques to be implemented. However, as these methods do not produce sharp edges, they must incorporate low-reflectivity coatings. A thorough investigation into the viability of various coatings was performed in a 2015 TDEM[116] which included adhesion tests, thermal cycling, and humidity exposure. Acktar Magic Black™ on titanium edges was found to produce the lowest levels of scattered light intensity, with little change in performance observed after subjecting the coupons to environmental tests. Scattered light models of full-scale starshades were also developed, and efforts are currently underway to improve correlation between measurements and simulation results.
An entirely alternative approach to controlling solar glint is to manufacture a select set of petals with a high spatial frequency shape in order to eliminate the dominating scattered-light features associated with edges broadside to the Sun. JPL has constructed prototypes of these edges and have demonstrated that the technique is feasible. However, this approach has large system implications as it does not allow for the starshade to spin and is therefore under careful evaluation.

C.5 Lateral Formation Flying Sensing (S-3)

Maintaining precise alignment of the telescope, starshade, and target star is imperative to achieving the science goals of an exo-Earth-finding mission. The rapid decline in contrast as one moves radially from the center of the starshade's shadow places a tight constraint on the lateral position of the starshade relative to the telescope-star line of sight. According to mission studies for Exo-S,[117] New Worlds Observer,[118] and THEIA,[119] a starshade spacecraft must control its lateral position to within about ± 1 m of the telescope boresight to keep the telescope within the darkest shadow.

The benign disturbance environment at either Earth-Sun L2 or an Earth Drift-Away orbit makes controlling to the meter-level straightforward with conventional chemical thrusters: 10 cm-level control is regularly done in low Earth orbit for rendezvous and docking. The challenge, however, is to sense the lateral position error to within ± 30 cm at distances of tens of thousands of kilometers. While the control requirements of formation flying at L2 may not be beyond current capabilities, the accuracy of position sensing at such large separations is unprecedented (**Figure 35**). Closing this gap requires demonstrating the required sensing capability.

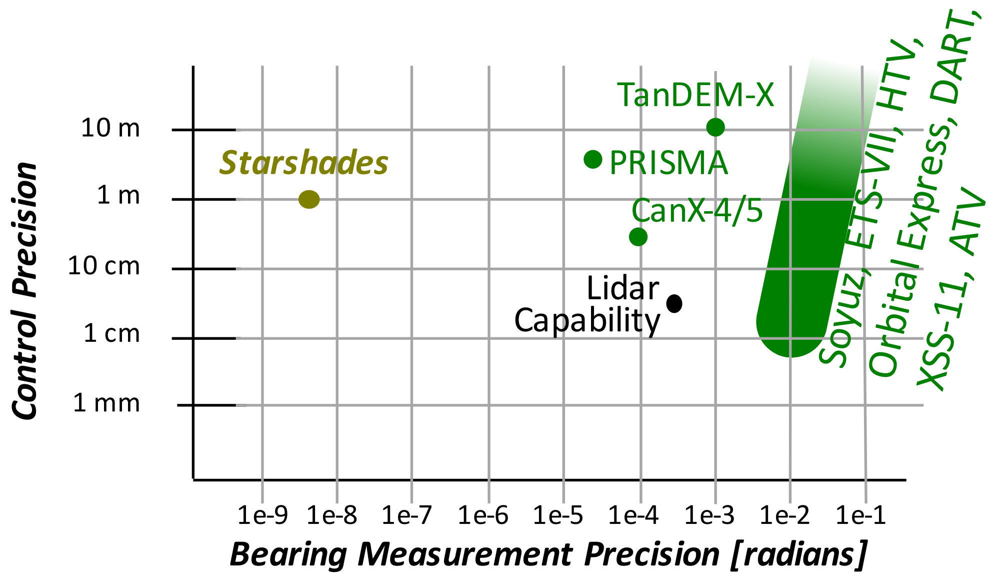

Figure 35: Precision of formation flying control versus precision of bearing angle. The ±1 m offset control between the starshade and the telescope is not unique to spacecraft. However, the bearing angle, due to the 30,000–50,000 km separations are unprecedented. More details can be found in the Exo-S report as well as Scharf et al. (2015).[120]

Comparatively, the axial separation distance, or range, between the starshade and telescope is loosely controlled to only within ±250 km,[121] with sensing knowledge to within ±1 km. The range is measured by a proximity radio with two-way ranging. These requirements are well within the state-of-the-art.

The WFIRST Project is investigating formation flying sensors as part of its starshade accommodation study. The goal of this study is to find starshade accommodation solutions that minimize the impact and additional risk to WFIRST. Therefore, retargeting the starshade between stars would be done with inertial navigation on the starshade using feedback from sensors on-board the WFIRST spacecraft. Results from this demonstration is expected in CY17.

With the creation of the managed starshade technology activity, no TDEM proposals in lateral formation sensing are sought in the 2016 SAT call.

C.6 Petal Positioning Accuracy and Opaque Structure (S-5)

To function as an occulter and to create a dark shadow for the formation-flying telescope, the starshade must (a) accurately deploy and maintain petal edges to their required in-plane position, and (b) deploy an optically opaque shade. Two distinct implementations are being considered for the packaging and deployment of a starshade. One example for the inner disk and petal deployment is the use of telescopic booms that radially expand to deploy the starshade's inner disk and petals (**Figure 36**, right). This architecture takes partial heritage from the JWST sunshield deployment (designed and built by Northrup Grumman) as well as non-NASA activities. The second approach is through the use of a radially deployable perimeter truss, from which attached concentrically-wrapped petals would unfurl (**Figure 36**, left). The architecture is inspired by Astro Aerospace's flight-heritage Thuraya radio-wave communications satellite, and most recently successfully flown with NASA's Soil Moisture Active Passive mission (Astro Aerospace is a subsidiary of Northrop Grumman). This is the architecture adopted by the NASA Exo-S mission concept study for 30–40 m-class starshades.

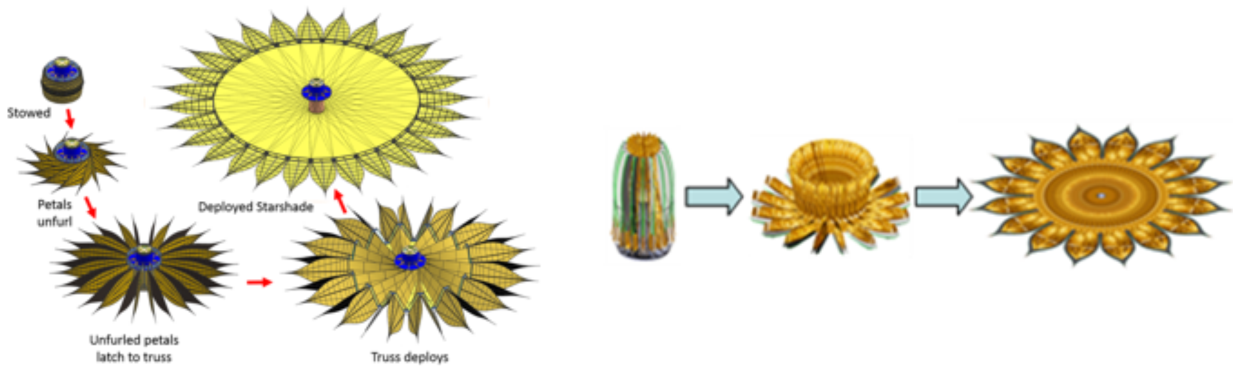

Figure 36: (Left) The Exo-S petal unfurling and inner disk deployment approach[122]; (Right) Northrop Grumman petal and inner disk deployment approach using simultaneous deployable telescopic booms[123].

Perimeter Truss/Petal Unfurling Deployment Approach

In 2013, a TDEM-10 activity[124] led by Jeremy Kasdin (Princeton) successfully demonstrated the deployment repeatability tolerances using an off-the-shelf retrofitted 12 m diameter Astromesh Antenna (Astro Aerospace), representative of the perimeter trusses architecture (Figure 37). This TDEM activity also produced a customized inner disk design tailored to accommodate starshade petals. In 2014, the ExEP advanced this concept by designing and building a 10 m diameter testbed to support future investigator demonstrations. Figure 38 shows this testbed fully deployed with four mockup petals. This effort was to demonstrate petal deployment accuracy only and not petal furling.

Figure 37: Kasdin TDEM-10 inner disk demonstration with an off-the-shelf 12 m diameter Astro-Aerospace antenna in the stowed configuration. This demonstration showed that the current Astromesh antenna design with specially attached petals could meet petal deployment and positioning requirements.

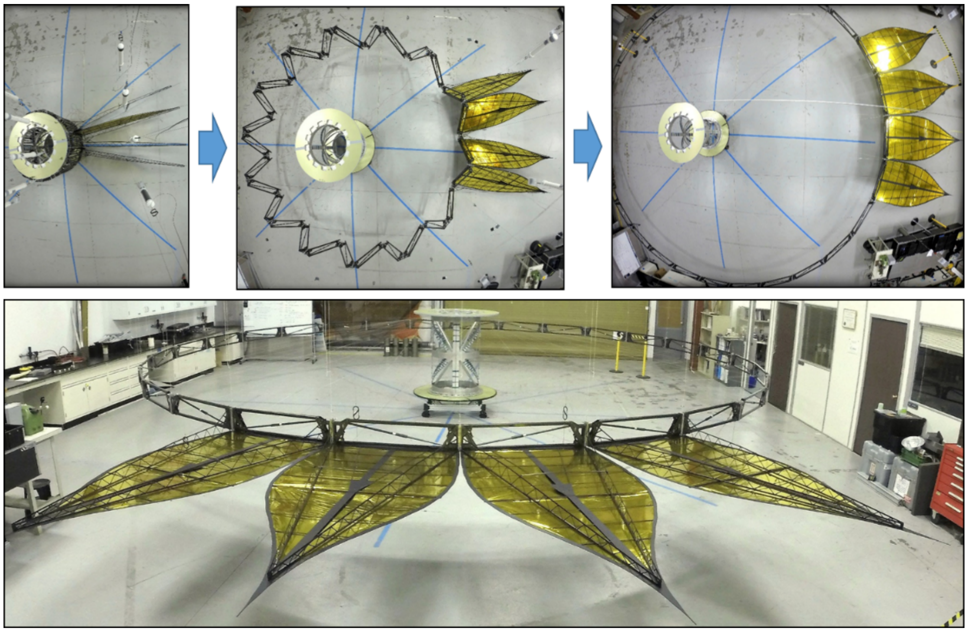

Figure 38: JPL-designed inner disk subsystem tailored to accommodate furling of the petals around the truss in the stowed configuration. This effort was supported by the Kasdin TDEM-10 effort and was built as testbed infrastructure for future principal investigator to investigate starshades solutions.

For the Exo-S architecture, a controlled petal deployment mechanism is required to secure petals throughout launch and ensure a deployment with no edge contact. The mechanical architecture stows the petals for launch in a very small volume by wrapping, or furling, them around a central hub. They deploy, or unfurl, by releasing the stored strain energy. The challenge is to control this energy release without petal optical edge to edge contact. There is no apparent state-of-art technology for this specific application.

In 2016, a full-scale petal deployment testbed was delivered to JPL by their SBIR partners ROCCOR and Tendeg (see Figure 39). Shown in the figure are the metallic simulated full-scale petal central spines wrapped around a simulated full-scale perimeter truss/spacecraft interface. Breadboard petal launch restraints were embedded in the petals and simulated the degrees of freedom required to restrain the petals for launch as well as simulate the challenge of furling the petals. This testbed will also serve to incorporate the culmination of the Tendeg effort to develop a higher fidelity petal unfurling mechanism. Near term efforts will include a breadboard unfurler mechanism that will unfurl the petal pairs synchronously. Additional features to be included are higher fidelity launch restraint mechanisms as well as features to control the tips of the petals during launch. This testbed serves as a stepping stone for Tendeg to design and deliver an unfurler testbed that include brassboard petals and high fidelity launch restraint interfaces and petal unfurler.

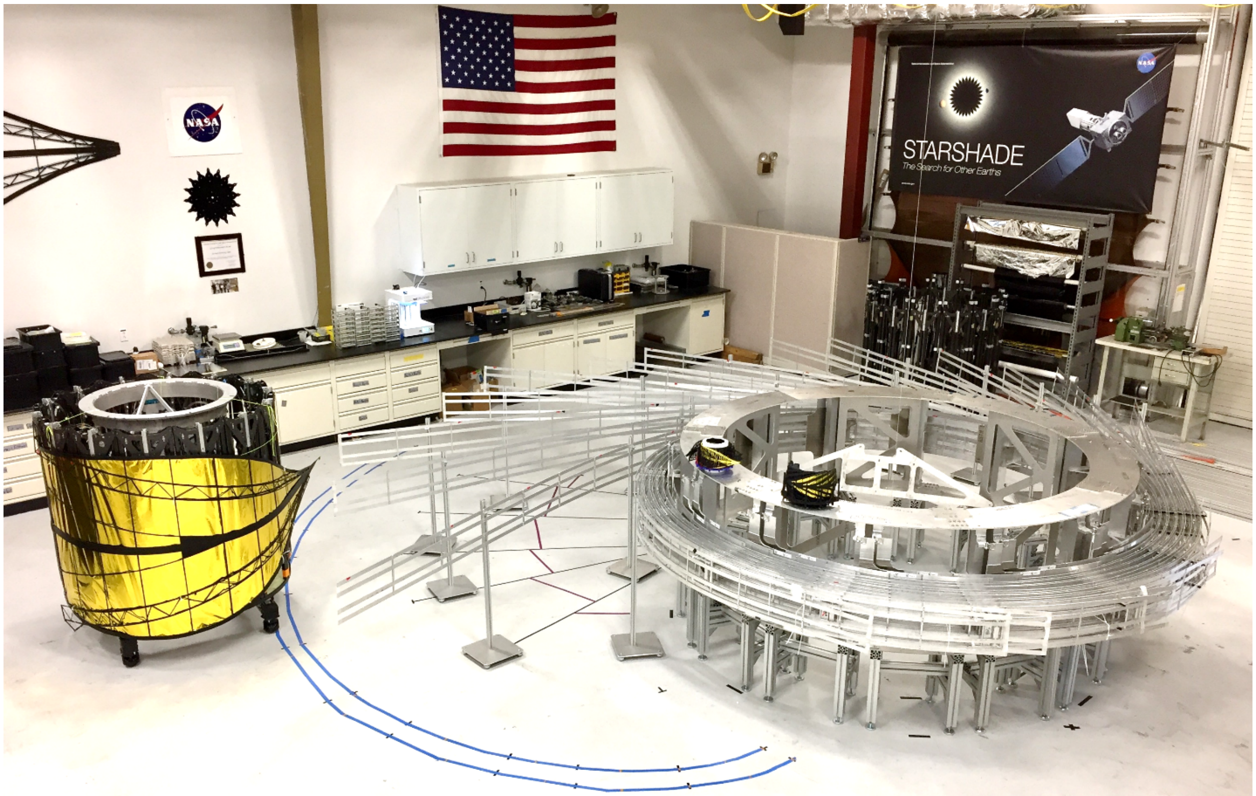

Figure 39: On the right is the Petal Launch restraint and Unfurling Subsystem testbed delivered to JPL by SBIR partners Roccor and Tendeg. Each of the long metallic spines represents a petal and simulates the same bending stiffness challenges as the single gold colored petal wrapped around the truss on the perimeter truss testbed on the left.

In 2016, a 5-m inner disk optical shield demonstration model was developed towards a TRL 5 half-scale Exo-S–based inner disk that built on the earlier origami fold pattern, considered to be ideal for stowage and deployment (**Figure 40**). Work is expected to continue in CY17 in developing the interfaces to the perimeter truss and experimenting with the inclusion of solar arrays as part of a potential solar electric propulsion application. JPL's Starshade Laboratory (Figure 41) is expected to play an important role in the continued technology maturation of the starshade on its path towards TRL 5.

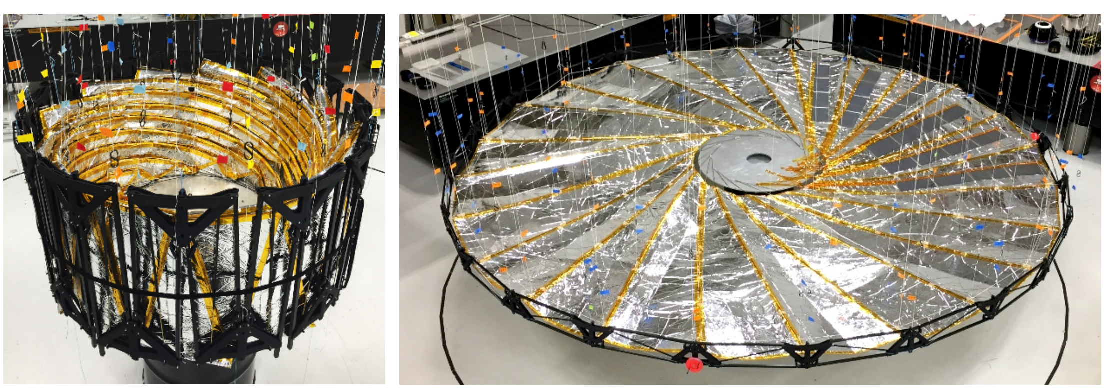

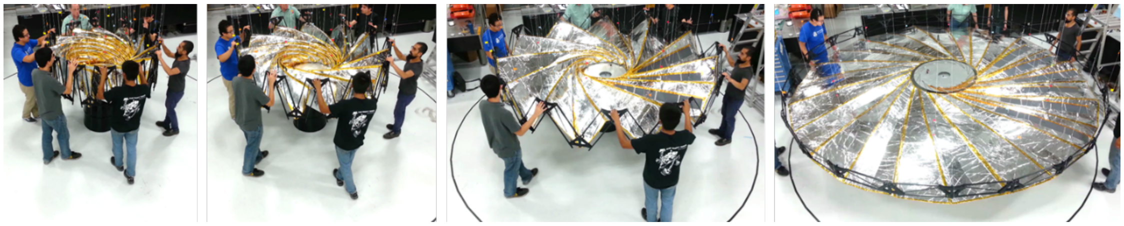

Figure 40: First deployments of 5-m flight-like optical shield with solar array segment. Material is two layers of Mylar sandwiching a thin layer of high-density polyurethane foam. The model also includes four gores of flexible solar panels as part of a possible solar electric propulsion option.

Figure 41: JPL Starshade Laboratory with multiple testbeds and demonstration units in use.

Telescoping Boom Deployment Approach

Northrop Grumman's deployment architecture, based in part on JWST sunshield heritage, and on non-NASA applications, relies on simultaneous telescopic booms to deploy both the rigid petal edges and inner membrane simultaneously—one boom per petal (**Figure 36**, right). This approach automatically deploys and positions the petals in a controlled manner with no risk of petal-to-petal contact. No demonstration, however, including petals or optical shield, has yet been developed. For completeness, and to provide comparison to the petal unfurling approach, we describe below its deployment architecture in more detail.

This deployment technique involves multiple actuations/deployments to transition from a stowed system that fits within launch vehicle volume requirements to the fully deployed operational system These deployments will require a high level of accuracy in order to meet the specified shape requirements of the starshade. The full deployment procedure is broken down into chronological steps:

Step one: release and deployment of launch lock support structure. The launch lock support structure will provide the necessary stiffness for the stowed petal structure to survive launch loads. Launch lock support arms provide this support and are constrained via a perimeter hoop restraint located approximately mid-height of the stowed system (Figure 43, left). Additional constraints at the support structure tips may be added to the launch lock system if additional stowed stiffness/frequency is required (or if support of the stowed petal system through the launch lock structure is needed).

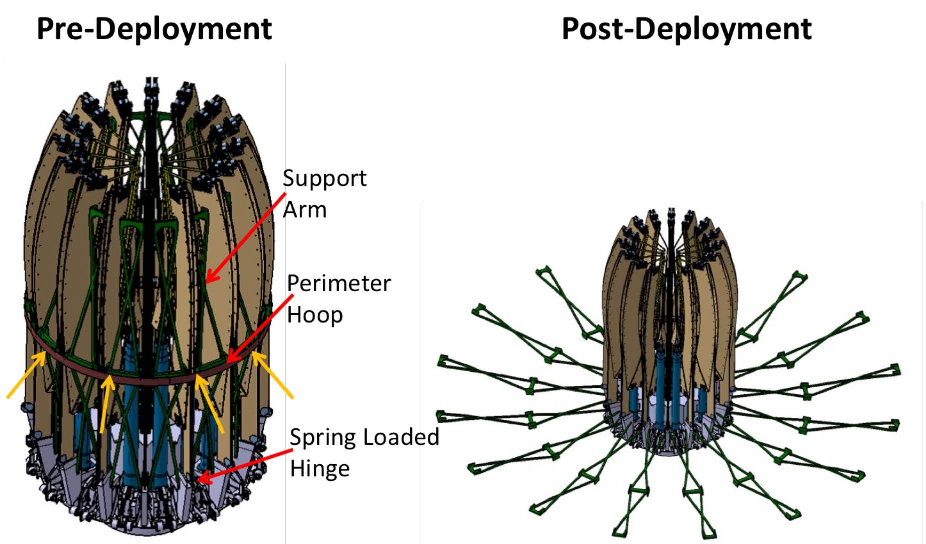

Figure 43: Launch lock mechanisms for the stowed starshade system. The perimeter hoop applies compressive force into the launch lock support arms. When the hoop is released, spring loaded hinges cause the support arms to deploy downward. This image shows a design with 16 support arms, but the hoop/support arm design could change in a future trade.

Release of the launch lock structure is triggered. The perimeter hoop restraint system releases all support structure arms in a near-simultaneous fashion. The deployment of the arms is accomplished by preloaded springs within a simple hinge at the root of the arms. Deployed preload from the springs is expected to be sufficient to hold the arms in the deployed position after release. Figure 43 shows the launch lock system in both its stowed (left) and its deployed (right) configuration. The concept presented uses a four-segment perimeter hoop and 16 support arms.

Step two: vertical driving of petals to clear base restraints. When stowed, the lower ends of the folded petals are seated in base restraints located on the main structure of the system (Figure 42, left). To clear the base restraints, the petals are driven upward to a sufficient deployment height so that the petals will clear the base restraints during the subsequent rotation of the boom systems (step 3 below). This deployment is shown in Figure 42.

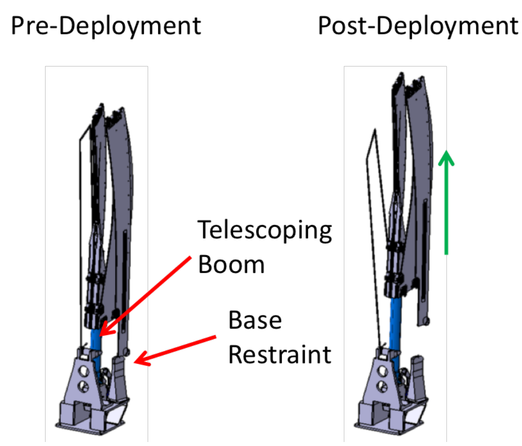

Figure 42: Images of a single boom before (left) and after (right) the STEM deployment required for the folded petal edges to clear the base restraints. A future trade may eliminate the need for this operation.

This vertical motion is achieved through the use of the Storable Tubular Extendible Member (STEM) systems. These STEM systems are drivers that are used in step four (see below) to fully extend the 16 telescoping booms.
Because each individual petal is tied to the next at the valley locations, all STEM systems must drive vertically simultaneously. Each STEM drive system has start/stop capability and contains rotary potentiometers tied to their output feeds, allowing a high degree of telemetry and control throughout the deployment cycle.
The vertical driving of the boom systems described here is required for the current design. A simple redesign may eliminate this step, and this will be included in a future design.

Step three: telescoping boom angular deployment (unfolding).

As in step two, near simultaneous deployment of all petals is a requirement to prevent excessive stress on the valley joints, and to prevent possible snags or tears of the membranes near the valley joints.
The booms are driven to their deployment angles via a central deployment tower, tied to each boom via linkages (Figure 45). The linkages are connected to a drive platform, which is driven up a worm gear by the drive motor. As the platform moves upward, the booms are deployed angularly downward. This design replaces previous concepts where this motion was controlled by an individual spring on each boom. The single motor option is much more controlled than the spring driven design. It also has a mechanical advantage, as the centralized tower system with deployment linkages allows back driving of the deployment

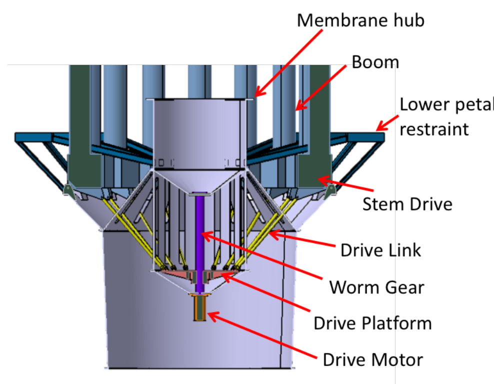

Figure 45: Details of the boom deployment mechanism. The 16 booms are driven simultaneously by a single drive motor, which drives a platform vertically up a worm gear. Linkages between the platform and the booms generate the desired angular deployment.

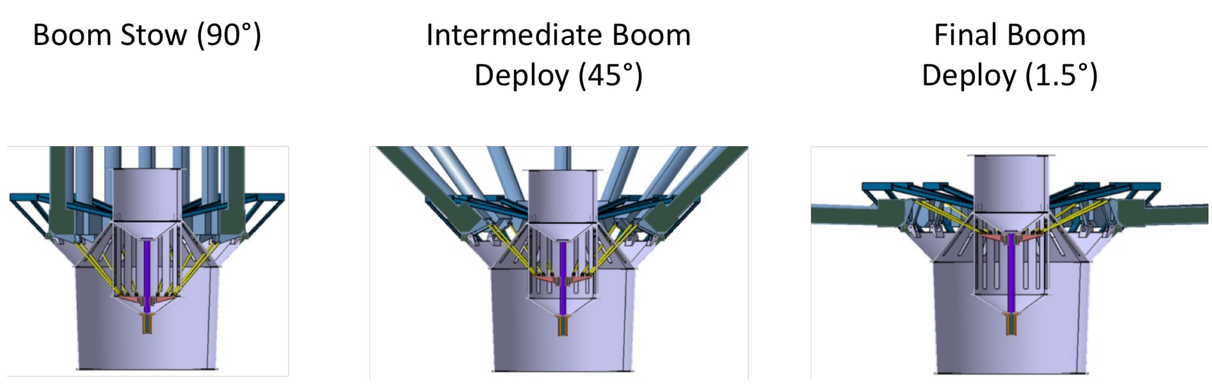

Figure 44: Snapshots of the angular boom deployment. Initially (left) the booms are in a vertical stow position. As the platform is driven up the worm gear, the booms move angularly downward until they reach the final deployed position, 1.5 degrees above horizontal (center, right).

if necessary, and holds steady at its final position, precluding the need for any positive latching of deploying boom/STEM elements. Snapshots of the angular deployment are provided in Figure 44.

S***tep four: STEM deployment (telescoping boom extension).***

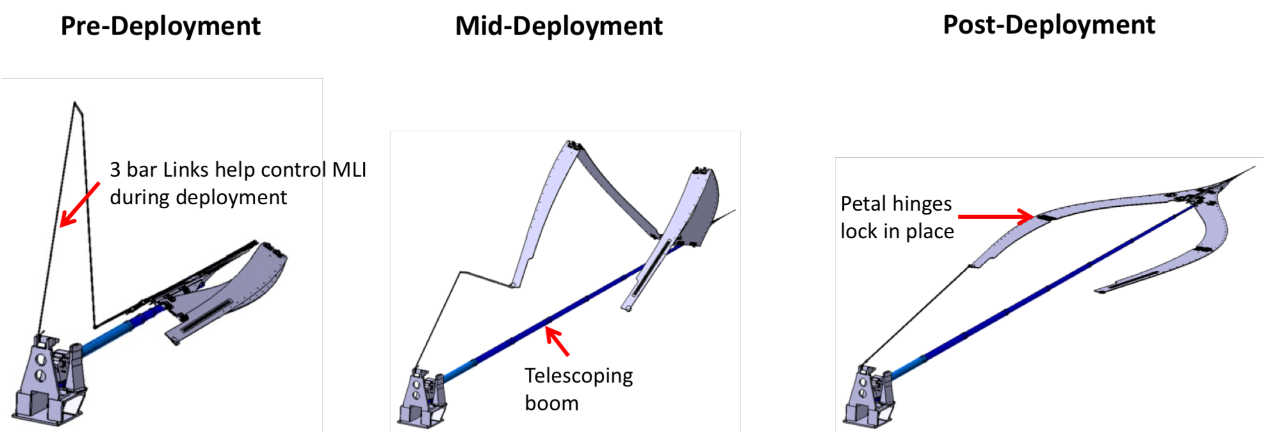

Figure 46: Snapshots of the STEM deployment for a single petal. As the telescoping boom extends, the petal outline unfolds. Once full extension is achieved, petal hinges lock in place in order to hold the desired shape

After the telescoping booms are driven to their final angle, the petals are fully extended by driving the STEM motors. Figure 46 illustrates this deployment step for a single petal. As the telescoping boom extends, the petal edge unfolds naturally, creating the required shape of the starshade outline. Once fully extended, the petal systems latch into place via clip/latching hinges.

Tension-links that run from the petal valley location to the central hub of the starshade are pulled out by the deploying booms in order to generate a positive tension within the starshade petal frame, as well as to control the MLI during deployment. The design trades for tying the tension links to the petals are still open, but one option is to use a constant force spring to connect the two. This spring would stroke over the last several inches of boom deployment and remain in that stroked/loaded position post deployment. Future trade studies will determine if more degrees of freedom at the petal valley need to be controlled.

JWST-heritage command and data handling (C&HD) motor control capabilities only allow for eight boom/STEM systems to be driven at once. As mentioned above, simultaneous deployment of all petals is desirable to minimize the risk of snag hazards and other detrimental shape warping effects. An incremental deployment that switches off between two sets of eight petals is an open option at this time, and is the current baseline. Future work will look at C&DH changes that will allow 16 systems to be driven at once.

Step five: tip wire deployment. The deployment of the tip wire is only required for Hypergaussian or near-Hypergaussian starshade shapes to complete the starshade shape. During step 4, the petal tips are folded back on themselves to protect them from damage and from damaging the membrane. Release of the tip wires is passive, actuated by either the full extension of the telescoping booms or the locking of the petal hinges (previous step). This

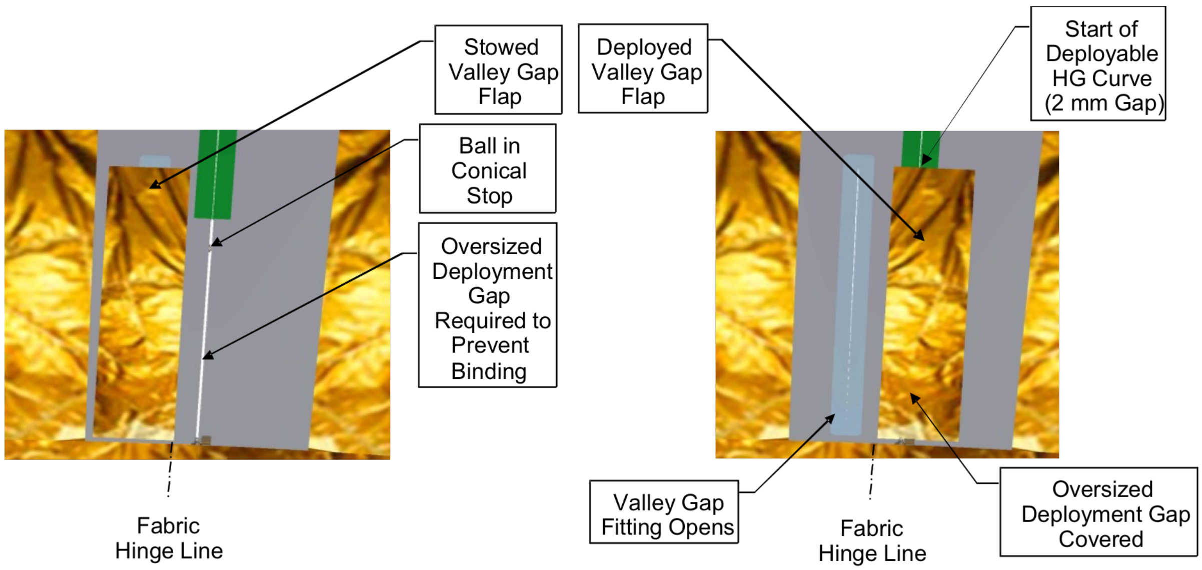

Figure 47: Images of the valley uncovering deployment for an HG starshade. The actual intersection between two adjacent petals is covered, replaced by an offset precision-made valley

option utilizes the capabilities/technology already in use on the JWST system. In that system, the shuttle at the tip of the last tube releases when the boom system is fully deployed.

The tip wires are deployed via a spring-loaded hinge that drives the tip wires into a hard stop. As the tips are spring driven to their final deployment positions, their motion must be damped in order to avoid damage to the tip wires upon impact with the hard stops.

Step six: Uncovering of Starshade Valleys. The Hypergaussian starshade shape also requires narrow valleys to complete the light-suppressing shape. Controlling the spacing between the two deploying petals to the required accuracy is difficult, so instead, the precise shape of the valleys is cut into one of the edge support pieces. Optically, offsetting the final part of the valley from the rest of the gap between two petals does not change the performance of the starshade. The optical valley is uncovered, and the mechanical valley is covered by the hinging of one piece of membrane material as shown in Figure 47.

Step seven: rotation of optics. The final required deployment is that of the formation flying optics. The laser/mirror system used as the beacon for lateral alignment sensing is stowed vertically within the vertically stowed booms for launch. On orbit, however, this system must be rotated 90 degrees downward in order to stay out of sunlight and avoid causing any glints (see Figure 48 below). This rotation is achieved with a motor that drives the hardware into a latch. The hardware will be rotated down toward a petal tip (rather than a valley) to ensure maximum shielding from sunlight.

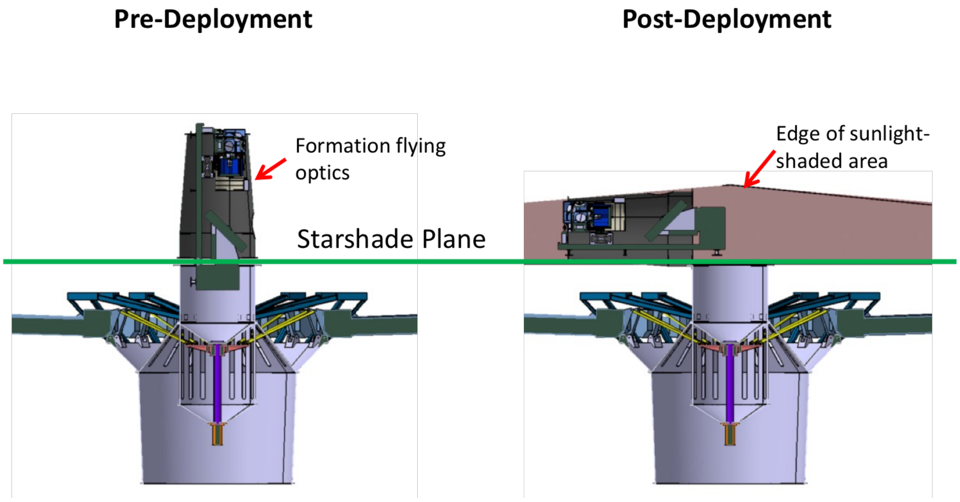

Figure 48: Deployment of the optics is a simple 90 degree rotation. The hardware is driven through the rotation by a motor, and is stopped by a latch. Once deployed the hardware will be shaded from the sun even in the worst case starshade-sun orientation, ensuring that glints will not contaminate data.

The optimal deployment approach for a starshade using a WFIRST Rendezvous design reference is currently an area of active study and the two approaches described here are intended to undergo a formal trade study and selection in CY17 by the ExEP starshade technology activity S5. The required size of starshades for larger, 4m-10 m-class telescopes is being studied but engineering designs have not yet been finalized nor whether they would be scalable from a WFIRST Rendezvous reference mission. This is likely to be a criterion in the deployment architecture trade study and will be included in the HabEx/LUVOIR mission concept studies.

C.6.1 Micrometeoroid Holes

Micrometeoroids will create holes in the starshade optical shield. Some will pass all the way through and others will not. The multiple spaced layers of an optical shield mitigate the impact of through holes, as only a small fraction will create a light path to the telescope. Preliminary modeling[125] of the starshade design and micrometeoroid flux environment indicates a cumulative through hole area less than 1 cm^2 that will add contrast of 10^{-12}.

The transmission of sunlight through micrometeoroid holes was modeled in 2015, showing that the open cell foam currently used to separate the optical shield layers is effective at dissipating sunlight. None the less, an additional layer of Kapton or Mylar is now planned as per the Exo-S architecture. More analysis will be required in this area as part of the starshade technology activity.

C.7 Petal Shape and Stability (S-4)

Starshade petals are responsible for controlling the diffraction pattern of the on-axis starlight so that it interferes destructively in a cylindrical region behind the starshade where an aligned telescope could follow. The petals also are required to mitigate reflection and diffraction of light from the off-axis Sun. Consequently, they must be fabricated to a precise shape to achieve all of these optical goals. A flight-like, full-scale petal (~ 6 - 8 m) must be fabricated to within 200 µm of shape tolerances and to maintain shape after multiple deployment cycles from stowed configuration as well as demonstrate required tolerances in a relevant environment.

Two similar approaches to the design of external occulters have been studied, differing by whether an analytical petal shape is used[126, 127] or whether it derives from a mathematical optimization.[128, 129] The TDEM-09 activity led by Jeremy Kasdin of Princeton adopted the latter approach and successfully demonstrated the allocated manufacturing tolerance (≤ 100 µm) of an early 6-m petal prototype, which did not include optical shields that make the petal opaque, optical edges that effectively scattered and diffracted sunlight, or environmental testing (**Figure 49**).

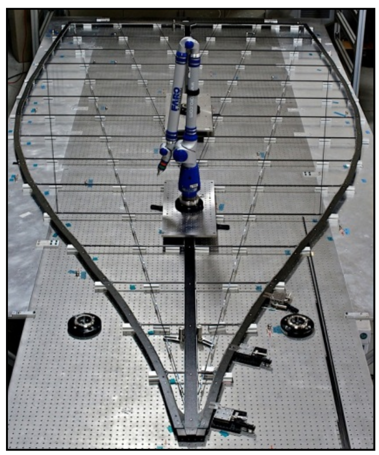

Figure 49: TDEM-09 6-m prototype petal designed and fabricated to meet 100 µm design tolerances (PI Kasdin/Princeton with his JPL Co-Is).

In 2015, a TDEM-12 activity led by Kasdin developed a new preliminary petal design that incorporates flight-like optical edges and optical shields and includes interfaces to proposed launch restraint and petal deployment control mechanisms. Ongoing activities will complete the detailed petal design, produce a flight-like, full-scale prototype and test it in relevant environments. The final verification will be to verify petal shape multiple times with deployment testing in between. This will require an in-situ petal metrology tool.

D OTHER TECHNOLOGY NEEDS

A single enhancing technology gap falls outside the typical coronagraph and starshade categories - Extreme Precision Ground-based Radial Velocity.

Table 6: ExEP Indirect Detection and Characterization Technology Gap List. The priority column refers to Table 8.

Priority	ID	Title	Description	Current Capabilities	Needed Capabilities
5	M-1	**Extreme Precision Ground-based Radial Velocity**	Ground-based radial velocity instrumentation capable of measuring the mass of candidate exo-Earths in the habitable zone and to maximize efficiency of space telescope surveys.	Single measurement precision: 80 cm/s HARPS instrument; NN-EXPLORE's NEID (WYNN observatory) in development: goal 27 cm/s	Signal from exo-Earths is 10 cm/s; Need to reduce systematic errors to 1 cm/s on multi-year timescales; statistical uncertainties of 1 cm/s on monthly timescales for late F, G, and early K stars

D.1 Extreme Precision Ground-based Radial Velocity (M-1)

Ground-based radial velocity (RV) measurements provide two important enhancements to a space mission's ability to direct-image and characterize exoplanets. First, by pre-selecting stars for coronagraph or starshade observations, science yield is increased since the widest projected exoplanet separations would be known a priori. Second, precision RV measurements determine the minimum mass, necessary for determining potential habitability.[130,131] The state-of-the art single measurement precision is currently 80 cm/s[132] , expected to be advanced to 20-30 cm/s by NN-EXPLORE's NEID instrument[133] for the WIYN telescope, and the iLocator[134] instrument for the LBT, both planned for first light in 2018. To discover Earth-mass planets orbiting Sun-like stars, a precision of 1 cm/s over the relevant orbital time scales is needed.[135] Achieving this goal requires investment in theoretical studies of stellar stability, as well as in instrumentation, including wavelength calibration and in the stability of spectrograph pressure, temperature and optical-mechanical structure on one-year time scales.

Despite the important benefits offered by precision RV technology, its enhancing nature (rather than mission-enabling) resulted in it being ranked lower than the starlight suppression needs for the ExEP. Hence, proposals for TDEM-16 funding for precision RV technology development studies are not requested at this time.

E TECHNOLOGY WATCH LIST

Four of the technology gaps submitted by the community, while not meeting the selection criteria to be included on the prioritized technology gap list, were determined to be potentially beneficial to exoplanet missions. These gaps will be revisited annually for possible prioritization and are listed in Table 7. Proposals to advance these technologies are not solicited in the TDEM component of the 2016 SAT call.

Table 7: ExEP Technology Watch List.

Gap Title
Advanced Cryocoolers
Sub-Kelvin Coolers
Mid-IR Ultra-low Noise Detectors
Astrometry

E.1 Advanced Cryocoolers

Some classes of energy-resolving near-infrared and visible detectors for exoplanet characterization (such as KIDs and TES microcalorimeters; see Section B.4.2) require cooling to temperatures < 1 K. To reach these temperatures, sub-kelvin coolers must be pre-cooled by an advanced cryocooler. Below 25 K, passive cooling in space is not practical and compact cryocoolers are necessary for pre-cooling a sub-Kelvin cooler. Custom solutions have been successful in space for mm-wave space missions such as Planck, but additional work is required in heat lift, lower mass, lower volume, and lifetime. Sorption coolers and mechanical Joule-Thomson, pulse tube, and Stirling coolers are possible solutions, but vibration isolation must be at a level compatible with the sub-nanometer wavefront stability needed for coronagraphy. See Rauscher et al (2016)[136] for a discussion of technology suitable for cryogenic detectors.

E.2 Sub-Kelvin Coolers

To cool an energy-resolving exoplanet detector system below 1 K starting from a stage pre-cooled by an advanced cryocooler, a sub-Kelvin cooler must be used. While sub-Kelvin coolers have been successfully flown on Herschel and Planck, cooler technology with the necessary heat lift have not advanced beyond TRL 3. Existing candidates include ^{3}He-^{4}He dilution refrigerators, ^{3}He sorption coolers, and adiabatic demagnetization refrigerators. The compatibility of these coolers with sub-nanometer wavefront stability required for a coronagraph is unknown.

E.3 Mid-Infrared Ultra-low Noise Detectors

Characterization at wavelengths longer than the 2.5 μm boundary is desirable for searching for biosignatures in exoplanet atmospheres. The HabEX and LUVOIR STDTs have not finalized their long wavelength cutoff, pending trade studies between coronagraph and starshade inner working angles and science goals. Depending on the requirements of the STDTs, it may be necessary to improve the read noise and dark current of detectors sensitive to the mid-infrared (out to 5 μm).

E.4 Astrometry

Precision astrometry determines the Keplerian orbital parameters of an exoplanet, enhancing the direct imaging and characterization of exoplanets by (1) increasing science yield of follow-up coronagraph, and (2) determining the mass of a detected exoplanet without the radial velocity, necessary to assess habitability. The current state of the art is the GAIA mission, preliminarily estimated to achieve 34 mas measurement error and thereby sensitive mainly to Jupiter-mass exoplanets.[137] The precision must be improved to 0.3 mas in a single measurement in order to enable detection of Earth analogs at 10 pc distance[138] (two orders of magnitude). A TDEM-13 (P.I. Eduardo Bendek/NASA-Ames) was awarded for a laboratory demonstration of 10 mas astrometric precision (when installed on a 2.4 m telescope) in conjunction with direct imaging using a PIAA coronagraph,[139] which would establish an important step towards the eventual sub-mas goal.

F PRIORITIZATION

The technology gaps were prioritized by the ExEP technology team (the Program Chief Technologist, the Deputy Technology Development Manager, the Program Chief Scientist, and the Deputy Program Chief Scientist) and reviewed by the Exo-TAC. The three prioritization criteria scores are shown in **Table 8** along with the relative weighting of each used to determine the total score. Definitions of the criteria and their relative values are described in Section A.3.

Table 8: Technology Gap Prioritization. Green refers to a technology gap deemed to be "enabling" while orange refers to an "enhancing" technology gap.

Priority	Gap ID	Gap Title	Impact	Urgency	Trend	Total
		Weight:	10	10	5	
1	S-2	Starlight Suppression and Model Validation	4	4	2	90
2	S-1	Control Edge-Scattered Sunlight	4	4	2	90
2	S-3	Lateral Formation Flying Sensing	4	4	2	90
2	S-4	Petal Shape	4	4	2	90
2	S-5	SS Deployment and Shape Stability	4	4	2	90
3	CG-1	Large Aperture Mirrors	4	3	3	85
3	CG-2	Coronagraph Architecture	4	3	3	85
3	CG-6	Mirror Figure / Segment Phasing, Sense & Control	4	3	3	85
3	CG-7	Telescope Vibration Control	4	3	3	85
3	CG-9	NIR Ultra-Low Noise Detector	4	3	3	85
4	CG-3	Wavefront Sensing and Control	4	3	2	80
4	CG-5	Deformable Mirrors	4	3	2	80
4	CG-8	Visible Ultra-Low Noise Detector	4	3	2	80
5	M-1	Extreme Precision Radial Velocity	3	3	3	75
6	CG-4	Data Post-Processing	4	2	2	70
7	CG-10	UV/NIR/Vis mirror coatings	3	3	2	70
8	CG-11	Mid-IR Spectral Coronagraph	2	3	3	65
9	CG-12	UV Ultra-low noise detector	2	3	2	60

G CONCLUSION

The 2010 Astrophysics Decadal Survey recommended the creation of a technology development program for a potential future exoplanet mission to mature starlight-suppression technology for the detection of spectra of Earth-like exoplanets. The ExEP supports a community-based process to help NASA identify the needed technologies to achieve this goal and to mature the selected concepts to inform the 2020 Decadal Survey committee. This Appendix outlines technology development plans and activities that will lead toward that goal.

A new ExEP Technology Development Plan Appendix will be released each year to update the progress made in each technology area and to identify new SAT-TDEM and APRA funding opportunities.

H DOCUMENT CHANGE LOG

This section contains a log of changes to the ExEP Technology Development Appendix.

Date	Version	Author	Description
Jan 10, 2017	A	B. Crill	Changes relative to 2016 release include updates in TDEM solicitation, updates in prioritization scores for each technology gap, advances in technology areas from TDEM reports, WFIRST technology milestone work, Major updates to **Figure 1** to and Figure 34.
Jan 30, 2017	B	B. Crill	Public release version: New material on telescoping boom starshade deployment added to section C.6, new cover.
Mar 27, 2017	B.1	B. Crill	Update to Figure 1 with new WFIRST requirements.
Apr 14, 2017	B.2	B. Crill	Update to Fig. 1 including WFIRST/starshade
May 1, 2017	B.3	B. Crill	Update to Fig. 1 removing WFIRST contrast curves pending project approval.

I ACRONYMS

ACAD	Adaptive Correction of Aperture Discontinuities
AIP	Astrophysics Implementation Plan
AFTA	Astrophysics Focused Telescope Assets
AMTD	Advanced Mirror Technology Development
APLC	Apodized Pupil Lyot Coronagraph
APRA	Astrophysics Research and Analysis
ATLAST	Advanced Technology Large Aperture Space Telescope
BMC	Boston Micromachines Corporation
CIC	Clock-Induced Charge
CTE	Coefficient of Thermal Expansion
DM	Deformable Mirror
DRM	Design Reference Mission
EMCCD	Electron Multiplying Charge Couple Device
ExEP	Exoplanet Exploration Program
ExoPAG	Exoplanet Program Analysis Group
HabEx	Habitable Exoplanet Imaging Mission
HCIT	High Contrast Imaging Testbed
HDST	High Definition Space Telescope
HiCAT	High Contrast Imager for Complex Aperture Telescopes
HRC	High-Resolution Channel
HST	Hubble Space Telescope
IWA	Inner Working Angle
JWST	James Webb Space Telescope
LOWFS/C	Low-order Wavefront Sensor and Controller
LTF	Low-temperature Fusion
LTS	Low-temperature Slumping
LUVOIR	Large Ultra-Violet Optical Infrared
mas	milliarcseconds
MCP	Micro Channel Plate
MEMS	Micro Electro Mechanical Systems
MKID	Microwave Kinetic Inductance Detectors
NG-VNC	Next Generation Visible Nulling Coronagraph
NICMOS	Near-Infrared Camera and Multi-Object Spectrometer
NWNH	New Worlds, New Horizons (2010 Astronomy and Astrophysics Decadal Survey)
PIAACMC	Phase-Induced Amplitude Apodization Complex Mask Coronagraph
PMN	Lead Magnesium Niobate
PSF	Point Spread Function
QE	Quantum Efficiency
ROSES	Research Opportunities in Space and Earth Sciences
SBIR	Small Business Innovation Research
SIM	Space Interferometry Mission
SLS	Space Launch System

SOA	State of Art
SP	Shaped Pupil
SPLC	Shaped Pupil Lyot Coronagraph
STScI	Space Telescope Science Institute
TCOP	Technology Development for the Cosmic Origins Program
TDEM	Technology Development for Exoplanet Missions
ULE	Ultra-Low Expansion
VNC	Visible Nulling Coronagraph
WFC	Wavefront Control
WFIRST	Wide-Field Infrared Survey Telescope
WFSC	Wavefront Sensing and Control

J REFERENCES

[1] National Research Council. *New Worlds, New Horizons in Astronomy and Astrophysics*. Washington, DC: The National Academies Press, 2010, http://science.nasa.gov/astrophysics/special-events/astro2010-astronomy-and-astrophysics-decadal-survey/

[2] National Research Council. *Review of Progress Toward the Decadal Survey Vision in New Worlds, New Horizons in Astronomy and Astrophysics*. Washington, DC: The National Academies Press, 2016, https://www.nap.edu/catalog/23560/new-worlds-new-horizons-a-midterm-assessment

[3] 2014 update to the Astrophysics Implementation Plan, http://science.nasa.gov/media/medialibrary/2015/01/16/ImpPlan_Rev2_15Apr2013_LL_150107TAGGED.pdf

[4] Exo-C and Exo-S Final Reports (2015); https://exoplanets.nasa.gov/exep/studies/probe-scale-stdt/

[5] WFIRST Home Page: http://wfirst.gsfc.nasa.gov/index.html

[6] LUVOIR Science & Technology Definition Team LUVOIR Study Office & Members of the LUVOIR Technology Working Group. *LUVOIR Decadal Mission Concept Study "O1" Deliverable: Technology Gap Assessment for the 2016 Program Office Technology Cycle*, 2016. http://asd.gsfc.nasa.gov/luvoir/docs/tech/2016-05-31-LUVOIR-O1-Deliverable_rev3.0.pdf

[7] TDEM past awards: https://exoplanets.nasa.gov/exep/technology/TDEM-awards/

[8] NSPIRES APRA past awards: https://nspires.nasaprs.com/external/solicitations/solicitations.do?method=closedPastIni&stack=push

[9] ExEP Technology Website; http://exoplanets.nasa.gov/technology/.

[10] Exo-C Final Report (2015); https://exoplanets.nasa.gov/exep/studies/probe-scale-stdt/

[11] Lawson, P. R., Belikov, R., Cash, W., et al. 2013, "Survey of experimental results in high-contrast imaging for future exoplanet missions," Proc. SPIE 8864, 88641F, http://spiedigitallibrary.org/proceeding.aspx?articleid=1744192&resultClick=1.

[12] Moody, D. C., Gordon, B. L., & Trauger, J. T. 2008, "Design and demonstration of hybrid Lyot coronagraph masks for improved spectral bandwidth and throughput," Proc. SPIE 7010, 70103P, http://spiedigitallibrary.org/proceeding.aspx?articleid=787868&resultClick=1

[13] Trauger, J., Moody, D., Gordon, B., Krist, J., Mawet, D. 2011, "A hybrid Lyot Coronagraph for the direct imaging and spectroscopy of exoplanet systems," Proc. SPIE 8151, 81510G, http://spiedigitallibrary.org/proceeding.aspx?articleid=1342401&resultClick=1.

[14] Trauger, J. et al, TDEM-09 Final Report: http://exoplanets.nasa.gov/files/exep/Lyot_TDEM_Report_121215_signed.pdf

[15] Breckinridge, J., W. Lam, and R. Chipman, 2015, "Polarization Aberrations in Astronomical Telescopes: The Point Spread Function". Publications of the Astronomical Society of the Pacific, 127: 445-468. http://dx.doi.org/10.1086/681280

[16] Krist, J., B. Nemati, and B. Mennesson, 2016, "Numerical modeling of the proposed WFIRST-AFTA coronagraphs and their predicted performances," J. Astron. Telesc. Instrum. Syst. 2016; 2 (1): 011003, http://astronomicaltelescopes.spiedigitallibrary.org/article.aspx?articleid=2468019.

[17] Breckinridge, J. and Chipman, R. TDEM-15 Abstract: https://exoplanets.nasa.gov/system/internal_resources/details/original/355_Abstract_TDEM15_.pdf

[18] John Trauger; Dwight Moody; John Krist; Brian Gordon, 2015, "Hybrid Lyot coronagraph for WFIRST-AFTA: coronagraph design and performance metrics", J. Astron. Telesc. Instrum. Syst. 2016; 2(1):011013. doi: 10.1117/1.JATIS.2.1.011013, http://astronomicaltelescopes.spiedigitallibrary.org/article.aspx?articleid=2482759

[19] Eric Cady; Camilo Mejia Prada; Xin An; Kunjithapatham Balasubramanian; Rosemary Diaz; N. Jeremy Kasdin; Brian Kern; Andreas Kuhnert; Bijan Nemati; Ilya Poberezhskiy; A. J. Eldorado Riggs; Robert Zimmer; Neil Zimmerman, 2015, "Demonstration of high contrast with an obscured aperture with the WFIRST-AFTA shaped pupil coronagraph", J. Astron. Telesc. Instrum. Syst; 2(1):011004. doi: 10.1117/1.JATIS.2.1.011004, http://arxiv.org/pdf/1511.01882v1

[20] Neil T. Zimmerman; A. J. Eldorado Riggs; N. Jeremy Kasdin; Alexis Carlotti; Robert J. Vanderbei, 2016, "Shaped pupil Lyot coronagraphs: high-contrast solutions for restricted focal planes", J. Astron. Telesc. Instrum. Syst; 2(1):011012. doi: 10.1117/1.JATIS.2.1.011012, http://astronomicaltelescopes.spiedigitallibrary.org/article.aspx?articleid=2482760

[21] Soummer, R. ApJ 618, L161 (2005); http://adsabs.harvard.edu/cgi-bin/nph-data_query?bibcode=2005ApJ...618L.161S&db_key=AST&link_type=ABSTRACT&high=5697e4cafa06758

[22] Pueyo & Norman ApJ 769, 31 (2013); http://adsabs.harvard.edu/cgi-bin/nph-data_query?bibcode=2013ApJ...769..102P&db_key=AST&link_type=ABSTRACT&high=5697e4cafa03070

[23] N'Diaye, M., Pueyo, L., & Soummer, R., ApJ 799, 13 (2015); http://adsabs.harvard.edu/cgi-bin/nph-data_query?bibcode=2015ApJ...799..225N&db_key=AST&link_type=ABSTRACT&high=5697e4cafa16543

[24] N'Diaye, M., Pueyo, L., Soummer, R. (2016, submitted)

[25] Neil T. Zimmerman; A. J. Eldorado Riggs; N. Jeremy Kasdin; Alexis Carlotti; Robert J. Vanderbei, 2016, "Shaped pupil Lyot coronagraphs: high-contrast solutions for restricted focal planes", J. Astron. Telesc. Instrum. Syst; 2(1):011012. doi: 10.1117/1.JATIS.2.1.011012, http://astronomicaltelescopes.spiedigitallibrary.org/article.aspx?articleid=2482760

[26] Kasdin, N. J., et al ApJ 582, 1147 (2003); http://adsabs.harvard.edu/cgi-bin/nph-data_query?bibcode=2003ApJ...582.1147K&db_key=AST&link_type=ABSTRACT&high=5697e4cafa23140

[27] Vanderbei, R. J., Spergel, D. N., Kasdin, N. J. ApJ 599, 686 (2003); http://adsabs.harvard.edu/cgi-bin/nph-data_query?bibcode=2003ApJ...599..686V&db_key=AST&link_type=ABSTRACT&high=5697e4cafa23140

[28] Carlotti, A., Vanderbei, R., Kasdin, N. J. Opt. Expr. 19, 26796 (2011), https://www.osapublishing.org/oe/viewmedia.cfm?uri=oe-19-27-26796&seq=0

[29] N'Diaye, M., Pueyo, L., & Soummer, R., ApJ 799, 225 (2015); http://adsabs.harvard.edu/cgi-bin/nph-data_query?bibcode=2015ApJ...799..225N&db_key=AST&link_type=ABSTRACT&high=5697e4cafa18208

[30] Zimmerman, N. T.; N'Diaye, M.; St. Laurent, K. E.; Soummer, R.; Pueyo, L.; Stark, C. C.; Sivaramakrishnan, A.; Perrin, M.; Vanderbei, R. J.; Kasdin, N. J.; Shaklan, S.; Carlotti, A., Proc. SPIE, Volume 9904, 99041Y (2016); http://adsabs.harvard.edu/abs/2016SPIE.9904E..1YZ

[31] Stark, C. C.; Roberge, A.; Mandell, A.; Clampin, M.; Domagal-Goldman, S. D.; McElwain, M. W.; Stapelfeldt, K. R., ApJ, 808, 149 (2015); http://adsabs.harvard.edu/abs/2015ApJ...808..149S

[32] Ibid

[33] Guyon, O. 2003, "Phase-induced amplitude apodization of telescope pupils for extrasolar terrestrial planet imaging," Astron. Astrophys. 404, pp. 379–387, http://arxiv.org/pdf/astro-ph/0301190v2

[34] Guyon, O., Kern, B., Belikov, R., et al. 2012, "Phase Induced Amplitude Apodization (PIAA) coronagraphy: Recent results and future prospects," Proc. SPIE 8442, 84424V, http://spiedigitallibrary.org/proceeding.aspx?articleid=1362336&resultClick=1

[35] Kern, B., Guyon, O., Give'on, A., Kuhnert, A., Niessner, A. 2011, "Laboratory testing of a Phase-Induced Amplitude Apodization (PIAA) coronagraph," Proc. SPIE 8151, 815104, http://spiedigitallibrary.org/proceeding.aspx?articleid=1342434&resultClick=1

[36] Erkin Sidick; Brian Kern; Ruslan Belikov; Andreas Kuhnert; Stuart Shaklan; 2014, "Simulated contrast performance of Phase Induced Amplitude Apodization (PIAA) coronagraph testbed ", Proc. SPIE. 9143, 91430W, http://spiedigitallibrary.org/proceeding.aspx?articleid=1894760&resultClick=1

[37] Olivier Guyon et al., TDEM-09 Final Reports: http://exoplanets.nasa.gov/technology/

[38] Olivier Guyon et al., TDEM-10 Final Report: http://exoplanets.nasa.gov/technology/Guyon-PIAA-Milestone-3.pdf

[39] Mawet, D., et al., (2005) "Annular groove phase mask coronagraph", ApJ 633, 1191–1200 http://dx.doi.org/10.1086/462409

[40] Foo, G., et al., (2005) "Optical vortex coronagraph", Opt. Lett. 30, 3308–3310 https://doi.org/10.1364/OL.30.003308

[41] Serabyn, E., et al., (2010) "An image of an exoplanet separated by two diffraction beamwidths from a star", Nature 464, 1018-1020 http://dx.doi.org/10.1038/nature09007

[42] Mawet, D., et al., (2010) "The Vector Vortex Coronagraph: sensitivity to central obscuration, low-order aberrations, chromaticism, and polarization", Proc. SPIE 7739, 773914 http://dx.doi.org/10.1117/12.858240

[43] Serabyn, E. et al. 2013, "High-contrast imaging with the vortex coronagraph," Proc. SPIE 8864, 8864–32, http://proceedings.spiedigitallibrary.org/proceeding.aspx?articleid=1744178&resultClick=1

[44] Absil, O., et al., (2016) "Three years of harvest with the vector vortex coronagraph in the thermal infrared", Proc. SPIE 9908, 99080Q http://dx.doi.org/10.1117/12.2233289

[45] Mawet, D., et al., (2009) "The vector vortex coronagraph: laboratory results and first light at Palomar Observatory", ApJ 709, 53-57 http://dx.doi.org/10.1088/0004-637X/709/1/53

[46] Eugene Serabyn, et al., "Demonstrations of Deep Starlight Rejection with a Vortex Coronagraph", TDEM-10 Final Report: http://exoplanets.nasa.gov/technology/Serabyn_Final_2010.pdf

[47] Mawet, D. et al., 2011, "Recent results of the second generation of vector vortex coronagraphs on the high-contrast imaging testbed at JPL", Proc. SPIE 8151, 81511D, http://proceedings.spiedigitallibrary.org/proceeding.aspx?articleid=1268318&resultClick=1

[48] Mawet, D. et al., 2013, "The multistage and ring-apodized vortex coronagraph: two simple, small-angle coronagraphic solutions for heavily obscured apertures", 886411, http://proceedings.spiedigitallibrary.org/proceeding.aspx?articleid=1744180&resultClick=1

[49] Mawet, D., et al., (2013) "Ring-apodized Vortex Coronagraphs for Obscured Telescopes. I. Transmissive Ring Apodizers", ApJS 209, 7 http://dx.doi.org/10.1088/0067-0049/209/1/7

[50] Ruane, G., et al., (2016) "Apodized vortex coronagraph designs for segmented aperture telescopes", Proc. SPIE 9912, 99122L http://dx.doi.org/10.1117/12.2024096

[51] Carlotti, A., et al., 2013, "Shaped pupil coronagraphy with WFIRST-AFTA", Proc. SPIE 8864, 886410, http://spiedigitallibrary.org/proceeding.aspx?articleid=1744179&resultClick=1

[52] Fogarty, K., Pueyo, L., and Mawet, D., 2014, "Optimal apodizations for on-axis vector vortex coronagraphs ", Proc. SPIE 9143, 914326, http://proceedings.spiedigitallibrary.org/proceeding.aspx?articleid=1894796&resultClick=1

[53] Mazoyer, J., et al, 2015, "Active correction of aperture discontinuities (ACAD) for space telescope pupils: a parametic analysis", Proc. SPIE 9605, 96050M, http://proceedings.spiedigitallibrary.org/proceeding.aspx?articleid=2443263&resultClick=1

[54] Ruane, G., et al, (2015) "Lyot-plane phase masks for improved high-contrast imaging with a vortex coronagraph", A&A 583, A81 http://dx.doi.org/10.1051/0004-6361/201526561

[55] Mawet, D. et al., (2014), "Demonstration of vortex coronagraph concepts for on-axis telescopes on the Palomar Stellar Double Coronagraph", Proc. SPIE 9143, 91432T http://proceedings.spiedigitallibrary.org/proceeding.aspx?articleid=1894816&resultClick=1

[56] http://www.astro.caltech.edu/~dmawet/new-caltech-group/projects.html

[57] Clampin, M., et al, 2013, TDEM-9 Technology Milestone #1 Final Report, "Visible Nulling Coronagraph Technology Maturation: High Contrast Imaging and Characterization of Exoplanets," Jet Propulsion Laboratory Doc. D-68671 http://exoplanets.nasa.gov/technology/Clampin_Report_FINAL.pdf

[58] Brian Hicks, et al., TDEM-10 Final Report: "Achromatic Visible Nulling Coronagraph Technology Maturation," http://exoplanets.nasa.gov/technology

[59] Brian Hicks, et al., TDEM-13 Whitepaper: "Nulling of an Actively-Controlled Segmented Aperture Telescope," http://exoplanets.nasa.gov/technology

[60] Matt Bolcar, et al., TDEM-14 Abstract: "Next Generation Visible Nulling Coronagraph," https://exoplanets.nasa.gov/exep/technology/TDEM-awards/

[61] Chris Stark et al. 2015, "Lower Limits on Aperture Size for an ExoEarth Detecting Coronagraphic Mission", ApJ 808 149S, http://adsabs.harvard.edu/abs/2015ApJ...808..149S

[62] Stahl, H. P., Postman, M., Smith, W. S. 2013, "Engineering specifications for large aperture UVO space telescopes derived from science requirements," Proc. SPIE 8860 06, http://spiedigitallibrary.org/proceeding.aspx?articleid=1762023&resultClick=1

[63] Postman, M., et al., 2009, "Advanced Technology Large-Aperture Space Telescope (ATLAST): A Technology Roadmap for the Next Decade," http://www.stsci.edu/institute/atlast/documents/ATLAST_NASA_ASMCS_Public_Report.pdf

[64] Dalcanton, J. and Seager, S., et al. [From Cosmic Birth to Living Earths], Association for Universities for Research in Astronomy, Washington, DC, (2015).

[65] Albanese, M., et al. 2006, "Verification of the James Webb Space Telescope coarse phase sensor using the Keck Telescope," Proc. SPIE 6265 05, http://spiedigitallibrary.org/proceeding.aspx?articleid=1326681&resultClick=1

[66] Stahl, H. P., Postman, M., Smith, W. S. 2013, "Engineering specifications for large aperture UVO space telescopes derived from science requirements," Proc. SPIE 8860, http://spiedigitallibrary.org/proceeding.aspx?articleid=1762023&resultClick=1

[67] Stahl, M. T., Shaklan, S. B., Stahl, H. P. 2015, "Preliminary Analysis of effect of random segment errors on coronagraph performance," Proc SPIE 9605 0P, http://spiedigitallibrary.org/proceeding.aspx?articleid=2446862&resultClick=1

[68] Stahl, H. P., Postman, M., Smith, W. S. 2013, "Engineering specifications for large aperture UVO space telescopes derived from science requirements," Proc. SPIE 8860 06, http://spiedigitallibrary.org/proceeding.aspx?articleid=1762023&resultClick=1

[69] Gonzales, M. A., et al., "Unprecedented Vibration isolation Demonstration using the Disturbance Free Payload Concept," AIAA 2004-5247, (2004), http://arc.aiaa.org/doi/pdf/10.2514/6.2004-5247

[70] Feinberg, L.D., et al. 2009, "Large segmented UV-optical space telescope using a Hybrid Sensor Active Control (HSAC) architecture," Proc. SPIE 7436 08, http://spiedigitallibrary.org/proceeding.aspx?articleid=785987&resultClick=1

[71] Pueyo, L, and Norman, C. 2013, "High-contrast Imaging with an Arbitrary Aperture: Active Compensation of Aperture Discontinuities ", ApJ 769, 102, http://adsabs.harvard.edu/cgi-bin/nph-data_query?bibcode=2013ApJ...769..102P&db_key=AST&link_type=ABSTRACT&high=5697e4cafa22878

[72] John Trauger; Dwight Moody; John Krist; Brian Gordon, *J. Astron. Telesc. Instrum. Syst.* 2016; 2(1):011013. doi: 10.1117/1.JATIS.2.1.011013

[73] Jeremy Kasdin, et al., TDEM-10 Final Report, "Integrated Coronagraph Design and Wavefront Control using Two Deformable Mirrors", http://exoplanets.nasa.gov/technology/TDEM_Kasdin_D-93928.pdf

[74] Private communication with John Trauger (December 2015).

[75] Clampin, M., et al, 2013, TDEM-9 Technology Milestone #1 Final Report, "Visible Nulling Coronagraph Technology Maturation: High Contrast Imaging and Characterization of Exoplanets", Jet Propulsion Laboratory Doc. D-68671, http://exoplanets.nasa.gov/technology/Clampin_Report_FINAL.pdf

[76] Enya, K., Abe, L., Takeuchi, S., et al., 2011, "A high dynamic-range instrument for SPICA for coronagraphic observation of exoplanets and monitoring of transiting exoplanets," Proc. SPIE 8146, 81460Q, http://spiedigitallibrary.org/proceeding.aspx?articleid=1342223&resultClick=1

[77] Mendillo, C. B., Hicks, B. A., Cook, T. A., et al. 2012, "PICTURE: a sounding rocket experiment for direct imaging of an extrasolar planetary environment," Proc. SPIE 8442, 84420E, http://spiedigitallibrary.org/proceeding.aspx?articleid=1362201&resultClick=1

[78] Traguer, J. T., et al., 2004, "Coronagraph contrast demonstrations with the high-contrast imaging testbed," SPIE 5487, 1330, http://proceedings.spiedigitallibrary.org/proceeding.aspx?articleid=847161

[79] Borde, P., and Traub, W., 2006, "High-contrast Imaging from Space: Speckle Nulling in a Low-Aberration Regime," Ap J 638, 488, http://iopscience.iop.org/article/10.1086/498669/meta;jsessionid=AE9D87794822875D9383A0D7E1F684F6.c4.iopscience.cld.iop.org

[80] Give'on, A., et al., 2007, "Broadband wavefront correction algorithm for high-contrast imaging systems" SPIE 6691, 66910A, http://proceedings.spiedigitallibrary.org/proceeding.aspx?articleid=1322594

[81] Pueyo, L., et al., 2009, "Optimal dark hole generation via two deformable mirrors with stroke minimization," Applied Optics 48, 32, 6296. https://www.osapublishing.org/ao/abstract.cfm?uri=ao-48-32-6296

[82] Belikov, R., Bendek, E., Pluzhnik, E., Sirbu, D., Thomas, S.J., 2016, "High contrast imaging in multi-star systems: technology development and first lab results," Proc SPIE 9904. http://proceedings.spiedigitallibrary.org/proceeding.aspx?articleid=2541995

[83] Guyon, O., Schneider, G., Close, L., et al. 2011, "Technology Milestone #2 Whitepaper: Instrument Tip-Tilt Control Demonstration at the sub-Milliarcsecond Level," Jet Propulsion Laboratory Doc. D-71066. http://exoplanets.nasa.gov/files/exep/Guyon_Milestone_WP2.pdf

[84] Shi, F. et al. 2016; "Low Order Wavefront Sensing and Control for WFIRST-AFTA Coronagraph", SPIE 9904 90418 (29 July 2016); doi: 10.1117/12.2234226

[85] Robinson, T., et al., 2014, "Detection of Ocean Glint and Ozone Absorption using LCROSS Earth Observations", ApJ 787: 171. http://dx.doi.org/10.1088/0004-637X/787/2/171

[86] Hennessy, J., et al., 2016, "Performance and prospects of far ultraviolet aluminum mirrors protected by atomic layer deposition" J. Astron. Telesc. Instrum. Syst. 2(4), 041206 (Jun 07, 2016). doi:10.1117/1.JATIS.2.4.041206 http://astronomicaltelescopes.spiedigitallibrary.org/article.aspx?articleid=2528070

[87] Gach et al. 2014, "Development of a 4k×4k frame transfer electron multiplying CCD for scientific applications", SPIE 9154 91540A, http://spiedigitallibrary.org/proceeding.aspx?articleid=1891356&resultClick=1

[88] Figer, D. 2010, et al., TDEM9 "Technology Milestone Final Report: A Photon-Counting Detector for Exoplanet Missions," Jet Propulsion Laboratory. D-93392; http://exoplanets.nasa.gov/technology/TDEMReportFiger.pdf

[89] Rauscher, B. et al. 2015, "ATLAST detector needs for direct spectroscopic biosignature characterization in the visible and near-IR", SPIE 9602, 96020D, http://spiedigitallibrary.org/proceeding.aspx?articleid=2444184&resultClick=1

[90] Rauscher, B. et al. 2015, "ATLAST detector needs for direct spectroscopic biosignature characterization in the visible and near-IR", SPIE 9602, 96020D, http://spiedigitallibrary.org/proceeding.aspx?articleid=2444184&resultClick=1

[91] Atkinson, D., Hall, D., Baranec, C., Baker, I., Jacobson, S., and Riddle, R., 2014, "Observatory deployment and characterization of SAPHIRA HgCdTe APD arrays," SPIE 9154, 915419, http://spiedigitallibrary.org/proceeding.aspx?articleid=1891378&resultClick=1

[92] Mazin, B. A., et al., "A superconducting focal plane array for ultraviolet, optical, and near-infrared astrophysics," Opt. Express 20, 1503-1511 (2012), http://arxiv.org/pdf/1112.0004v1.pdf

[93] Private communications with Bernie Rauscher (December 2015)

[94] Rauscher, B., et al., 2015, "ATLAST detector needs for direct spectroscopic biosignature characterization in the visible and near-IR", SPIE 9602, 96020D, http://spiedigitallibrary.org/proceeding.aspx?articleid=2444184&resultClick=1

[95] ibid

[96] Robinson, T., et al., 2014, "Detection of Ocean Glint and Ozone Absorption using LCROSS Earth Observations", ApJ 787: 171. http://dx.doi.org/10.1088/0004-637X/787/2/171

[97] Bolcar, M., et al., 2016, "Technology Gap Assessment for a Future Large-aperture Ultraviolet-Optical-Infrared Space Telescope," J. Astron. Telesc. Instrum. Syst. 2(4), 041209. doi:10.1117/1.JATIS.2.4.041209 http://astronomicaltelescopes.spiedigitallibrary.org/article.aspx

[98] Soummer, R., et al., 2014, "Five Debris Disks Newly Revealed in Scattered Light from the Hubble Space Telescope NICMOS Archive," The Astrophysical Journal Letters 786 (23S), http://adsabs.harvard.edu/cgi-bin/nph-data_query?bibcode=2014ApJ...786L..23S&db_key=AST&link_type=ABSTRACT&high=5697e4cafa04593

[99] Menesson, D., 2015, "AFTA coronagraph performance feedback from post-processing studies to overall design," Proc. SPIE 9605, http://spiedigitallibrary.org/proceeding.aspx?articleid=2443259&resultClick=1

[100] Ygouf, M., et al., 2015, "Data processing and algorithm development for the WFIRST-AFTA coronagraph: reduction of noise free simulated images, analysis and spectrum extraction with reference star differential imaging" Proc. SPIE 9605 9605 0S, http://spiedigitallibrary.org/proceeding.aspx?articleid=2443266&resultClick=1

[101] http://asd.gsfc.nasa.gov/firs/

[102] Boccaletti, A., et al., 2015, "The Mid-Infrared Instrument for the James Webb Space Telescope, V: Predicted Performance of the MIRI Coronagraphs," Publications of the Astronomical Society of the Pacific Vol 127, 953, http://iopscience.iop.org/article/10.1086/682256

[103] Shaklan, S. B., Noecker, M. C., Glassman, T., et al. 2010, "Error budgeting and tolerancing of starshades for exoplanet detection," Proc. SPIE 7731, 77312G, http://spiedigitallibrary.org/proceeding.aspx?articleid=749972&resultClick=1

[104] Shaklan, S. B., Marchen, L., Lisman, P. D., et al. 2011, "A starshade petal error budget for exo-earth detection and characterization," Proc. SPIE 8151, 815113, http://spiedigitallibrary.org/proceeding.aspx?articleid=1268343&resultClick=1

[105] Exo-S Final Report, https://exoplanets.nasa.gov/exep/studies/probe-scale-stdt/

[106] Schindhelm, E., Shipley, A., Oakley, P., et al. 2007, "Laboratory studies of petal-shaped occulters" Proc. SPIE 6693, 669305, http://spiedigitallibrary.org/proceeding.aspx?articleid=817922&resultClick=1

[107] Leviton, D. B., Cash, W. C., Gleason, B., et al. 2007, "White-light demonstration of one hundred parts per billion irradiance suppression in air by new starshade occulters." Proc. SPIE 6687 66871B, http://spiedigitallibrary.org/proceeding.aspx?articleid=817377&resultClick=1

[108] Lo, A. S., Glassman, T., Dailey, D., Sterk, K., Green, J., Cash, W., Soummer, R. 2010, "New Worlds Probe," Proc. SPIE 7731, 77312E, http://spiedigitallibrary.org/proceeding.aspx?articleid=749969&resultClick=1

[109] Samuele, R., Varshneya, R., Johnson, T. P., et al. 2010, "Progress at the starshade testbed at Northrop Grumman Aerospace Systems: comparisons with computer simulations," Proc. SPIE 7731, 773151, http://spiedigitallibrary.org/proceeding.aspx?articleid=750104&resultClick=1

[110] Cady, E. et al. 2010, "Broadband suppression and occulter position sensing at the Princeton occulter testbed." Proc. SPIE 7731, 77312F, http://spiedigitallibrary.org/proceeding.aspx?articleid=749970&resultClick=1

[111] Sirbu, D., Kasdin, N. J., Vanderbei, R. J., 2013, "Progress on optical verification for occulter-based high contrast imaging," Proc. SPIE 8864, 886419, http://spiedigitallibrary.org/proceeding.aspx?articleid=1744187&resultClick=1

[112] Glassman, T. et al., TDEM-12 Final Report, "Demonstration of Starshade Starlight-Suppression Performance in the Field"; http://exoplanets.nasa.gov/files/exep/GlassmanTDEM2012_FinalReport.pdf

[113] Kasdin et al., TDEM-12 White Paper "Optical and Mechanical Verification of an External Occulter for Starlight Suppression", http://exoplanets.nasa.gov/files/exep/Kasdin_OcculterTDEM_12_Milestone_signed.pdf

[114] Martin, S. R., Shaklan, S. B., Crawford, S. L., et al. 2013, "Starshade optical edge modelling, requirements, and laboratory tests," Proc. SPIE 8864, 88641A, http://spiedigitallibrary.org/proceeding.aspx?articleid=1744188&resultClick=1

[115] Steeves, J.S., Martin, S. R., et. al. 2016, "Precision optical edges for a starshade external occulter",

Proc. SPIE 9912, 99122O, http://proceedings.spiedigitallibrary.org/proceeding.aspx?articleid=2538386

116 Casement et al., TDEM-12 Whitepaper "Starshade Stray Light Mitigation through Edge Scatter Modeling and Sharp-Edge Materials Development"; http://exoplanets.nasa.gov/technology/casement_whitepaper.pdf

117 Seager, S., et al., 2015, "Exo-S: starshade probe-class exoplanet direct imaging mission concept, Final Report," https://exoplanets.nasa.gov/exep/stdt/Exo-S_Starshade_Probe_Class_Final_Report_150312_URS250118.pdf

118 Cash, W., Kendrick, S., Noecker, et al., 2009, "The New Worlds Observer: the astrophysics strategic mission concept study," Proc. SPIE 7436, http://spiedigitallibrary.org/proceeding.aspx?articleid=785984&resultClick=1

119 N.J. Kasdin et al., 2009, "Occulter design for THEIA," Proc. SPIE 7440, http://proceedings.spiedigitallibrary.org/proceeding.aspx?articleid=786370

120 Scarf, D. et al., 2015 Precision Formation Flying at Megameter Separations for Exoplanet Characterization, 8th International Workshop on Satellite Constellations and Formation Flying, 8-10 June, 2015 (journal coming out in early CY16).

121 Exo-S Final Report, https://exoplanets.nasa.gov/exep/studies/probe-scale-stdt/

122 Exo-S Final Report, https://exoplanets.nasa.gov/exep/studies/probe-scale-stdt/

123 Cash, W., Kendrick, S., Noecker, et al., 2009, "The New Worlds Observer: the astrophysics strategic mission concept study," Proc. SPIE 7436. http://spiedigitallibrary.org/proceeding.aspx?articleid=785984&resultClick=1

124 Kasdin, J., TDEM-10 Final Report, "Verifying Deployment Tolerances of an External Occulter for Starlight Suppression", http://exoplanets.nasa.gov/technology/KasdinTDEM10FinalReport.pdf

125 Exo-S Final Report, p.6-26, https://exoplanets.nasa.gov/exep/studies/probe-scale-stdt/

126 Cash, W. 2006, "Detection of Earth-like planets around nearby stars using a petal-shaped occulter," Nature 442, pp. 51–53, http://www.nature.com/nature/journal/v442/n7098/full/nature04930.html

127 Vanderbei, R. J., Cady, E., & Kasdin, N. J. 2007, "Optimal Occulter Design for Finding Extrasolar Planets," Astrophys. J. 665, pp. 794–798, http://adsabs.harvard.edu/cgi-bin/nph-data_query?bibcode=2007ApJ...665..794V&db_key=AST&link_type=ABSTRACT&high=5697e4cafa02790

128 Cady, E. 2011, "Nondimensional representations for occulter design and performance evaluation," Proc. SPIE 8151, 815112, http://spiedigitallibrary.org/proceeding.aspx?articleid=1268342&resultClick=1

129 Lo, A., Cash, W., Hyde, T., Polidan, R., & Glassman, T., 2009, "Starshade Technology Development: Astro2010 Technology Development Whitepaper," ArXiv Astrophysics e-prints 2010, pp. 44+, http://www8.nationalacademies.org/astro2010/DetailFileDisplay.aspx?id=525

130 Plavchan, P., et al., 2015, "Radial Velocity Prospects Current and Future: A White Paper Report prepared by the Study Analysis Group 8 for the Exoplanet Program Analysis Group (ExoPAG)" https://arxiv.org/abs/1503.01770

131 Fischer, D, et al., 2016, "State of the Field: Extreme Precision Radial Velocities", workshop summary whitepaper, https://arxiv.org/abs/1602.07939

132 ibid.

[133] Schwab, C., et al, 2016, "Design of NEID, an extreme precision Doppler spectrograph for WIYN", Proc. SPIE 9908, Ground-based and Airborne Instrumentation for Astronomy VI, 99087H (August 9, 2016); doi:10.1117/12.2234411 http://proceedings.spiedigitallibrary.org/proceeding.aspx?articleid=2544294

[134] Crepp, J, et al, 2016, "iLocater: A Diffraction-limited Doppler Spectrometer for the Large Binocular Telescope", Proc. SPIE 9908, Ground-based and Airborne Instrumentation for Astronomy VI, 990819 (4 August 2016); doi:10.1117/12.2233135, http://proceedings.spiedigitallibrary.org/proceeding.aspx?articleid=2543021

[135] Plavchan, P., et al., 2015, "Radial Velocity Prospects Current and Future: A White Paper Report prepared by the Study Analysis Group 8 for the Exoplanet Program Analysis Group (ExoPAG)" https://arxiv.org/abs/1503.01770

[136] Rauscher, B, et al., 2016, "Detectors and cooling technology for direct spectroscopic biosignature characterization" J. Astron. Telesc. Instrum. Syst. 2(4), http://astronomicaltelescopes.spiedigitallibrary.org/article.aspx?articleid=2545567

[137] Perryman, M., et al., 2014, "Astrometric Exoplanet Detection with GAIA", ApJ 797, 14, http://iopscience.iop.org/article/10.1088/0004-637X/797/1/14/meta

[138] Catanzarite, J, et al., 2006, "Astrometric Detection of Terrestrial Planets in the Habitable Zone of Nearby Stars with SIM PlanetQuest" PASP 118, 847 http://iopscience.iop.org/article/10.1086/504442

[139] Bendek, E., et al., TDEM-13 Whitepaper: "Enhanced Direct Imaging Exoplanet Detection with Astrometry Mass Determination," http://exoplanets.nasa.gov/technology